PONTIFICIA UNIVERSIDAD CATÓLICA DE CHILE
ESCUELA DE INGENIERÍA

OPTICAL DESIGN AND PROTOTYPE OF A HIGH RESOLUTION NEAR IR SPECTROGRAPH FOR ASTRONOMY

SURANGKHANA RUKDEE

Thesis submitted to the Office of Graduate Studies
in partial fulfillment of the requirements for the Degree of
Doctoral of Science in Engineering

Advisors:
LEONARDO VANZI

Santiago de Chile, November, 2019

PONTIFICIA UNIVERSIDAD CATÓLICA DE CHILE
ESCUELA DE INGENIERÍA

OPTICAL DESIGN AND PROTOTYPE OF A HIGH RESOLUTION NEAR IR SPECTROGRAPH FOR ASTRONOMY

SURANGKHANA RUKDEE

Members of the Committee:
LEONARDO VANZI
YADRAN ETEROVIC SOLANO
ANDRÉS GUESALAGA
MIGUEL ATTILIO TORRES
ANDRÉS JORDÁN
ANDREI TOKOVININ
CHRISTIAN SCHWAB

Thesis submitted to the Office of Graduate Studies
in partial fulfillment of the requirements for the Degree of
Doctoral of Science in Engineering

Santiago de Chile, November, 2019

Dear My Family

ACKNOWLEDGEMENTS

It has been quite a journey for my Ph.D. study. Firstly, I would like to express my sincere gratitude to my supervisor Prof. Leonardo Vanzi for the continuous support of my Ph.D. study and related research, for his patience, motivation, and immense knowledge. I would like to thank him for giving me independence in this research. His guidance helped me in all the time of research and writing of this thesis.

Besides my advisor, I would like to thank the rest of my thesis committee: Prof. Jorge Vasquez Pinillos, Prof. Andres Guesalaga, Prof. Miguel Attilio Torres, Prof. Andres Jordan and Dr. Andrei Tokovinin, for their insightful comments and encouragement, but also for the hard questions which incented me to widen my research from various perspectives.

My sincere thanks also goes to Dr. Christian Schwab, who provided me an opportunity to join his team as an intern, and gave access to the laboratory and research facilities. Without their precious support, it would not be possible to conduct this research. Special thank to Chris Schwab who always shares with me great advices for the projects, lives, and future career.

I thank my fellow lab-mates in for the stimulating discussions, and for all the fun we have had in the last four years. I thank Abner Zapata and Rafael Brahm for the insightful technical and science discussion. I thank Mauricio Flores and Alvaro Valenzuela Navarro for the help on mechanical design and fabrication of TARdYS. Also I thank the AIUC team for their support.

I thank Dr. Franz E. Bauer who always gives me support, encouragement and opportunity to enhance my strength in the optical design.

Last but not the least, I would like to thank my family: my parents and my brother for supporting me spiritually throughout writing this thesis and my life in general. I thank my better half, Johannes Buchner for his support in every way he can and to always tell me that everything is going to be okay.

TABLE OF CONTENTS

LIST OF FIGURES

LIST OF TABLES

ABSTRACT

The search for extraterrestrial planets is an exciting current field of research. One of the most efficient ways to detect exoplanets is through the measurement of the Radial Velocity (RV) detection of Doppler shifts of the host star. Recently, the target of the exoplanet search has moved to cooler and lower mass stars. Although these cool stars are abundant in our galaxy, most of them are too faint to be detected by instruments operating in the visible. Thus, it requires high resolution spectroscopy in the near infrared region. In this work, we will contribute to the field by developing a cost-effective infrared spectrograph which will empower the upcoming generation of telescopes.

The Tao Aiuc high Resolution (d) Y band Spectrograph (TARdYS) project is a collaboration between the Center of Astro-Engineering UC-AIUC, Chile and the University of Tokyo, Japan. The instrument is a high resolution near infrared spectrograph for astronomy being developed at the AIUC for installation at the Tokyo Atacama Observatory TAO 6.5 m. telescope. TARdYS is optimized for the precise measurement of radial velocities of cool stars. For this science purpose, the instrument requires high resolution $>$ 60,000 and RV precision of 5 m/s. Moreover, it will also be a powerful tool for the study of astroseismology, star-forming regions, and exoplanet atmosphere.

The requirements of the instrument are derived from the science objectives and budget constraint. We select a 1kx1k infrared detector and an R6 echelle disperser. This choice enables high resolution with a small beam diameter. TARdYS can yield a spectral resolution $>$ 60,000 within the spectral coverage from 0.843-1.117 μm. We plan to use a cryogenic Dewar in the last part of the objectives to minimize the background radiation reaching the detector. Thus, this will be operated in a semi-cryogenic system as a cost-effective solution.

In this work, I created and evaluated the optical design of the two different configurations for a cost-effective high resolution near-infrared spectrograph. This work tests a cost-effective

solution with less widely tested spectrograph choices, especially an R6 echelle, and only a semi-cryogenic setup.

Optimization with computer-aided simulations yields excellent spectral resolution at the diffraction limit even when taking realistic manufacturing and alignment tolerances into account. I built a prototype of the spectrograph using commercially available components and determined its performance. The measured spectral resolution agrees well with the simulation. With a simple temperature control, I achieved a stability of ±0.1K over several hours. The remaining spectral drift is predominately caused by environmental pressure.

Once TARdYS is installed at TAO, it will become available as a exoplanet hunter to the Chilean science community.

Keywords: Spectroscopy, Astronomical Instrumentation, Exoplanets, Infrared

1. INTRODUCTION

1.1. The search for exoplanets

After the first discovery of a planet outside solar system in 1995 (Mayor & Queloz, 1995), exoplanet science quickly became a main branch of astronomical research. The interest of the subject is high as it will shed light on the formation and evolution of planetary systems and ultimately, the likelihood of life in the universe. Several observation techniques have been applied to the search of exoplanets. These includes Radial velocity, Transits, Astrometry, Timing, Microlensing, and Direct Imaging (see review of Exoplanet Handbook from Perryman) (Perryman, 2011). The number of exoplanet detection from different methods to date is displayed in Fig. 1.1.

Radial Velocity (RV) technique measures Doppler shifts in stellar lines due to the orbital motion of a nearby planet using a high-resolution spectrograph. It can derive masses ($m \sin i$) but not planet radii.

Transits is a photometric method that aims at detecting the planet crossing in front of its parent star. This phenomena causes the visual brightness of the star to drop by small amount according to the relative size of the planet. This method can infer the radii of planets, but not their masses.

Astrometry is the measurement of the positions and movements of stars. In terms of extra-solar planet detection, astrometry technique is applied to measure the small wobble, caused by small companion, in the stars' position. This method is ideal when the system is 'face on'

Timing are observations of periodic variations in several classes of astronomical objects such as radio pulsars, pulsating stars, eclipsing binaries and a transit event. In pulsars timing, for example, the observed radio pulses are used to track the pulsar's motion. The pulse-timing observations can disclose the parameters of the orbit (if it has a planet). It can potentially

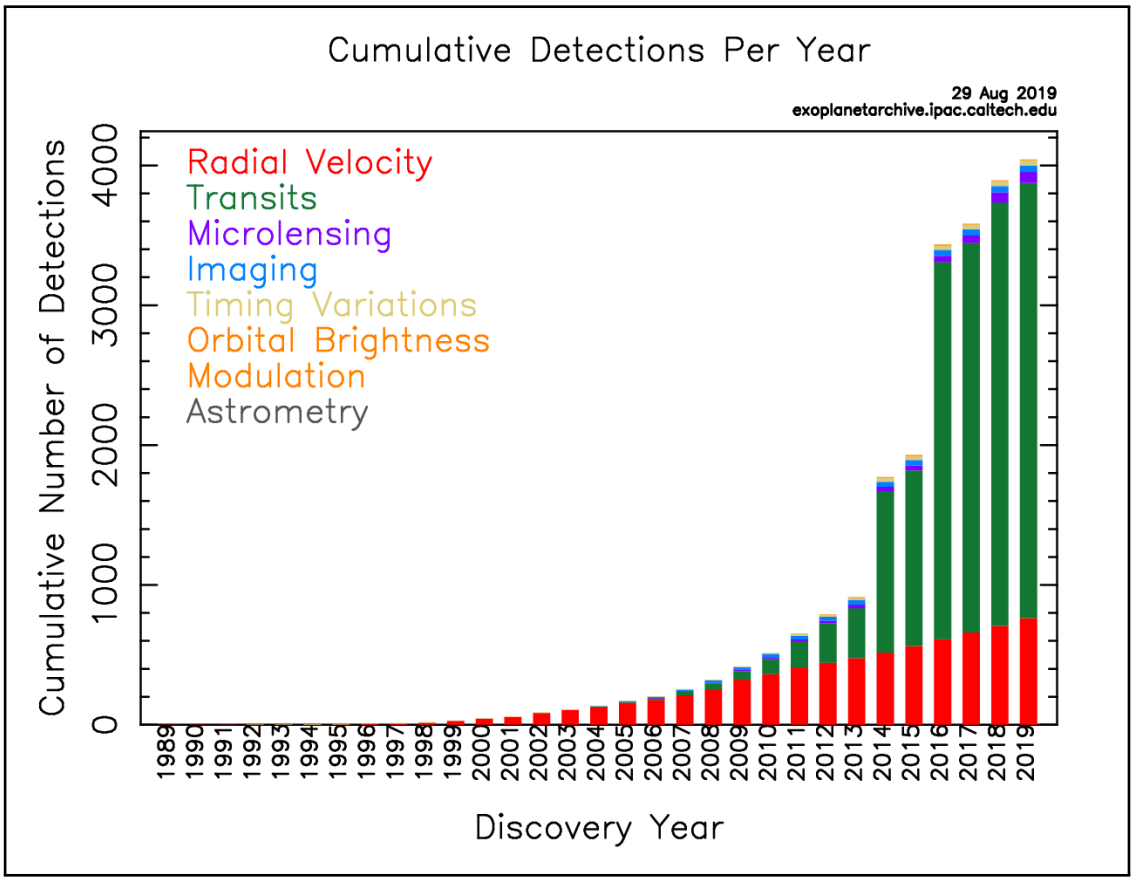

Figure 1.1. Confirmed exoplanet detection to date using different methods.

detect planets down to less than a tenth mass of Earth. However, due to the high-energy radiation of pulsars, it is unlikely that life can survive on those planets around pulsar.

Microlensing: An exoplanet can be detected due to the effects of the gravitational field of a planetary system on the passing light of a distant background star. This method is sensitive to detect low-mass planets around distant stars.

Direct Imaging of exoplanetary systems make use of Adaptive Optics (AO) and work best for the 'face on' planetary system whose planets orbit at a great distance.

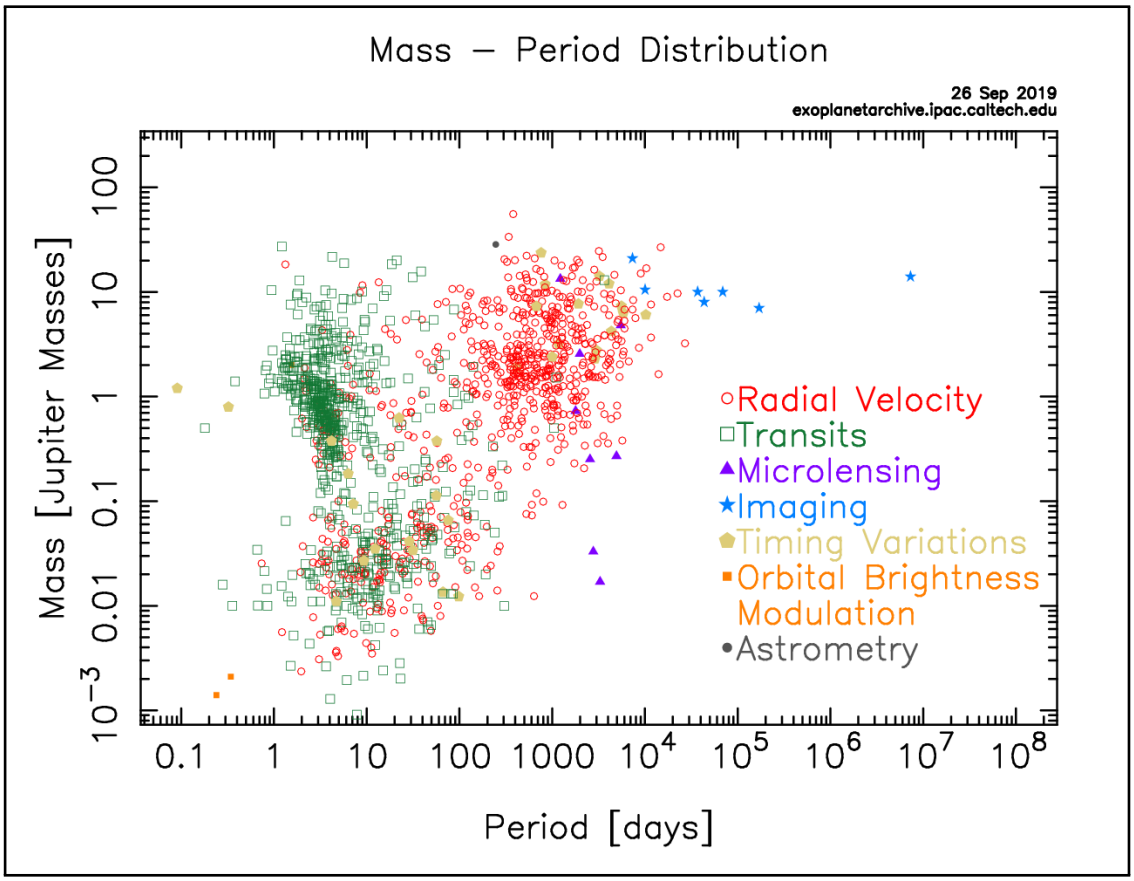

Figure 1.2. Confirmed exoplanet detections to date using different methods, displays in mass period distribution .

1.1.1. Radial Velocity of a Star

Despite the increasing number of exoplanets found through the transit method ((Crossfield et al., 2016), (Vanderburg et al., 2016)), RV measurements remain a fundamental tool for confirming and characterizing exoplanets. The illustration in Fig.1.2 shows the confirmed exoplanet detections using different methods in terms of mass-period distribution. Transits and Radial Velocity are the two most effective methods for exoplanet detection. It can be seen that both can reach the low mass planets (less than 0.01 Jupiter Masses). Moreover the Radial Velocity method also allows the detection of planets with relatively longer periods.

Planets are generally much fainter than their host stars and difficult to detect by their emission. However, their gravitational pull can make the star wobble and produce measurable periodic shifts in the apparent speed of the parent star. The velocity measurement along the line of sight of the observer can reveal the change in wavelength due to the Doppler effect, the phenomenon of changing wavelength for an observer who is moving relative to the source.

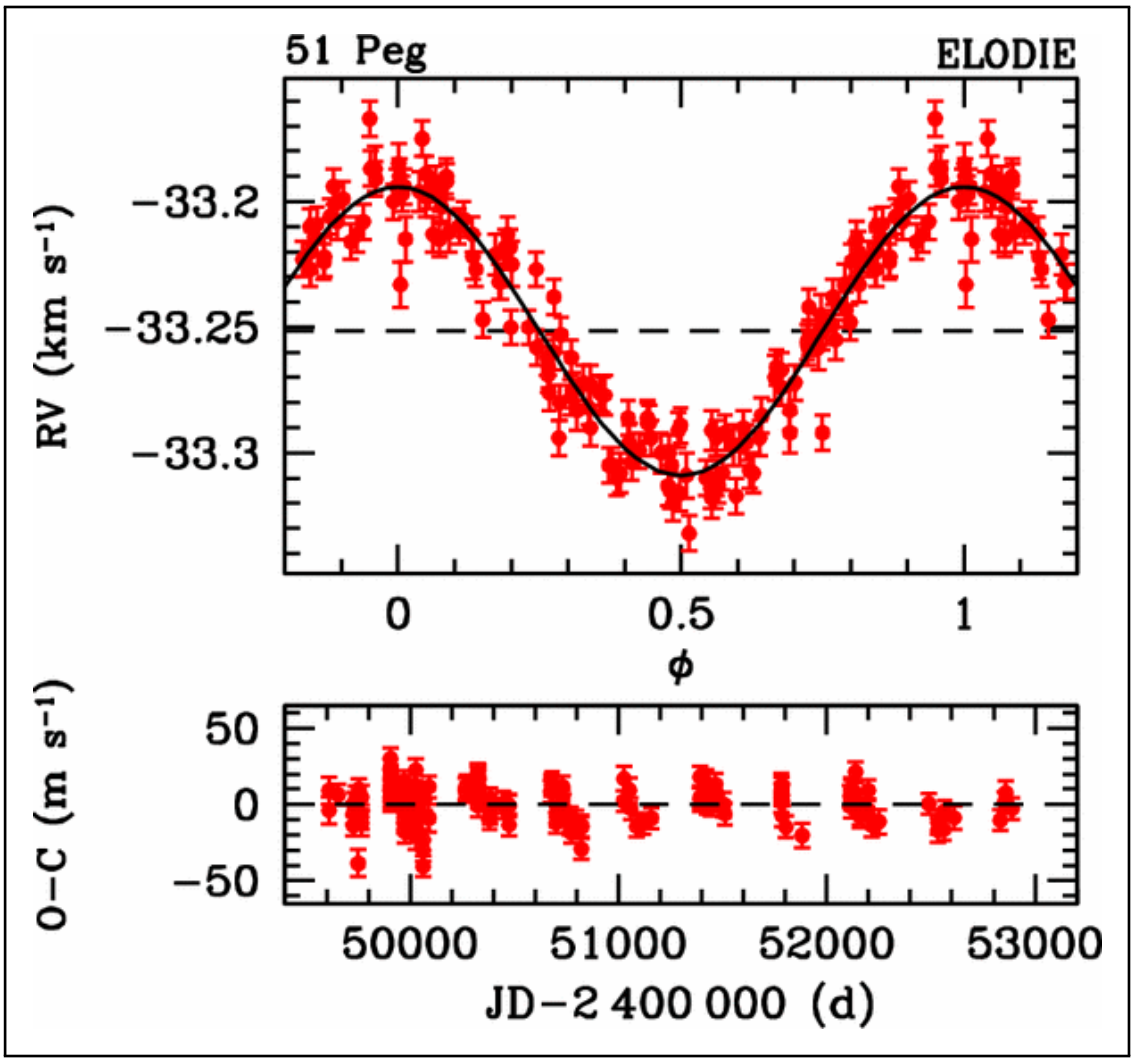

Figure 1.3. Radial Velocity of a Jupiter mass exoplanet orbiting around 51Peg with a period of 4.3 days, semi-major axis 0.05 AU and mass of 0.45 M_{Jup} (Mayor & Queloz, 1995) (Retrieved from `https://obswww.unige.ch/~udry/planet/51peg.html`).

The radial velocity of a star, as shown in Fig.1.3, can be describe according to (Murray & Dermott, 2000) (Balan & Lahav, 2009) and (Feroz, Balan, & Hobson, 2011) as:

$$v_{(i,t_i)} = V - \sum_{p=1}^{N_p} K_p[sin(f_{i,p} + \omega_p + e_p \sin(\omega_p)] \quad , \tag{1.1}$$

where v_i is the ith radial velocity entry corresponding to the time t_i,

V = systematic velocity of the system,

K_p = velocity semi-amplitude of the pth planet,

ω_p = longitude of periastron of pth planet,

$f_{i,p}$ = true anomaly of the pth planet,

e_p = orbital eccentricity of the pth planet.

One can, in the end, calculate the mass of the planets using the velocity semi-amplitude as describe in (Lovis & Fischer, 2010)

$$K_p = \sqrt{\frac{G}{1-e^2}} m_2 \sin i (m_1 + m_2)^{-1/2} a^{-1/2} \quad , \tag{1.2}$$

where m_1 and m_2 are the masses of the bodies,

i = the inclination of the orbital plane with the ecliptic,

e = eccentricity of the planet.

This equation can be displayed in practical units as:

$$K_p = \frac{28.4329 m s^{-1}}{\sqrt{1-e^2}} \frac{m_2 \sin i}{M_{Jup}} \left(\frac{m_1 + m_2}{M_\odot} \right)^{-1/2} \left(\frac{a}{1AU} \right)^{-1/2} \quad , \tag{1.3}$$

One can use Kepler's third law to replace semi-major axis a with the orbital period P:

$$K_p = \frac{28.4329 m s^{-1}}{\sqrt{1-e^2}} \frac{m_2 \sin i}{M_{Jup}} \left(\frac{m_1 + m_2}{M_\odot} \right)^{-2/3} \left(\frac{P}{1yr} \right)^{-1/3} \quad . \tag{1.4}$$

Then one can rewrite the equation in terms of the planet m_2 mass as:

$$\frac{m_2 \sin i}{M_{Jup}} = K_p \frac{\sqrt{1-e^2}}{28.4329 m s^{-1}} \left(\frac{m_1 + m_2}{M_\odot}\right)^{2/3} \left(\frac{P}{1yr}\right)^{1/3} \quad . \tag{1.5}$$

The left hand side of Eq.1.5 is the minimum mass of the planet due to the inclination of the orbit, that we obtain from the RV measurements in (km/s).

1.1.2. Exoplanet around low-mass cool stars

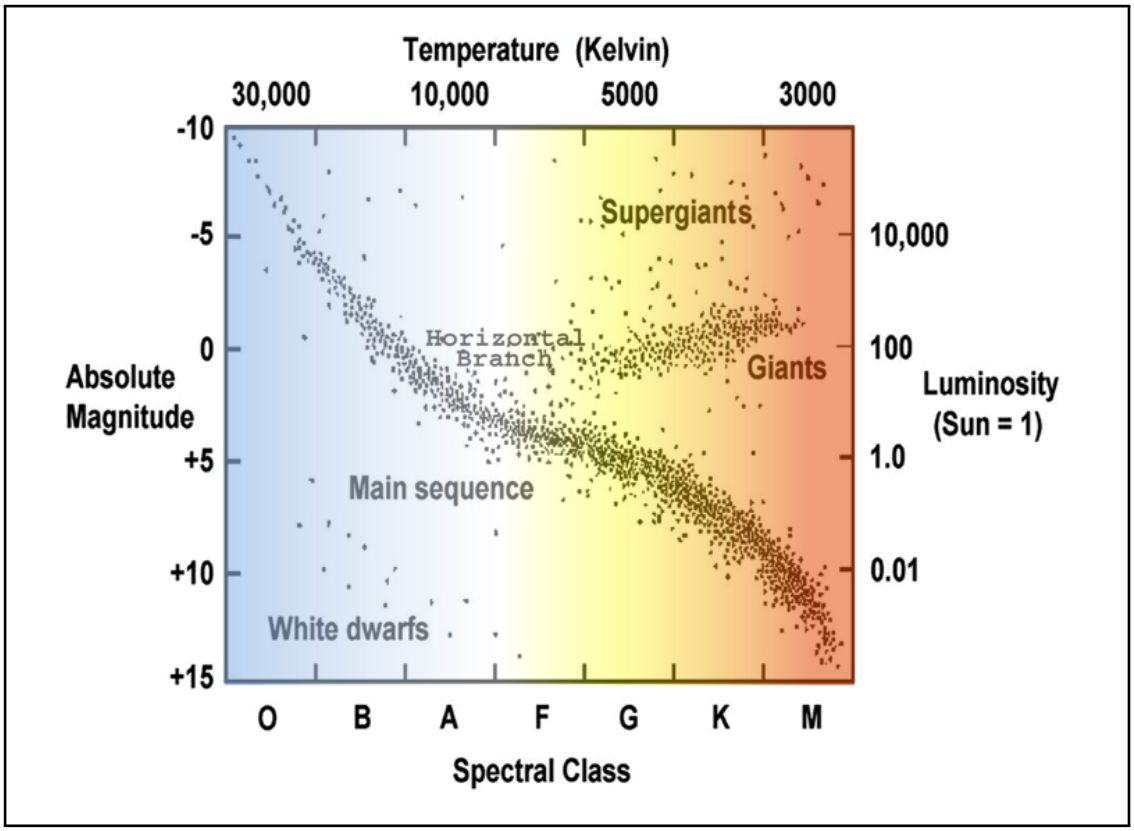

Figure 1.4. Hertzsprung–Russell diagram overlayed with Vega-relative chromaticity. (Adapted from `http://chandra.harvard.edu/edu/formal/variable_stars/HR_student.html`).

Astronomers classify stars into several spectral types depending on the temperature of the star using the 'Harvard spectral classification' introduced in the 1800s. The spectral sequence

is ordered from the hottest to the coolest stars represented by letters: *O, B, A, F, G, K, M*. The Hertzsprung–Russell diagram (H-R diagram) in Fig.1.4 is a fundamental tool that astronomers use to classify stars. The diagram displays the Temperature in Kelvin of the stars corresponding to different spectral classes/types. The sun is a G type star. In recent years, the exoplanet search has moved to cooler and lower mass stars. Thus in this research, I focus on the spectral class M, which has effective temperatures of 2,400-3,700 K.

Why M stars?

Due to their large numbers, M-dwarf stars are interesting candidates for planet searches in particular, in the habitable zone, a distance from a star where water stays liquid (Tarter et al., 2007). They are also extremely common in the Universe, comprise of 70% of stars in the Milky Way, and relatively small and dim as shown in the H−R Diagram in Fig.1.4, where the luminosity goes down with spectral type. The low mass of M stars yield larger amplitude according to equation 1.5. Due to the small radii, signals from an Earth-sized planet should be distinguishable from transit surveys, for example, Mearth (Nutzman & Charbonneau, 2008) project results in the first super Earth mass planet detection around the 13 pc distant M dwarf GJ1214 (Charbonneau et al., 2009). The smaller size and low effective temperature of the host star also implies that the orbiting planets could fall within the habitable zone relatively nearby the host star. However, M-dwarfs habitability is still poorly understood. The knowledge of habitability can be improved by obtaining larger samples of M dwarfs with photometric all-sky surveys. The Transiting Exoplanet Survey Satellite (TESS) (Ricker et al., 2015) is predicted to find 990±350 planets orbiting 715±255 stars (Ballard, 2018). Yet, it will still need the ground-based RV confirmation to fully characterize this type of stars.

Planet formation theories can be tested by M dwarf planet searches. Several recent studies exhibit compelling results; for example, a study of a terrestrial planet candidate around Proxima Centauri (Anglada-Escudé et al., 2016); a study of rotational velocities of M dwarfs (Jenkins et al., 2009); as well as some exoplanet survey programs using HARPS (Bonfils et al., 2013), the Red-Optical Planet Survey of precision radial velocity of M dwarfs (Barnes et al., 2014). The recent detection of the TRAPPIST system (Grimm et al., 2018) revealed

a number of Earth-sized planets in the habitable zone yet unknown atmosphere to answer whether water and life actually exist on those planets (Wandel, 2018).

The major challenge of observing M dwarfs is that they are intrinsically faint. Nonetheless, infrared spectroscopy is highly efficient, since the flux emitted by M5 dwarfs at 1 μm (Y-band) is several times higher than in the optical regime. To achieve an RV precision of 5 m/s in Y-band, assuming S/N of 100 at 1 μm, requires spectral resolution R of 60,000 for M9 spectral-type (Reiners et al., 2010).

1.2. TAO Telescope

The Atacama desert in the north of Chile is one of the best sites for ground−based astronomy since it offers excellent seeing of 0.69" (Yoshii et al., 2010), low precipitable water vapor $\approx$ 0.5mm and high clear fraction up to 82 % photometric. The University of Tokyo Atacama Observatory (TAO) telescope is a project of the University of Tokyo located at the summit of Co. Chajnantor 5,640 m altitude in northern Chile. At this high altitude, the atmospheric absorption is minimal at the infrared observing window. In Fig.1.5, three observing sites are compared: (top) The TAO site (Co. Chajnantor) at 5,600m, 498 hPa, Precipitable Water Vapour (PWV)=0.5 mm, (middle) the Subaru site (Mauna Kea) at 4,200m, 600 hPa, PWV=1.0 mm, and (bottom) the VLT site (Paranal) at 2,600 m, 737 hPa, PWV=6.0 mm.

The telescope is Cassegrain/Ritchey-Chretien type. The primary mirror, secondary mirror and tertiary mirror are made of borosilicate and light-weighted honeycomb structure. The primary mirror is a circular mirror and concave surface of 6.5 m in size, with a fast beam (f/1.25). The secondary is a circular shape, convex surface of 0.9 m diameter. The tertiary is an elliptical shape mirror and flat surface of 1.1 m x 0.75 m in size. The effective diameter of the primary mirror is 6153.8 mm and the final focal ratio of the telescope is f/12.2. The unvignetted field-of-view is of 25' in diameter and the plate scale diameter is of 2.75"/mm. (Yoshii et al., 2016)

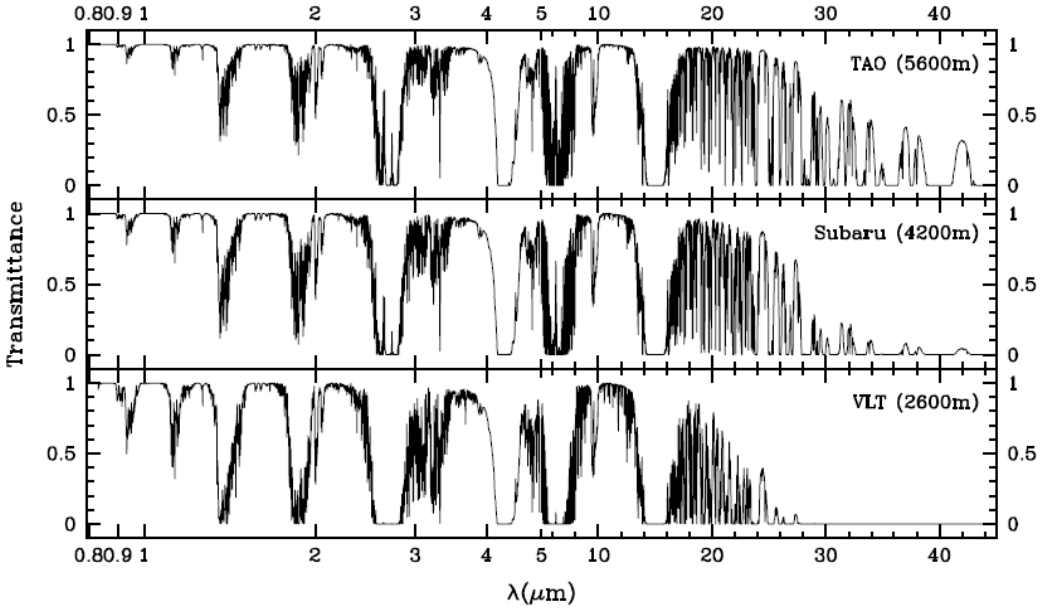

Figure 1.5. Atmospheric Transmittance comparison at the site of TAO, Subaru and VLT from 0.8 to 45 μm. A unique characteristic of the TAO site allows a relatively larger observing window to 45 μm into mid-infrared region (Yoshii et al. 2010).

There are two PI instruments at TAO working in the near-mid infrared i.e. MIMIZUKU: a mid-infrared imager and low resolution spectrograph (Kamizuka et al., 2016), and SWIMS: a wide-field near infrared multi-object spectrograph and imager (Motohara & Yoshii, 2016). However, the observatory lacks a high-resolution spectrograph. TARdYS will expand more science cases for TAO as an exoplanet hunter.

1.3. Novel Near Infrared High Resolution Spectrographs

In general, spectroscopic data in astronomical observation always represents a bottleneck since the spectroscopy generally takes more integration time than other observing techniques. Although there are many spectrographs in operation, only a handful are suitable to observe RV shifts of exoplanets around M-type stars. This is because most spectrographs operate in the visible and M dwarfs are too faint to observe at this wavelength. The fact that their flux

peak in the near infrared complicates the stability of the instrument. In this section, I focus on the novel near infrared high resolution spectrographs currently commissioned.

Table 1.1. Novel near infrared high resolution spectrographs and their specification.

Instrument	λ [μm]	R	Telescope	Calibrator	Precision
NIRSPEC (upgrade)	1.00-5.50	37,500	Keck 10m	Arc Lamps	50 m/s
IGRINS*	1.50-2.50	45,000	Gemini S. 8m	ThAr, UNe	50 m/s
GIANO	0.90-2.50	46,000	TNG 3.5m	UNe	10 m/s
CARMENES	0.52-1.71	80,000	Calar Alto 3.5m	Fabry Perot Etalon	3 m/s
IRD	0.97-1.75	70,000	Subaru 8m	Frequency Comb	1 m/s
HPF	0.85-1.70	60,000	HET 10m	Frequency Comb	3 m/s
SPIRou	0.90-2.40	85,000	CFHT 3.6m	Fabry Perot Etalon	1 m/s

*IGRINS has been on various different telescopes

NIRSPEC

NIRSPEC is an infrared spectrograph developed by UCLA Infrared Laboratory. In one mode, it can measure radial velocity measurements based on an f/10 cross-dispersed echelle spectrograph with 120 mm collimated beam in quasi-Littrow mode. The instrument has been installed at the Keck II telescope since 1999. Recently, the instrument has been upgraded for a higher spectral resolution and a larger spectral grasp from three aspects: detector, slit-viewing camera and control electronics (Martin et al., 2014). Using different types of arc lamps, the instrument yields precision of 50 m/s (BaileyIII et al., 2012).

IGRINS

The Immersion Grating Infrared Spectrometer (IGRINS) is a unique infrared spectrograph due to a special type of the dispersing element, immersion grating, which provides a compact design and minimizes the size of the instrument. It yields a spectral resolution R=45,000 with relatively wide wavelength coverage. IGRINS has a robust design so that it can be commissioned on telescopes of different aperture size and different telescope f-number. Currently (2018), IGRINS is a visiting instrument at Gemini South 8 m telescope. The instrument is

not originally optimized for the exoplanet search yet capable for RVs. Together with post-processing routine, in two exposures, IGRINS provides relative RV with uncertainty of 50 m/s (Mace, Jaffe, Park, & Lee, 2016). This RV capability lead to a recent interesting study on the detection of a Neptune-sized planet around M4.5 star (Mann et al., 2016)

GIANO

GIANO is a near infrared high resolution spectrograph mounted on the TNG 3.5 m telescope since 2012. It is fed by IR-transmitting 85 μm ZBLAN fibers, corresponding to 1.0 arcsecond on the sky. The spectral range covers Y,J,H and K bands with R=50,000. GIANO can reach RV precision of 10 m/s at magnitude H=5 and 50-80 m/s at magnitude H=9 (Carleo et al., 2016).

Recently GIANO has a combined observing program with HARPS-N, a high resolution (R=115,000) visible exoplanet hunter, called GIARPS (GIAno & haRPS) (Claudi et al., 2016). This program will be fruitful to the exoplanet community since it gives a wide spectral range (0.383-2.45 μm) and high spectral resolution for precision radial velocity measurement.

CARMENES

CARMENES is a high resolution R=80,000 spectrograph covering both optical and near infrared regions. It has been installed at the Calar Alto 3.5 m telescope in 2015. The CARMENES radial velocity program aims to observe 324 M dwarfs' orbiting planets. The current study found that the highest RV precision of all M-type dwarfs can be reached in the wavelength range of 0.7-0.9 μm using CARMENES. The instrument yields RV precision to about 3-4 m/s (Reiners et al., 2017).

IRD

IRD is a Japanese Y and J band exoplanet hunter installed on Subaru telescope in Hawaii. Its cryogenic system cools the spectrograph at 70K and optics at 200K and is highly stable at 0.01K. IRD employs the most precise calibrator, a frequency comb, capable of precision of 1 m/s (Tamura & team, 2015). The main goal of IRD is to detect earth-like planets around M

stars and aims to unveil the frequency and properties of the habitable planets. They are targeting late M dwarfs (M4V-M9V), which have large RV amplitudes and short orbital periods. The large collecting area of Subaru 8 m telescope has an advantage on the faintness of the objects. The fiber injection system of IRD is also coupled with an Adaptive Optics (AO) system. This aims to provide coronagraphic high-dispersion spectroscopy employing the combination of extreme AO and coronagraphy, for star light reduction.

HPF

The Habitable-Zone Planet Finder (HPF) is a stabilized fiber-fed NIR Spectrograph for the Hobby-Eberly 10 m Telescope (HET) in Texas, USA. Unlike typical telescopes, the HET main mirror is fixed at a 55 ° angle, and allows only azimuthal rotation. For observing exoplanets, one should keep in mind that the telescope only access to 70 % of the sky (Hill, MacQueen, Palunas, Shetrone, & Booth, 2006). Some tracking can be done by moving the instruments at the focus of the telescope. The maximum track time per night is 5 hours. The HPF project also aims to discover low mass planets around M dwarfs. The cryostat of HPF is cooled to 200K. It is capable to reach RV precision of 3 m/s (Mahadevan et al., 2014).

SPIRou

SPIRou is a high precision near infrared high resolution spectrograph installed at the Canada France Hawaii Telescope (CFHT) in early 2018. The instrument employs a Fabry−Perot Etalon as a calibrator, which provides stability of 1 m/s (Cersullo, Wildi, Chazelas, & Pepe, 2017) for the detection of a planet in the habitable zone around a low-mass star. One special feature of SPIRou is the measurement of spectral polarization. This allows differentiation between the planet and star signals, as the planet spectrum will be polarized. Besides detecting planets in the solar neighborhood, SPIRou will also be used for detecting magnetic fields of stars, studying atmospheres of transiting planets as well as studying the surface cloud models of brown dwarfs.

1.4. Limitation of current search

Finding earth-like exoplanets has been an on-going challenge in the last two decades. It is difficult because the small size of the planet yields very small amplitude K (Eq.1.2) in the signal. The relatively close and small habitable zone of M dwarfs and their abundance makes them attractive hosts. However, this generation of spectrographs have difficulties achieving the sub-meter-per-second precision necessary to detect habitable rocky planet. The three major limitations are:

Budget constraint: the high cost of building an infrared spectrograph limits the number of follow-up instruments for significant samples.

Stability: high-resolution spectrographs are complex precision instruments with dozens of sources of the instrumental error, which must be controlled and minimized. At the same time, a high frequency stability calibrator is required to ensure a more precise measurement.

Stellar Activity Jitter: the stellar surface inhomogeneities caused by starspots, plages, convection, and flares introduce the radial velocity noise especially around young stars. This RV red noise jitter inhibits exoplanet detection or leads to false positives. However, the jitter is smaller in the infrared.

In this work, we balance the science need with the budget constraint. The following chapters will discuss how to build an infrared spectrograph within a limited budget. For the other aspects, they can be briefly discussed as follows:

1.4.1. Instrumental challenge

The most important factors affecting spectrograph are: 1) spectral resolution, 2) stability, 3) efficiency and 4) calibration system.

1) *Spectral resolution*: High spectral resolution ($>$ 60,000) allows disentangle stellar photospheric velocities from orbital velocities because achieving high RV precision can be limited by the apparent RV variation caused by co-rotating features and temporal variations of the stellar surface (Reiners et al., 2010). There are a few methods to boost up the spectral resolution of a spectrograph such as working at high orders using echelle gratings, using image slicers (Vanzi et al., 2018), using adaptive optics fed single mode fiber(Schwab et al., 2016) and using Fabry-Perot interferometer array (Ben-Ami, López-Morales, Garcia-Mejia, Gonzalez Abad, & Szentgyorgyi, 2018).

2) *Temperature and pressure stability*: Thermal expansion modifies the dimensions of the optical elements and could slightly change their position. The refractive indices of optical glasses can be affected by temperature and air pressure perturbations. Thus, it is important to control both factors within some critical range. According to the Munich Spectrograph Stability Project of refurbishing FOCES spectrograph, they apply a simple "box in box" system (Anna Brucalassi, 2013) to stabilize temperature to $<$ 0.01 K and pressure stability $<$ 0.1 hPa in order to search for planets. An alternative versatile technique to reach a sub-mK temperature stability is presented in the HPF spectrograph (Stefansson et al., 2016). The modified model from APOGEE uses the combination of radiation shield, thermal strap, thermal insulation and a robust vacuumed cryostat to create an Environmental Control System (ECS) for HPF project. This method yields 0.6 mK RMS stability over 15 days at 180K and 300K.

3) *Efficiency*: There are several factors that contribute to the system efficiency such as atmospheric transmission, telescope, and system optics that includes fiber illumination issue, guiding and telescope interface unit. To improve the throughput at the spectrograph front-end, several techniques such as fiber core geometry, and coupling fibers (Peter P. Plavchan, 2013) can be applied. Vanzi et al. 2018 demonstrates that upgrading the fore-optics at the telescope

interface unit help increasing the efficiency of the spectrograph. Fast tip-tilt corrector is also being applied to FIDEOS at La Silla Observatory.

4) *Calibration system*: The traditional method for calibrating a spectrograph is using emission lamps e.g. Th-Ar or U-Ne, which last only a few hundred hours and become restrictive. Gas absorption cells are also used for calibrating the short wavelength range of 500 to 630. To go for sub-meter-per-second regime, Laser frequency combs become a potential candidate to use despite their complexity and cost. Schwab (Schwab et al., 2015) introduces an affordable and very promising solution, to use a Fabry-Perot etalon to reach 3 cm/s RV precision.

1.4.2. Data challenge

A good instrument alone is not sufficient for good measurements of a planetary system, particularly to reach high RV precision. The stellar activity can introduce RV variations or jitter. This RV red noise jitter inhibits exoplanet detection or leads to false positives. This noise can be caused by various sources; for example, P-mode oscillations, granulation, spots, activity cycle, and rotational broadening, which happen in different time scales ranging from minutes to decades (Dumusque, Udry, Lovis, Santos, & Monteiro, 2011). In order to remove the corrupting components: stellar activity and noise from RV signal, the model needs to be sufficiently flexible and not swallow the planet signal.

In 2015, the RV fitting challenge (Dumusque et al., 2017) in the Extreme Precision Radial Velocity workshop (EPRVII) evaluated various methods to tackle stellar activity, which can be separated into two sub-groups: empirical and Gaussian processes, a statistically rigorous way to handle red noise.

Secondly, methods for deciding whether an exoplanet signal is statistically significant or not are required. In the EPRVIII challenge, various methods are vetted for their robustness (Nelson et al., 2018). Currently available methods such as BIC and MCMC are insufficient (Ford & Gregory, 2007).

From those two challenges, no current algorithm is statistically rigorous, robust and can handle the red noise. The effect of RV jitter can additionally be combated by obtaining more information on the stellar activity. Two methods are currently promising: 1) simultaneously monitoring stellar activity of the observed star (e.g. R_{HK}) to estimate the activity-induced jitter in radial velocity measurements (Lanza, Boisse, Bouchy, Bonomo, & Moutou, 2011); 2) multi-band RV observations exploiting the wavelength dependence of the spot-caused jitter and the wavelength-independence of the planetary Doppler shift (Ma & Ge, 2012).

1.5. Hypothesis

The design of a high spectral resolution ($>$ 60,000) near infrared spectrograph covering the spectral range of 0.843-1.117 μm combined with a large collecting area of 6.5 m telescope at a very high altitude will be a unique tool for detecting planets around low mass- cool stars. I hypothesize:

- Employing an echelle R6, one can reach a high resolution with a smaller size instrument compared to the conventional R2, R3 or R4 grating options.
- A semi-cryogenic setup and small number of camera surfaces, originally designed for TARdYS, will also contribute to reduce the cost of the instrument.
- The abundance of lines in the wavelength calibration source of Uranium will allow sufficient RV precision of the instrument for detecting planets.

1.6. Objectives

In this study, the scope mainly focuses on the optical design, analysis and test on a prototype. I use the optical ray-tracing program ZEMAX for the modelling and analysis. Before having the parts fabricated, I perform tolerance analysis to evaluate the defects of manufacturing and alignment errors since the spectrograph consists of an infrared detector and a lens to be cooled in cryogenic environment, the system also needs the thermal analysis to evaluate the performance under the low temperature atmosphere.

Then I build a prototype of this spectrograph using the optical elements according to the optical design developed. I design new optomechanical mounts for each optical components. Partly I will also use the commercial mounts for this prototype setup. The prototype will be used to test the performance of different setups of the spectrograph i.e. quasi-Littrow configuration and White Pupil configuration. In this prototype, I will employ a commercial tool infrared detector XEVA 1.7-640-TE3 with Thorium Argon and/or Uranium calibration lamp to test stability of the warm setup of the spectrograph.

1.7. Theory

1.7.1. Gratings

"No single tool has contributed more to the progress of modern physics than the diffraction grating" (Harrison, 1949a).

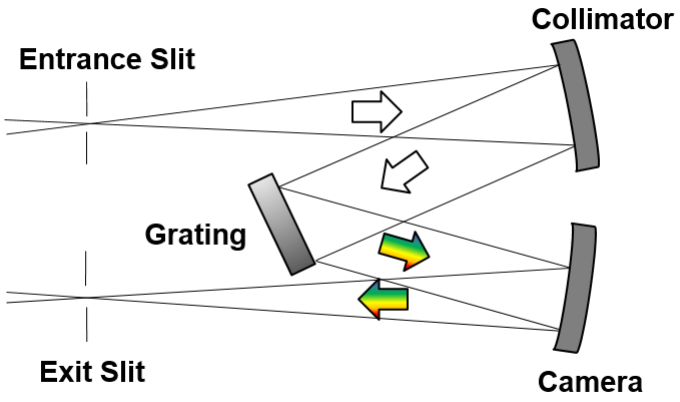

Figure 1.6. An integration of a diffraction grating into a monochromator or a spectrograph (replace the exit slit by a CCD).

The development of gratings began in 1785, in the report of David Rittenhouse while he was explaining the concept of optical deception, he mentioned a chocolate size glass with furrows (Rittenhouse, 1786). This was a prototype of half-inch wide grating with 53 apertures but there was no further evidence of scientific experiments (Palmer, 2014). It was then Joseph von Fraunhofer, who actually used diffraction gratings in his work in 1821 (Fraunhofer, n.d.). He was able to measure absorption lines of the solar spectrum known now as 'Fraunhofer lines'. In 1870, L.M Rutherford investigated reflection gratings made out of speculum metal as his part-time interest (Palmer, 2014). Later H.A. Rowland successfully established spectroscopic technology using gratings as the primary optical element since 1882 (Rowland, 1882). He excelled his ruling engines and introduced the concave grating. In 1921, J.A. Anderson

perfected the **blazed** grating. He succeeded to diffract 50 % of the light into the first order. By 1924, the plane grating, the flat diffraction grating, blazed 600 line/mm was installed at Mt. Wilson by C. Jacomini, the co-pioneer of the blaze grating (Hearnshaw, 2009).

A reflective type grating reflects the diffracted beam into the incident direction as shown in Fig.1.7. The relationship of these angles can be explained using the **grating equation**:

$$m\lambda = d(\sin\alpha + \sin\beta) \tag{1.6}$$

where:

m = diffraction order

λ = wavelength

d = line spacing

α = angle of incidence

β = angle of diffraction

From Eq.1.6 in the case of a constant wavelength, I can differentiate the equation and obtain:

$$\cos\alpha d\alpha + \cos\beta d\beta = 0 \tag{1.7}$$

This relationship can be expressed in terms of **anamorphic magnification** r in Eq.1.8, which is the ratio of the change between the angle of the camera beam and the angle of collimator beam (Schweizer, 1979).

$$r = -d\beta/d\alpha = \cos\alpha/\cos\beta \tag{1.8}$$

If $r \neq 1$ which means $\alpha \neq \beta$, this condition leads to Cassegrain and Coud́e spectrograph. In a special case when the incident angle equals the reflective angle and equals the blaze angle θ_B or γ in Fig.1.7, this condition is called **Littrow configuration** $\alpha = \beta = \theta_B$ and $r = 1$. It

yields the maximum efficiency of the grating and can be expressed as:

$$m\lambda = 2d \sin \theta_B \tag{1.9}$$

1.7.1.1. Echelle grating

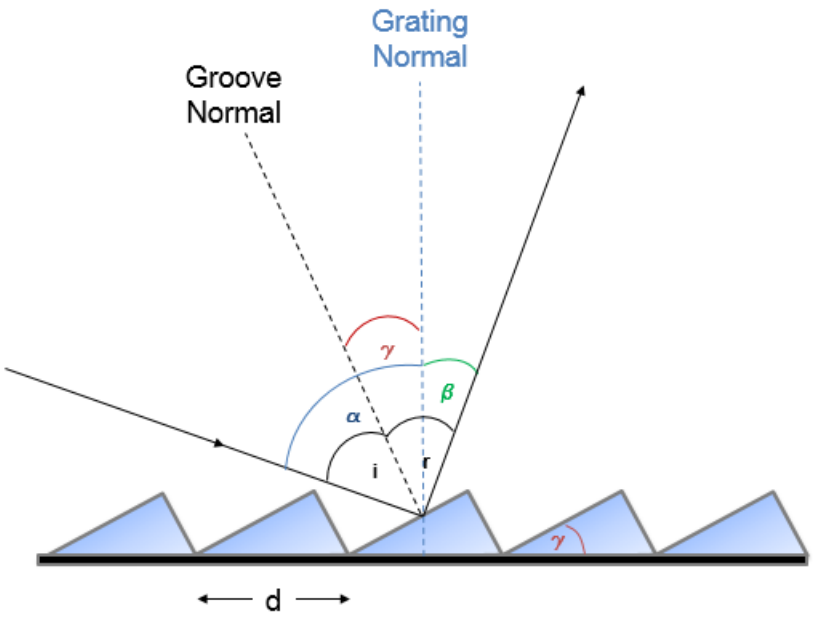

Figure 1.7. Blaze condition where *i* is an angle of incidence and *r* is an angle of reflection.

Echelle grating is a type of blazed grating with a large blaze angle. The modern reflection echelon was introduced by George R. Harrison in 1949. He explained his so called **echelles** grating to have *a simple step groove form that reflects light of all orders in a narrow bundle, and designed to be used at an angle of incidence greater than 45° and normal to the narrow side of the "step"* (Harrison, 1949b). In this work, he developed a large grating with near theoretical resolving power. He also suggested having a suitable prism or grating of low dispersion to avoid overlapping of orders. The tangent of the blaze angle is used to specify

the grating as R-number. For example, a R2 Echelle has a blaze angle = 63.4°. An R4 grating corresponds to 76 °. An R6 Echelle has a blaze angle of 80.5 °.

1.7.1.2. VPH grating

The Volume-Phase Holographic (VPH) Grating[1] is also a type of blazed grating. It usually works in transmission. The grooves are formed in a layer of transmissive material and sealed between two layers of clear glass or fused silica. The grating equation for VPH grating is similar to Eq.1.6. The equation of the VPH grating is represented by:

$$m\nu\lambda = \sin\alpha - \sin\beta \quad , \tag{1.10}$$

where ν is the frequency of the intersection of the grating fringes with grating surface and the other parameters are defined as same as in Eq.1.6.

The light that goes into each order is determined by the **Bragg condition**. A plane-parallel grating with fringes normal to the grating surface is shown in Fig.1.8A (Barden, Arns, Colburn, & Williams, 2000). This configuration can be expressed by:

$$m\nu_g\lambda = 2n_g sin\alpha_g \tag{1.11}$$

where ν_g is the fringe frequency, n_g is the average refractive index of the grating medium, and α_g is the angle of incidence inside the grating respected to the fringe plane. The Bragg condition diffraction in Eq.1.11 of some possible VPH configuration is shown below. Fig.1.8A illustrates the case of a *transmission* grating with fringes perpendicular (γ = 90 degrees) to the grating surface where $\alpha = \beta$. Fig.1.8B exhibits a *transmission* grating with tilted fringes. The case of a *reflection* grating with fringes parallel (γ = 0 degrees) to the grating surface is shown in Fig.1.8C. Lastly, the *reflection* grating with tilted fringes in shown in Fig.1.8D. In TARdYS, I use VPH in littrow configuration (Fig. 1.8A).

Using a VPH grating benefits the performance capability over typical astronomical gratings in various aspects. For example, VPH grating yields almost 100% efficiency at the

[1] http://www.kosi.com/

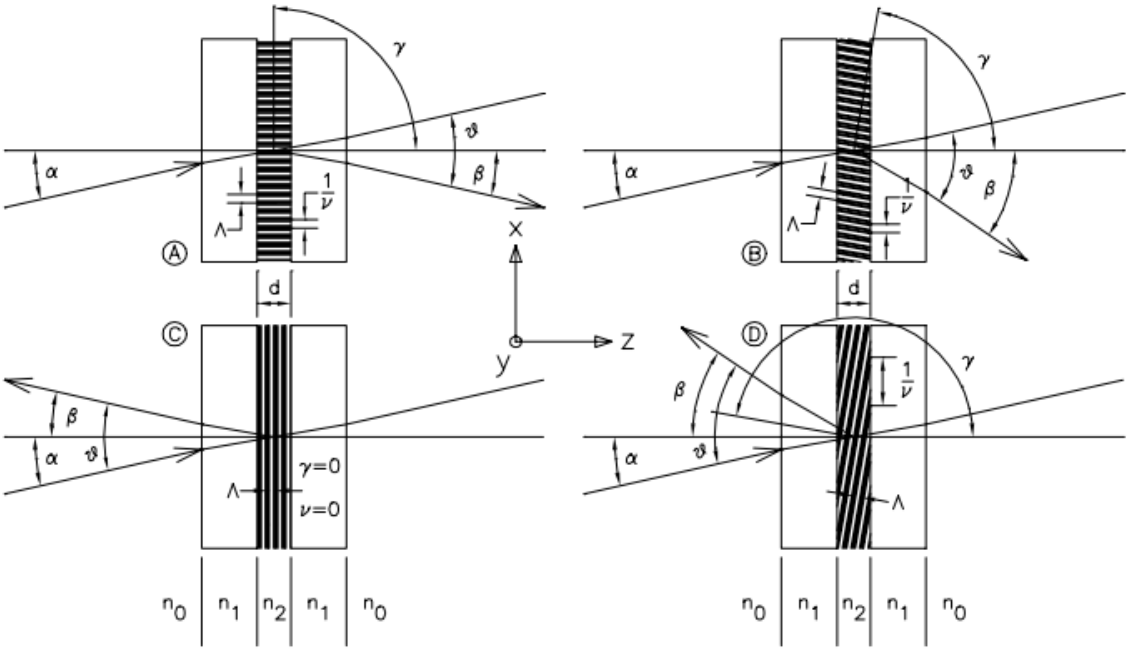

Figure 1.8. Four possible fringe structures for VPH gratings : (A) Littrow transmission grating. (B) Non-Littrow transmission grating. (C) Nondispersive reflection grating (notch filter). (D) Dispersive reflection grating, taken from Barden et al.2000 (Barden, Arns, Colburn, & Williams, 2000).

diffraction peak. The ghost, the image caused by reflections of lenses, and scattered light are significantly reduced. Some VPH gratings can be tuned to shift the diffraction efficiency peak to a desired wavelength. It can be manufactured with higher groove densities, up to 6000 lines/mm while the normal surface-relief (SR) gratings are restricted to line densities less than 1200 lines/mm. The VPH grating is encapsulated between glass material. This allows the grating surface to be cleaned (from outside) and coated with the anti-reflection (AR) coating on the surface. However, the drawback of using the VPH grating is that the wavelength and angular bandwidths will get very narrow for high line density transmission gratings. Second, to generate the higher order of VPH diffraction is still poorly understood and difficult to fabricate. The last concern respecting the spectrograph is that it must have a camera-to-collimator angle that conforms to the VPH grating parameters (Barden et al., 2000).

1.7.2. Dispersion

Dispersion is the separation of rays of different wavelengths. This is illustrated in Fig.1.7. White light comes through telescope, fiber, collimator, then dispersed by grating and lands on a detector where colors/wavelengths are spatially separated. The angular dispersion and linear dispersion can be expressed as follows:

Angular Dispersion: the change of diffraction angle ($d\beta$) corresponding to a change in wavelength ($d\lambda$)

$$\frac{d\beta}{d\lambda} = \frac{m}{d\cos(\beta)} = \frac{\sin\alpha + \sin\beta}{\lambda\cos(\beta)} \quad . \tag{1.12}$$

Linear Dispersion: the change of wavelength over the detector.

$$\frac{dx}{d\lambda} = \frac{d\beta}{d\lambda} f_{cam} = \frac{m f_{cam}}{d\cos(\beta)} \quad , \tag{1.13}$$

where:

α = the angle of incidence

β = the angle of diffraction

m = the diffraction order

d = the line spacing

λ = wavelength of light

$f_{cam} = dx/d\beta$ = the camera focal length

1.7.3. Free Spectral Range

In general, the diffracted λ can overlap between two adjacent orders (m and m$\pm$1). Free spectral range (FSR) shown in Fig.1.9 defines the range of wavelengths in a given spectral order where the superposition of light from the neighboring order does not occur. The free spectral range is given by:

$$\Delta\lambda_{FSR} = \frac{\lambda}{m} \quad . \tag{1.14}$$

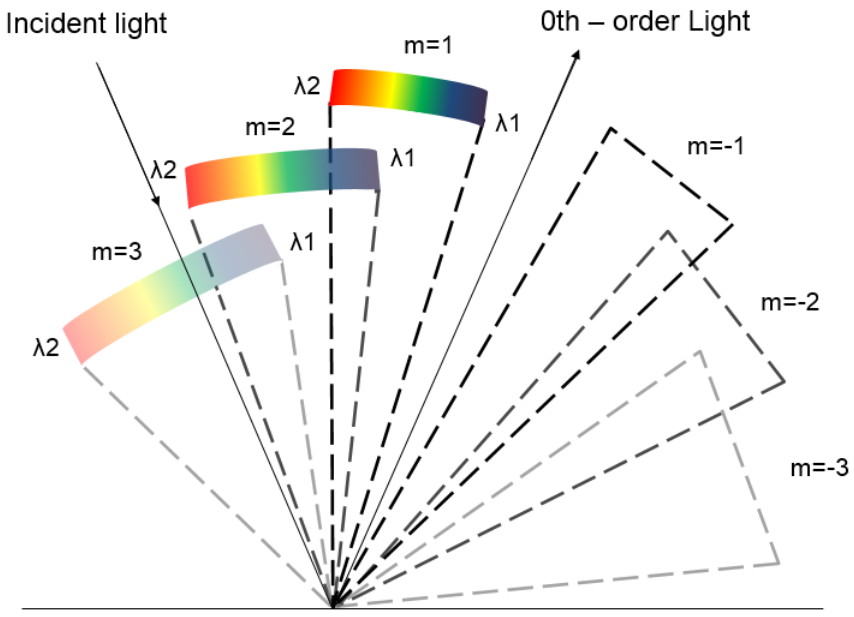

Figure 1.9. The partially overlapping spectral orders when disperses with the diffraction grating.

Then one can calculate the order separation (Δy) after the camera of focal length f_{cam} as follows:

$$\Delta y = f_{cam} \frac{d\beta}{d\lambda_{XD}} \Delta\lambda_{FSR} \quad , \tag{1.15}$$

where $d\beta/d\lambda_{XD}$ is the angular dispersion of the cross-disperser, the second dispersing element used to avoid the overlapping orders.

1.7.4. Resolving power

The resolving power R is related to the ability to separate adjacent spectral lines of average wavelength, and is defined as:

$$R = \frac{\lambda}{\Delta\lambda} \quad , \tag{1.16}$$

where $\Delta\lambda$ is the smallest difference in wavelength that can be distinguished at the wavelength λ, in other words, how well spectral lines are resolved.

Diffraction Limit is the resolution of an optical system limited by limiting edges of the optical elements. In terms of diffraction grating, the diffraction limit can be derived from the grating equation (Eq.1.6). In the grating equation, the parameter *d* represents the line spacing which also equals to number of grooves *N* along the grating length *L*. Thus Eq.1.6 becomes

$$m\lambda = \frac{L}{N}(\sin\alpha \pm \sin\beta) \quad . \tag{1.17}$$

If one differentiate the above equation and let the beam diameter on the collimator $D_{col} = L\cos\alpha$ and the diffraction limited angular slit size $\delta\alpha \approx \lambda/D_{col}$. Then the largest possible resolution due to the diffraction limit is

$$R = mN \quad . \tag{1.18}$$

Slit Limited: the entrance slit width of the spectrograph can also determine the spectral resolution. In the case that the anamorphic factor = 1 (Littrow Configuration), one can obtain the relationship between slit width δf and image width δl as

$$\delta l = M\delta f \tag{1.19}$$

where the magnification $M = f_{cam}/f_{col}$.

From the linear dispersion equation (Eq.1.13) when $\alpha = \beta = \theta_B$, then:

$$\Delta\lambda = dx\frac{d\cos(\beta)}{mf_{cam}};\ dx = \delta l \quad . \tag{1.20}$$

Then, I substitute λ from Eq.1.6 and $\Delta\lambda$ from Eq.1.20, the maximum spectral resolution then becomes

$$R = 2\frac{f_{cam}}{\delta l}\tan\theta_B = 2\frac{f_{col}}{\delta f}\tan\theta_B \quad , \tag{1.21}$$

where:

m = diffraction order

θ_B = grating blazed angle

f_{cam} = focal length of the spectrograph camera

f_{col} = focal length of the spectrograph collimator

δf = slit width

δl = image width

1.7.5. Fiber-coupled Spectrograph

Optical fibers have proved to be critical to reach high stability. For precision RV measurements, it is useful not to have the instrument attached to the telescope focal plane. In Fig.1.10, the illustration shows the coupling of the telescope system with a spectrograph. One drawback doing that is the loss of efficiency mostly because of the **focal ratio degradation** (FRD) (Ramsey, 1988). This effect was first described by Angel et al. (1977) who examined the properties of fused-silica fibers in their transmission as a function of wavelength in the optical and IR regions as well as the effect of fiber propagation on the focal ratio in an astronomical spectrophotometer (Angel, Adams, Boroson, & Moore, 1977).

The effect occurs when an output focal ratio F_{out} is faster (higher) than the input focal ratio F_{in}, given D_{tel} (as shown in Fig.1.10) is the telescope diameter and D_{col} is the beam size at the collimator. Then

$$F_{in} = \frac{f_{tel}}{D_{tel}} \quad , \tag{1.22}$$

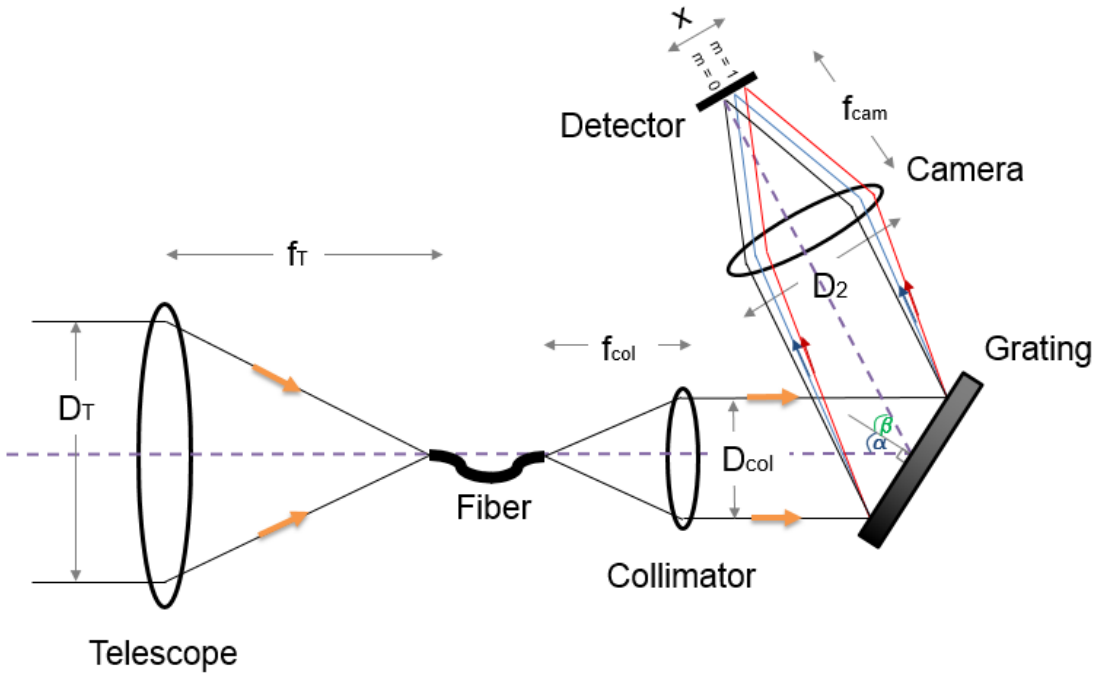

Figure 1.10. This illustration shows a fiber-fed spectrograph connected to the telescope. The fiber link has optics to match F-ratio to telescope and collimator. The arrows show the direction of the light ray from telescope to fiber, collimator then disperse at the grating. The dispersion of the diffraction orders can be observed using a detector.

$$F_{out} = \frac{f_{col}}{D_{col}} \quad . \tag{1.23}$$

The focal ratio degradation (FRD) can be described in terms of ρ

$$\rho = \frac{F_{in}}{F_{out}} \quad . \tag{1.24}$$

2. SENSITIVITY SIMULATION AND EXPOSURE TIME CALCULATOR

The Exposure Time Calculator (ETC) plays an important role in accurately estimate the feasibility of astronomical observation and achieve the required Signal to Noise (S/N). Most novel astronomical spectrographs, for example MOSFIRE [1] , FEROS [2] and HARPS [2] , are usually accompanied by an Exposure Time Calculator for users.

Here I develop an exposure time calculator for TARdYS. The TARdYS ETC adapts a sensitivity simulation concept as IGRINS Exposure Time Calculator (Le et al., 2015). While IGRINS works in the near infrared H and K band, I adjust the working wavelength to Y and J band. The sensitivity simulation method in both calculators take into account the atmospheric transmission, thermal emission, throughput of telescope, instrument optics as well as the dark current and read out noise of the Teledyne infrared detector arrays. In this chapter, I discuss the parameters using in the simulation in section 2.1 and the concept of the TARdYS ETC in section 2.2.

2.1. Sensitivity Simulation

The Sensitivity Simulation basically simulates the observational environment and observing conditions from the observing object, atmosphere, telescope and spectrograph until the detector surface. This section explains each parameter implemented in the sensitivity simulation: atmospheric transmission, OH transmission, system throughput and background emission. The simulation method is also presented.

2.1.1. Atmospheric Transmission

In the optical region, light can travel almost unimpeded through the atmosphere. This is not true for the infrared astronomical observations. Spectra taken from ground based observatory are always affected by molecules from earth atmosphere sometimes, so-called telluric

[1] https://www2.keck.hawaii.edu/inst/mosfire/etc.html
[2] https://www.eso.org/observing/etc/

Table 2.1. Major Atmospheric Gas Composition

Gas Name	Formula	Volume in percent	Absorption
Nitrogen	N_2	78.084	No
Oxygen	O_2	20.094	MW, visible
Argon	Ar	0.934	No
Water vapor	H_2O	0.001-5	MW to near IR
Carbon Dioxide	CO_2	0.035	mid IR
Methane	CH_4	0.00017	mid IR
Nitrous oxide	N_2O	0.000031	mid IR
Ozone	O_3	trace to 0.0008	mid IR
Carbon Monoxide	CO	trace to 0.000025	minor

(Saunders, 1996) and (Mackenzie, 2003)

molecules. The main atmospheric gases absorbing or emitting in the IR are CO_2, H_2O, O_3, CH_4, N_2O, CFCs. To get a precise determinations of molecular abundances from planetary observations with ground based telescopes, the effects of the Earth's atmosphere need to be accurately removed by taking the spectrum of interest and dividing it by a telluric standard (Cotton, Bailey, & Kedziora-Chudczer, 2014). However, to make this subtraction for high-resolution infrared spectrographs, a suitable high resolving power atmospheric characterisation is necessary. It requires a high resolving power of R $(\lambda/\Delta\lambda) > 100{,}000$ to perform a proper telluric division because the shapes of the telluric lines are governed by the instrumental profile and not fully resolved (Seifahrt et al., 2010).

The strongest absorption lines, belong to some of the species; namely water vapor (H_2O), Carbon dioxide (CO_2), Methane (CH_4), and Nitrous Oxide (N_2O)(Seifahrt et al., 2010) and (Bailey, Simpson, & Crisp, 2007). The fraction of these gases is shown in Table 2.1. The amount of water in the atmosphere is crucial for ground spectroscopic observation since the variation of water vapor content can vary the strength of absorption features. Carbon dioxide (CO_2), Methane (CH_4), and Nitrous Oxide (N_2O) are potent greenhouse gases especially the CO_2 which has its levels rising worldwide and seasonally various with other short-term influences. Figure 2.1 is an example case of Atmospheric Condition at Cerro Paranel. The

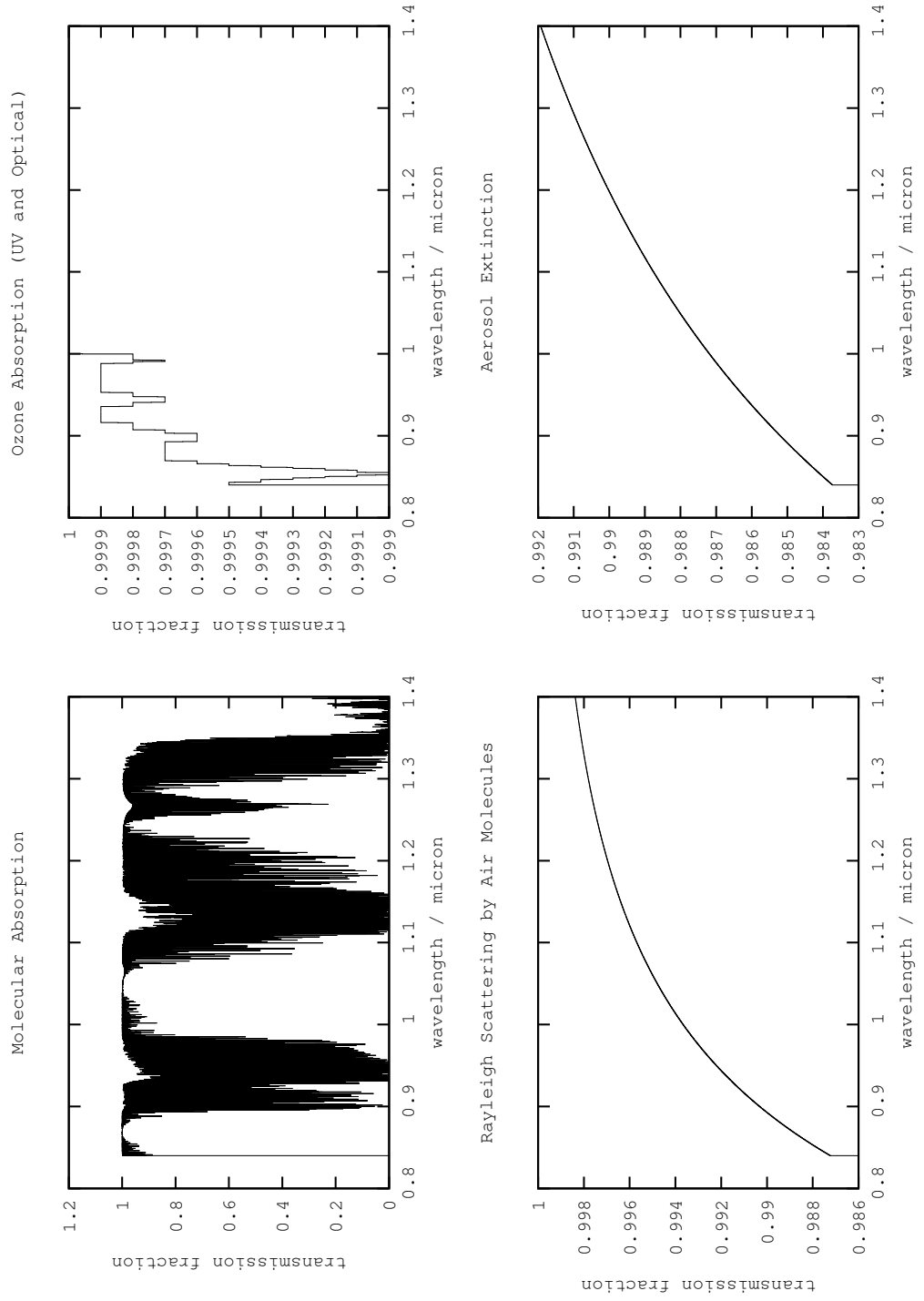

Figure 2.1. Atmospheric Condition at Cerro Paranal

molecular absorption shown in upper left corner covers Y and J windows within the white area.

In order to extract the real spectrum of astronomical objects, one has to remove these atmospheric absorption features from the observed spectra. The traditional practice would be dividing the featureless observed spectrum of standard star into the observed spectrum of the object. The practical difficulties of doing that are: 1) The interpolation techniques using for featureless spectra of early-type stars cannot properly correct the spectrum in the hydrogen lines vicinity, 2) The air-mass differences between standard star and observed object leads to differences in the strength of the molecular absorption features, and 3) The variety of the strength of absorption features due to the water content. These are major problems that limit the S/N achievable in ground-based IR spectroscopy (Bailey et al., 2007).

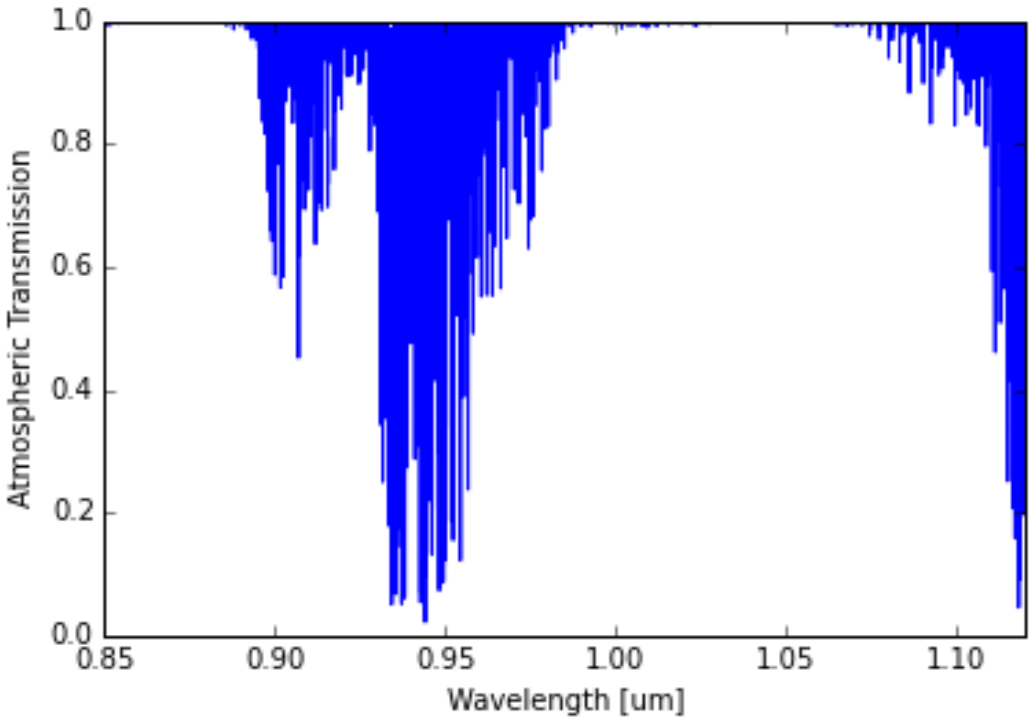

Figure 2.2. ATRAN atmospherica transmission setup to be at TAO observatory at the altitude of 5,640 m. with number of atmospheric layer = 2 (default), wavelength range from 0.86-1.2 μm and resolution R = 60000.

For the atmospheric transmission information, I obtain simulated data from ATRAN (Atmospheric TRANsmission) (Lord, 1992), which is part of a project SOFIA, a NASA's Stratospheric Observatory for Infrared Astronomy. At the stratosphere altitude level (10-50 km above sea level), the presented water vapor is at densities of approximately 2-10 parts per million [3] . This can be translated into a precipitable water vapor level of about 7 μm, which is already sufficient to have an effect on infrared observations. ATRAN uses several detailed atmospherical models including the mix of gases, water vapor, and ozone to predict water vapor overburden at the zenith. It allows accurate calculations of atmospheric transmittance from altitudes ranging from 0 to 30 km and covers wide wavelength range from near infrared to far infrared (0.8 to 10,000 μm). The water vapor burden is affected by the season, latitude, the jet stream and local weather, especially at lower altitude. The setup parameters of the simulation is according to the altitude and closest location of TAO observatory, number of atmospheric layer = 2 (default), wavelength range from 0.86-1.2 μm and resolution R = 60000. This results in Fig. 2.2.

2.1.2. OH Transmission

The Hydroxyl radical was first observed in 1950 (Meinel, 1950). Its bright airglow is produced by a chemical reaction of hydrogen and ozone in the Earth's atmosphere. Emission lines produced by the OH radical dominate background radiation source in the near infrared spectra. They appear between 0.61 and 2.62 μm. Bright lines appear above 1.5 μm and can yield a relative intensity in excess of 2000 proportional to the photon flux. The relative and absolute intensities of these lines are time dependent (Rousselot, Lidman, Cuby, Moreels, & Monnet, 2000). Fig. 2.3 shows the night sky synthetic spectrum of OH emission. Some studies reported the measurement OH airglow lines to be used for the calibration for spectrometers according to (Oliva & Origlia, 1992) and (Osterbrock, Fulbright, & Bida, 1997) since they can provide a useful wavelength reference of about 100 bright and isolated lines between 1.07 μ m and 2.25 μm to be used with low resolution (R $\geq$ 1000) instruments. The list of OH lines can be used to choose narrow band filters in order to reject the strong sky lines.

[3] https://www.sofia.usra.edu/science/instruments/water-vapor-monitor

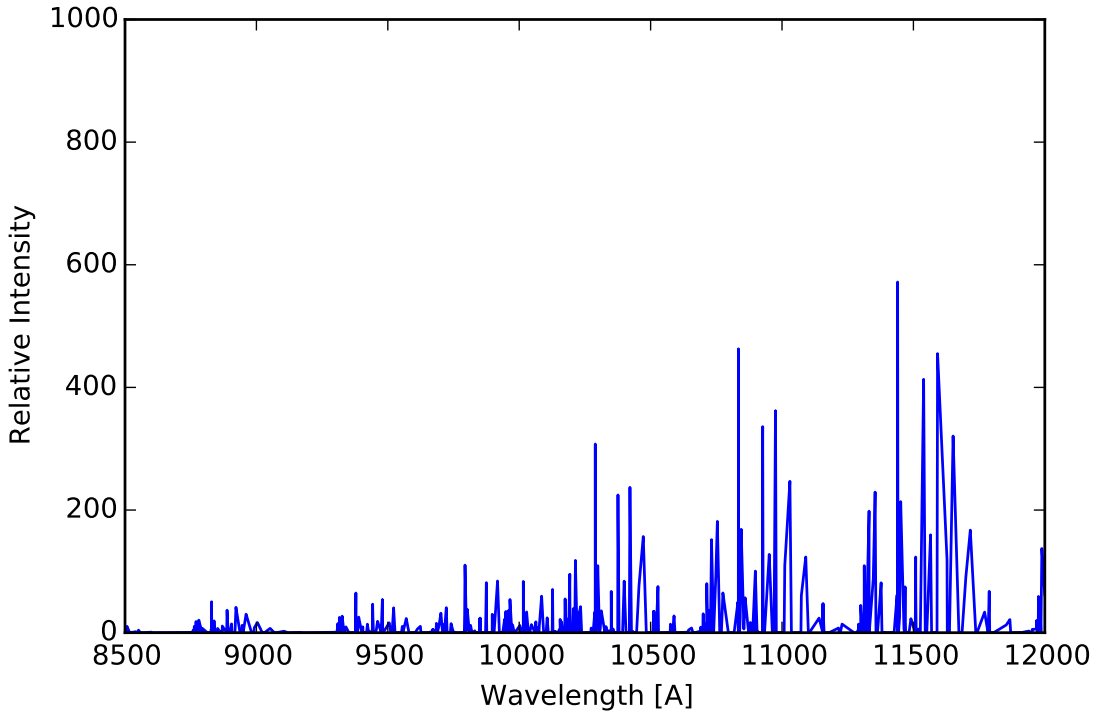

Figure 2.3. General synthetic spectrum of the night-sky OH emission from Rousselot, P. et al. 2000. The relative intensity is proportional to the photon flux.

Table 2.2. Infrared Bandpass (UKIRT)

Bandpass	$\lambda[\mu m]$	$\lambda_1 - \lambda_2[\mu m]$
Y	1.02	0.97-1.07
J	1.24	1.13-1.42
H	1.65	1.53-1.81
K	2.20	2.00-2.41
L'	3.77	3.50-4.10
M'	4.67	4.55-4.80

For near-infrared observations, particularly through the atmospheric window J and H bandpass (Table. 2.2 (Hillenbrand, Foster, Persson, & Matthews, 2002) and (Simons & Tokunaga, 2002)), the OH airglow contribute 92-98% and 98% of background emission (Maihara et al., 1993) and (Herbst, 1994). Removing this component could reduce the sky surface

brightness. The elimination of this noise results in a significant improvement in sensitivity to faint objects (Paul Martini, 2000).

2.1.3. Throughput

For this work, the TARdYS ETC simulates dual astronomical photometric band: Y (0.85-1.12 μm) and J (1.12-1.4 μm). The throughput parameters are basically the efficiency from every component along the light path from the atmosphere, telescope, fiber input, spectrograph optics: doublet, collimator, echelle, VPH, camera and detector. The throughput parameters are shown in Table 2.3. I simulate the system efficiency of 10 $\%$.

Table 2.3. Spectrograph efficiency budget

Parameter	Efficiency
Atmosphere	0.85
Telescope Mirror	0.55
FRD (slitloss)	0.75
Doublet (Input)	0.85
Collimator	0.85
Echelle	0.55
VPH	0.90
Camera	0.90
Cut off filter	0.95
Cold window	0.95
Detector	0.80

2.1.4. Background emissions

The background emission is calculated from zodiacal light, the moon light, OH emission lines, and thermal emission from the atmosphere. One can define the solid angle on the sky viewed by one pixel as

$$A\Omega = \pi\left(\frac{D_{tel}}{2}\right)^2\left(\frac{W_{slit}/n_{slit}}{206265}\right)^2 = 3.12\times10^{-11}[m^2 srpixel^{-1}] \tag{2.1}$$

In this case, I employ a 50 μ m fiber, which correspond to 0.4 arcsecond on the sky. I use this number as W_{slit} and n_{slit} is 2 pixels sampling. Thus I obtain $A\Omega = 3.12\times10^{-11}[m^2\ sr\ pixel^{-1}]$ and plug into 2.2.

$$\epsilon_{Zod,Moon,OH} = A\Omega\tau_{extend}\frac{\lambda_0}{\Delta\lambda_{BW}R}(\Phi_{Zod} + \Phi_{Moon} + 0.1\Phi_{OH}) \tag{2.2}$$

where τ_{extend} is the total throughput for an extended source, R is spectral resolution, λ_0 is central wavelength of Y and J band, $\Delta\lambda_{BW}$ is the band width of the filter, Φ_{Zod}, Φ_{Moon}, and Φ_{OH} are photon fluxes from the Zodiacal light, Moon light and OH airglow shown in Table 2.4.

For Cerro Chajnantor, the site study result from (Giovanelli et al., 2001) has shown a comparison between simultaneous measurements at Cerro Chico (a plateau near Chajnantor) and Cerro Paranal indicates that seeing at Cerro Chico is about 12% better than at Paranal. The percentage of optically photometric nights in the Chajnantor region is about 60%, while that of nights useful for astronomical work is near 80%. The exponential scale height of the water vapor density in the median Chajnantor atmosphere is 1.13 km; the median PWV is 0.5 mm above an elevation of 5750 m (?, ?). However, Cerro Paranal is a well studied site with a lot of site's characteristic information and is nearby Cerro Chajnantor. Thus, we obtain some important parameters from ESO's Skycalc. The library of telluric transmission spectra with various resolutions and atmospheric conditions has been calculated with the Cerro Paranal Advanced Sky Model. A description of the usage of the spectra is discussed in (Moehler et al., 2014). I chose the input configuration of Cerro Paranal (Noll et al., 2014) and (Jones, Noll, Kausch, & Kimeswenger, 2014) as it has similar conditions as Cerro Chanajtor as follows:

Observatory Height: : 2640 m above sea level
Altitude of Target above Horizon: : 90°
Airmass: : 1.00
Season: : Entire Year
Time Period: : Entire Night

Table 2.4. Background emission parameters

Parameter	Y band	J band	Unit
Central wavelength	1.0	1.25	μm
Zero Magnitude Flux density	2.03e-23	1.56e-23	$W\ m^{-2}Hz^{-1}$
Zodical light at latitude 0°	130	110	$photon\ s^{-1}m^{-2}arcsec^{-2}$
Zodical light at latitude 30°	70	60	$photon\ s^{-1}m^{-2}arcsec^{-2}$
Zodical light at latitude 60°	48	40	$photon\ s^{-1}m^{-2}arcsec^{-2}$
Zodical light at latitude 90°	42	35	$photon\ s^{-1}m^{-2}arcsec^{-2}$
Half moon light	115	70	$photon\ s^{-1}m^{-2}arcsec^{-2}$
Full moon light	1500	100	$photon\ s^{-1}m^{-2}arcsec^{-2}$
Ambient Temperature	275	275	K
Detector read noise	5	5	$electron$
Detector dark current	0.02	0.02	$electron\ s^{-1}$

Flux density based on UKIRT; one Jansky represents an incident energy flux density of $10^{-26}W\ m^{-2}Hz^{-1}$
For Zodical light, I assume the heliocentric ecliptic longitude is $\pm 90°$

PWV: : Seasonal Average

Monthly Averaged Solar Radio Flux: : 130.00 sfu

Components included in the radiance model: :

Scattered Moonlight:

- separation of Sun and Moon : 90 degrees
- separation of Moon and object : 45 degrees
- altitude of Moon above horizon : 45 degrees

Scattered Starlight

Zodiacal Light:

- heliocentric ecliptic longitude of object : 135 degrees
- ecliptic latitude of object : 90 degrees

Molecular Emission of Lower Atmosphere Emission Lines of Upper Atmosphere

Airglow/Residual Continuum

Wavelength grid:

- Range: 840.00 nm - 1400.00 nm
- Fixed spectral resolution R=60000

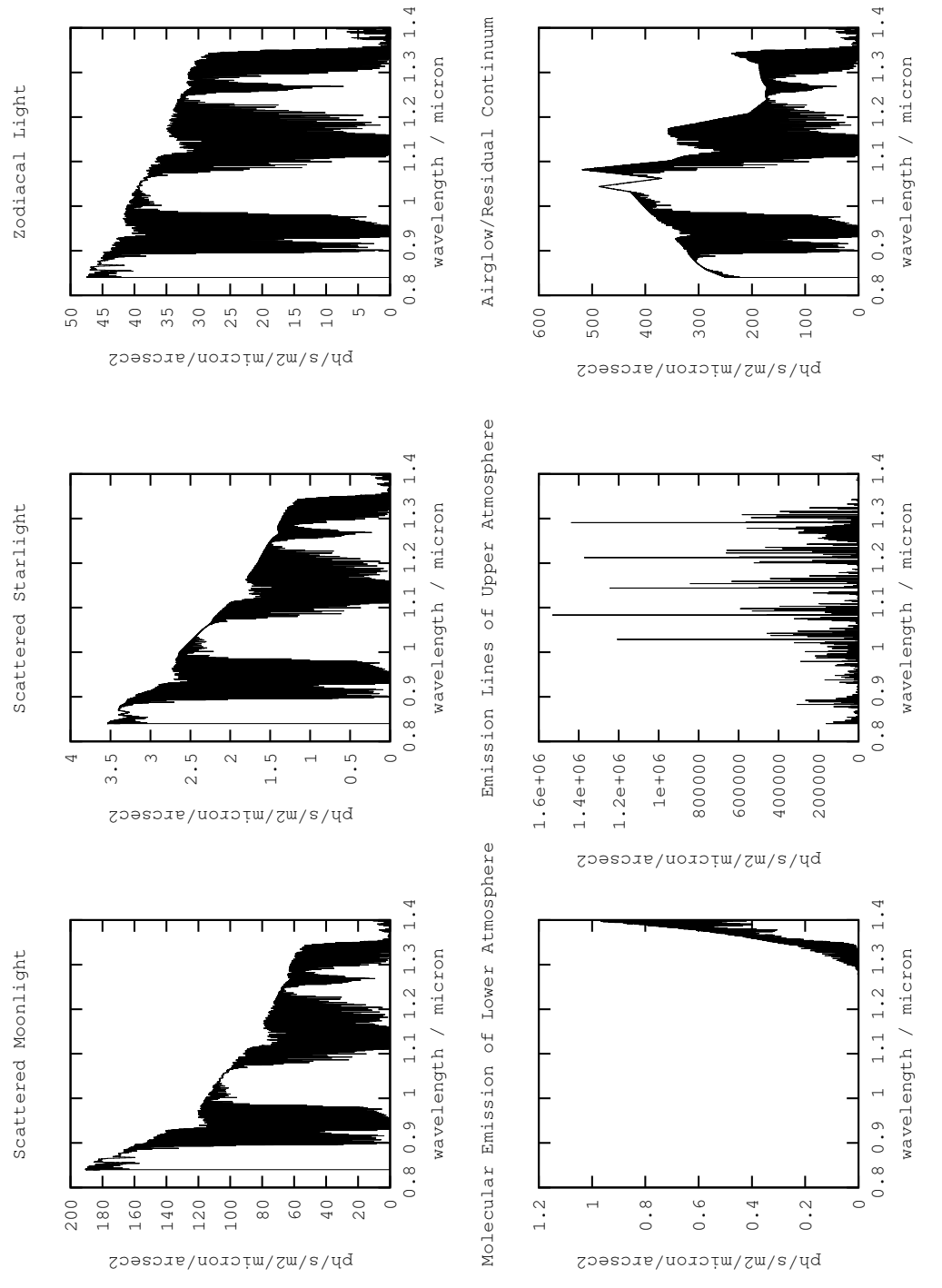

Figure 2.4. The result of Moonlight, Starlight, Zodical light, Emission and Airglow radiance from Skycalc.

In the simulation, I average the Zodical light from Skycalc of different latitude (example result in Fig. 2.4)and apply in the simulation Φ_{Zod} = 72.5 and 61.25 for Y and J band respectively. I include moon light in three separate cases: no moon, half moon and full moon phases. The OH value is included in the form of summation of OH line intensity in Y and J band $\Phi_{OH} = 600 \quad photons^{-1}m^{-2}arcsec^{-2}$

2.1.5. Blackbody Object

The main observing targets are stars and planets. Often, they are modeled as a black body, an object that absorbs all incident electromagnetic radiation while maintaining thermal equilibrium. The radiation emitted from these bodies thus called black-body radiation. The black-body flux can be calculated with Planck's law (Rybicki & Lightman, 1979)

$$B_\nu(T) = \frac{2h\nu^2/c^5}{exp(h\nu/kT) - 1} \quad erg\ s^{-1}cm^{-2}Hz^{-1}sr^{-1} \tag{2.3}$$

where
h is Planck's constant $(6.6260693 \times 10^{-34}\ W\ s^2)$
c is the speed of light $(2.99792458 \times 10^8\ m\ s^{-1})$ and
k is Boltzmann's constant $(1.380658 \times 10^{-23}\ J\ K^{-1})$

Under the assumption that stellar objects behave according to the blackbody thus their spectra are continuous. Figure 2.5 plots blackbody spectra of different temperatures. The peak of the blackbody curve in a spectrum moves to longer wavelength for cooler objects. At T $\approx$ 3000K, representing a spectrum of M stars, it has a peak at 1000 nm in the near infrared region in Fig.2.5. This peak can also be calculated using Wien's displacement law in Eq. 2.4.

$$\lambda_{max} = \frac{b}{T} \tag{2.4}$$

where T is the absolute temperature in kelvins. b is a Wien's displacement constant equals $2.8977729 \times 10^{-3} m \cdot K$. An example case of a cool star with temperature 3000 K: $\lambda_{max} = 2.9 \times 10^{-3} m \cdot K / 3000 K$ gives $\lambda_{max} = 1 \mu m$.

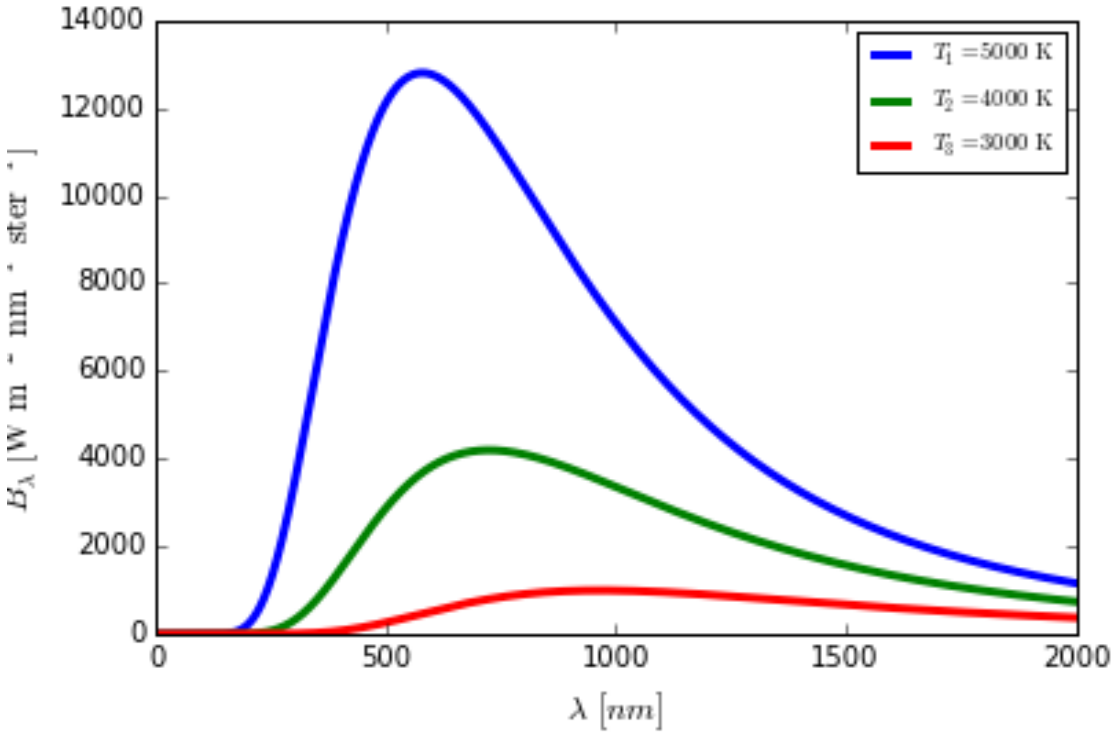

Figure 2.5. Blackbody depending on Temperature

The blackbody flux is included in the simulation as the thermal flux according to equation:

$$\epsilon_{thermal} = A\Omega\epsilon\frac{B_{\nu,T}}{hR} \quad electrons\ s^{-1}\ pixel^{-1} \tag{2.5}$$

where A is aperture of the telescope, Ω is the solid angle on the sky viewed by one pixel, $B_{\nu,T}$ is the Planck function of frequency ν, T is temperature and R is spectral resolution. Then the total emissivity ϵ is defined as

$$\epsilon = \frac{(1-\tau_{atmo}) + [\epsilon_{mirror} + (1-\tau_{window})/\tau_{window}]/\tau_{mirror})}{\tau_{atmo}} \tau_{FRD}\tau_{point} \tag{2.6}$$

This equation 2.6 is adapted from equation 7 from (Le et al., 2015) but instead of using slit loss value, I apply Fiber Ratio Degradation (FRD) value as τ_{FRD} (priv. comm. with Dan Jeffe) and τ_{point} is the total throughput for the point source.

2.2. Exposure Time Calculator

With the sensitivity simulation and all initial parameters mentioned above, I create a python code and implement a user-interface Exposure Time Calculator to calculate signal to noise for various observing conditions in particular for observing at TAO.

2.2.1. S/N Calculation Method

In spectrometry, there are two classes of radiation sources: continuum sources and line sources. The continuum sources emit in a wide range of wavelengths from heated solid material. The line sources are designed to emit discrete wavelengths specific to the lamp's material including laser. For the continuum sources, I calculate the continuum signal using

$$S_{Cont} = \frac{n_{exp} t_{exp} A \tau_{point} S_{ZM} 10^{-0.4m}}{hR} \tag{2.7}$$

S_{Cont} is calculated in the unit of electrons per resolution element, n_{exp} is the number of exposures, t_{exp} is the exposure time, $A = \pi(D_{tel}/2)^2$, S_{ZM} is the flux density at zero magnitude in units of $Wm^{-2}Hz^{-1}$ depending on the photometric band, τ_{point} is total throughput of the point source, m is the apparent magnitude of the continuum source, h is Planck's constant, and R is spectral resolution.

The noise can be calculated from:

$$N_{Cont} = [2n_{slit}^2 n_{exp}\{t_{exp}(\epsilon_{Zod,Moon,OH} + n_{dark} + \epsilon_{thermal}) + n_{read}^2\} + S_{Cont}]^{1/2} \tag{2.8}$$

where N_{Cont} is in units of electrons per resolution element, n_{slit} is pixel sampling along the pseudo slit. $\epsilon_{Zod,Moon,OH}$ is the background emission from Eq. 2.2. n_{dark} and n^2_{read} are dark current and read out noise from detector array respectively. $\epsilon_{thermal}$ is the thermal background from Eq. 2.5 and S_{Cont} is from Eq. 2.7.

For emission lines, I follow the definitions from (Pak et al., 2004) for the calculation of integrated line flux of signal and noise as follows:

$$S_{Line} = \Delta\lambda_{pixel} \sum_i (f_{L,i} - \bar{f}_c) \tag{2.9}$$

$$N_{Line} = \Delta\lambda_{pixel} \sigma(f_{C,i}) \sqrt{n_L(1 + 1/n_C)} \tag{2.10}$$

where $\Delta\lambda_{pixel}$ is the pixel width at the line center, $f_{L,i}$ is the line flux data samples, index i is labeled over the individual samples along the spectra , $f_{C,i}$ is the integrated flux over the continuum, $\bar{f_C}$ is the average of the $f_{C,i}$. The noise part is derived from the standard deviation $\sigma(f_{C,i})$ of $f_{C,i}$ where n_L and n_C are the numbers of spectral samples in the emission and continuum bands respectively.

This method is used to generate three modes for Signal to Noise (S/N) simulation via graphical user interface:

S/N Calculation: Within this mode, the user can assign input of exposure time, number of exposure, seeing and moonlight condition as well as the certain magnitude and background temperature of the observing object. The ETC simply calculates average S/N for Y and J bands by assuming a point source target.

S/N vs. Magnitude: For the magnitude calculation, the user can assign the magnitude range needed. The ETC will give an output of calculated S/N versus limiting magnitude as shown in Fig.2.6. The S/N of Y and J band is calculated. Note that the Y band flux is calculated from the J band user input.

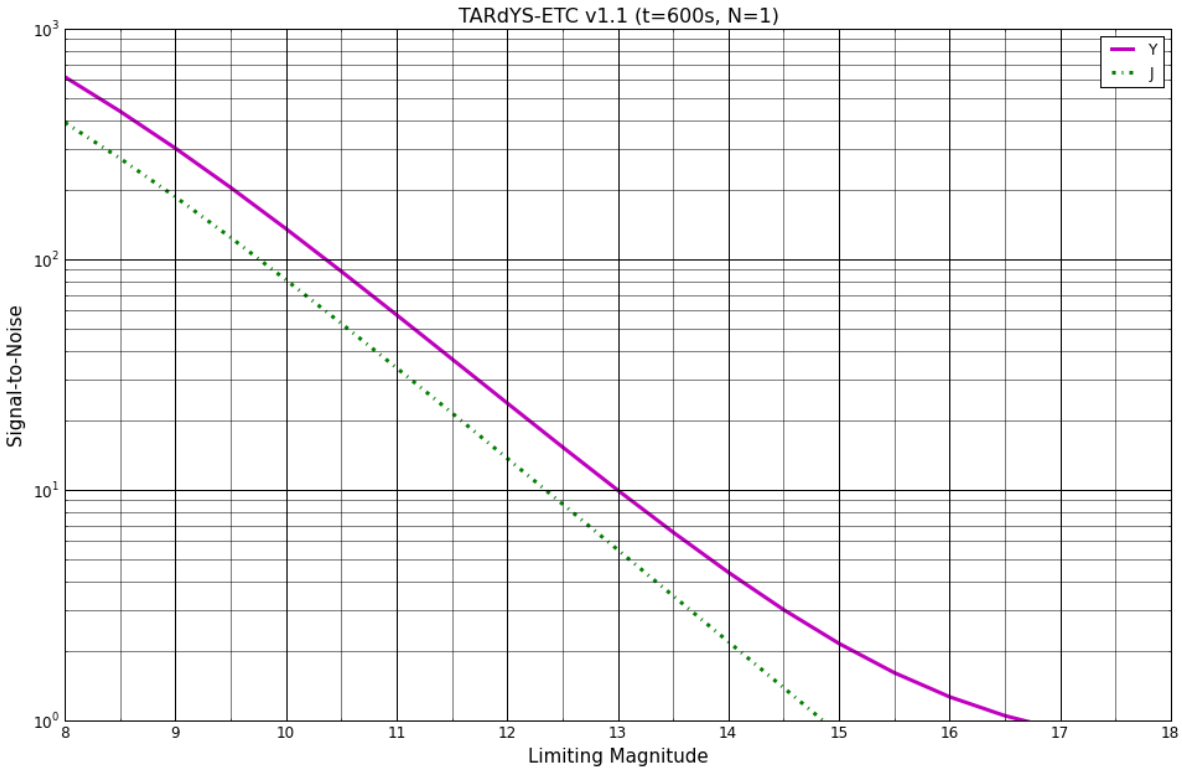

Figure 2.6. The result of the sensitivity simulation in S/N vs. Magnitude mode in the case of 10 minutes exposure time, PWV is 1.0 mm and no moon. The purple solid line is resulting Y band calculation. The green dotted line indicates the calculation in J band.

S/N vs. Wavelength: This mode can receive information of emission lines: rest wavelength, line flux, Doppler shift and line width, in order to simulate S/N versus the resolution element along the working wavelength of the spectrograph. The calculated result is shown in Fig.2.7

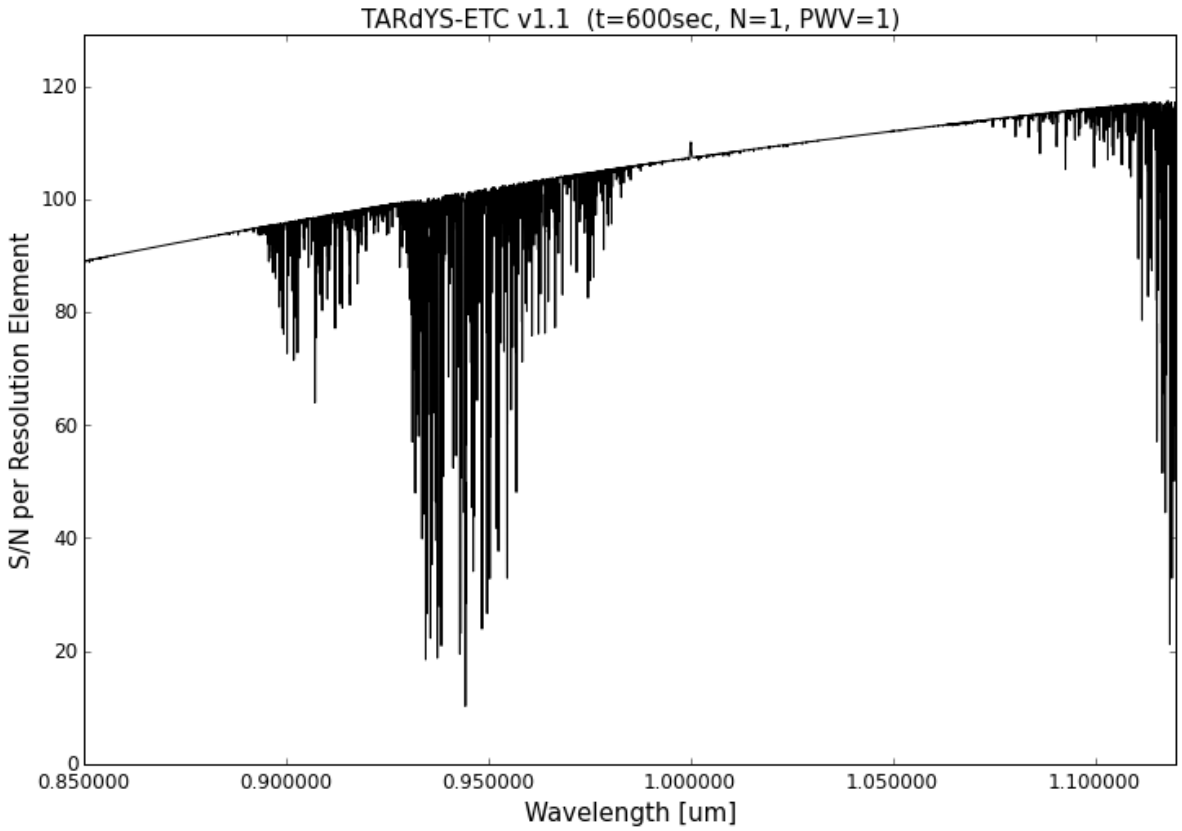

Figure 2.7. The plot shows S/N per Resolution element along the working wavelength of the spectrograph covers Y band. The trend of this plot includes the atmospheric transmission effect and follows the blackbody spectrum of M type star which has blackbody temperature of about 3,000K

2.2.2. User Interface

The second step of making the sensitivity simulation become more user-friendly is to implement a web-based user interface. The code is translated from Python language to Java script and HTML based. The input panel shown in figure 2.8 allows user to choose calculation modes and assign important parameters for each mode as same as the Python based version. Then the results from each mode are displayed in the output panel.

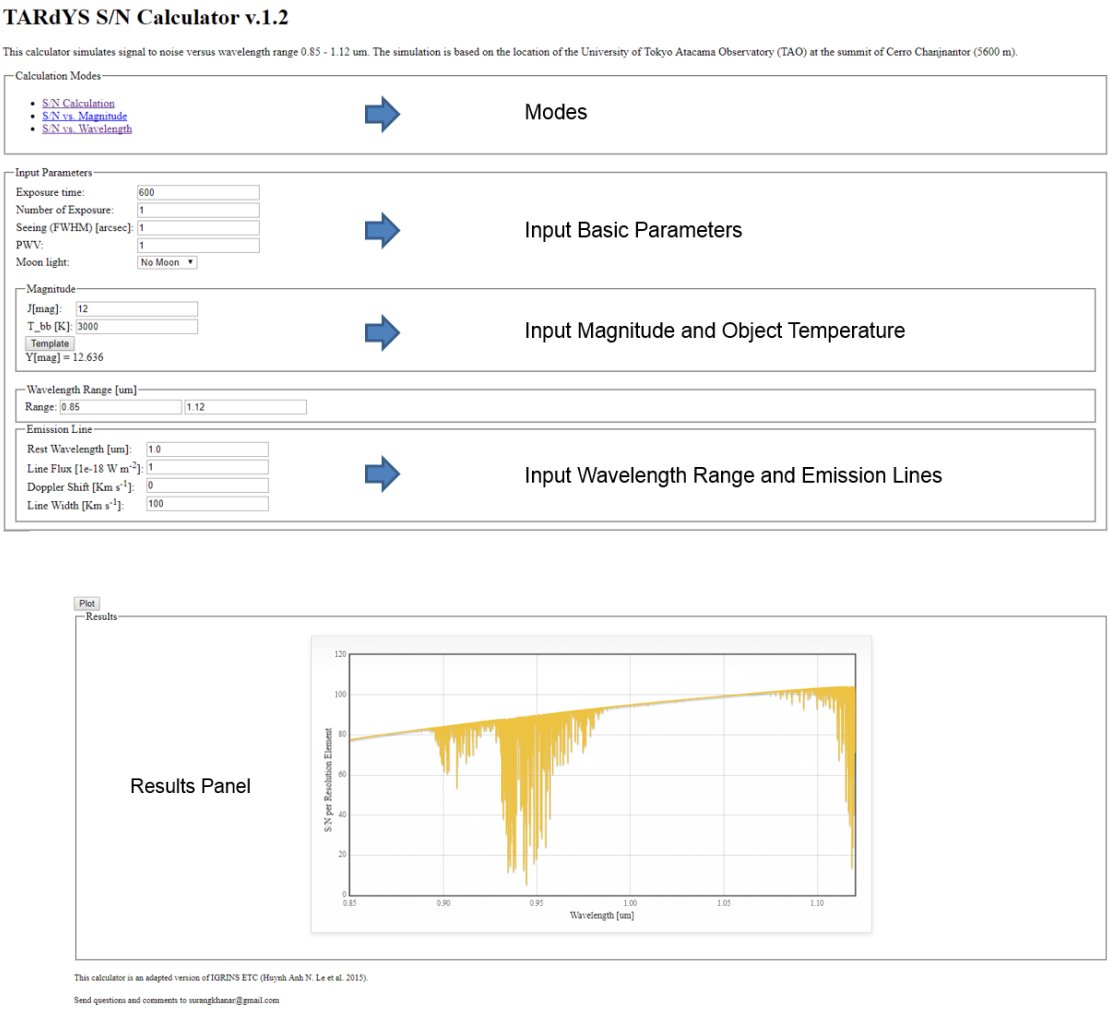

Figure 2.8. The web-based Graphical User Interface for TARdYS S/N calculator shows the input panels for assigning the calculation mode and the observing condition. The output panel shows the result from S/N vs. wavelength mode.

2.2.3. Application

This calculation method is also robust enough to be adjusted in order to work on different wavelength range. I modify some parameters to accommodate the average observing conditions of a optical spectrograph. I found that the simulation matches well with the real observational data as shown in Fig.2.9 (cite Vanzi+2018).

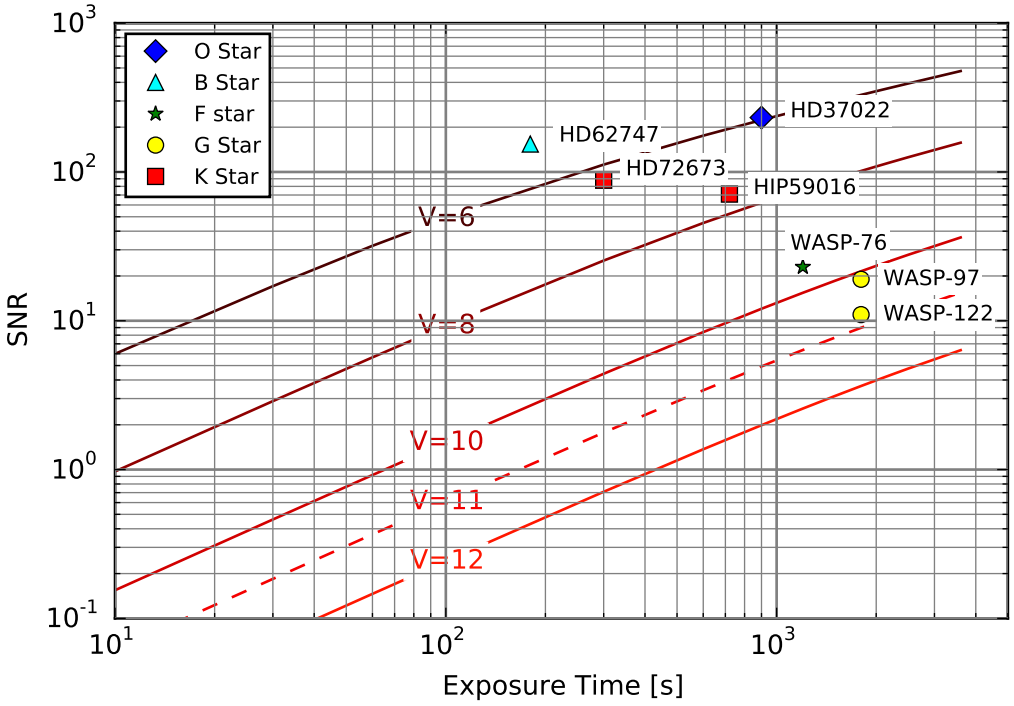

Figure 2.9. The limiting magnitude calculation of FIDEOS spectrograph using exposure time calculator with average observing condition during 30 minutes, overlayed with the real observational data point.

3. SPECTROGRAPH OPTICAL DESIGN

This chapter will focus on the optical design study and performance simulation of an upcoming near infrared high resolution spectrograph to be used as an exoplanet hunter. I explore the use of a recent commercially available Echelle R6 grating with various spectrograph main optics options in section 2 and 3. I will discuss the cost-effective solution from the optical design point of view. I perform some important analysis of the optical design to predict the performance of the spectrograph in section 4.

3.1. Aberration

In order to obtain a good optical system, designer should learn about the defects or so called aberration that cause the imperfection in the image formation of the optical system. There are two different systems used to describe wavefront aberration: Seidel aberration and Zernike polynomial.

3.1.1. Seidel aberrations

Seidel aberrations, from Ludwig von Seidel (1857) are basic types of aberration due to the geometry of optics. Seidel aberrations cannot describe all possible aberrations of the wavefront. The seidel aberration equations generally apply to a rotational symmetrical optical system, like spherical lenses. It is also known as third order aberration, which is typical to display system aberration using Seidel diagram (Fig.3.1). The Seidel equations have "field-dependent" terms for off-axis viewing angles.

Seidel aberration is a wavefront distribution function (W), where the exit pupil is calculated in terms of polar coordinates such that $x = \rho\cos\theta$ and $y = \rho\sin\theta$ (Wyant & Creath, 1992). The wavefront coefficient W_{jmn} can be described as:

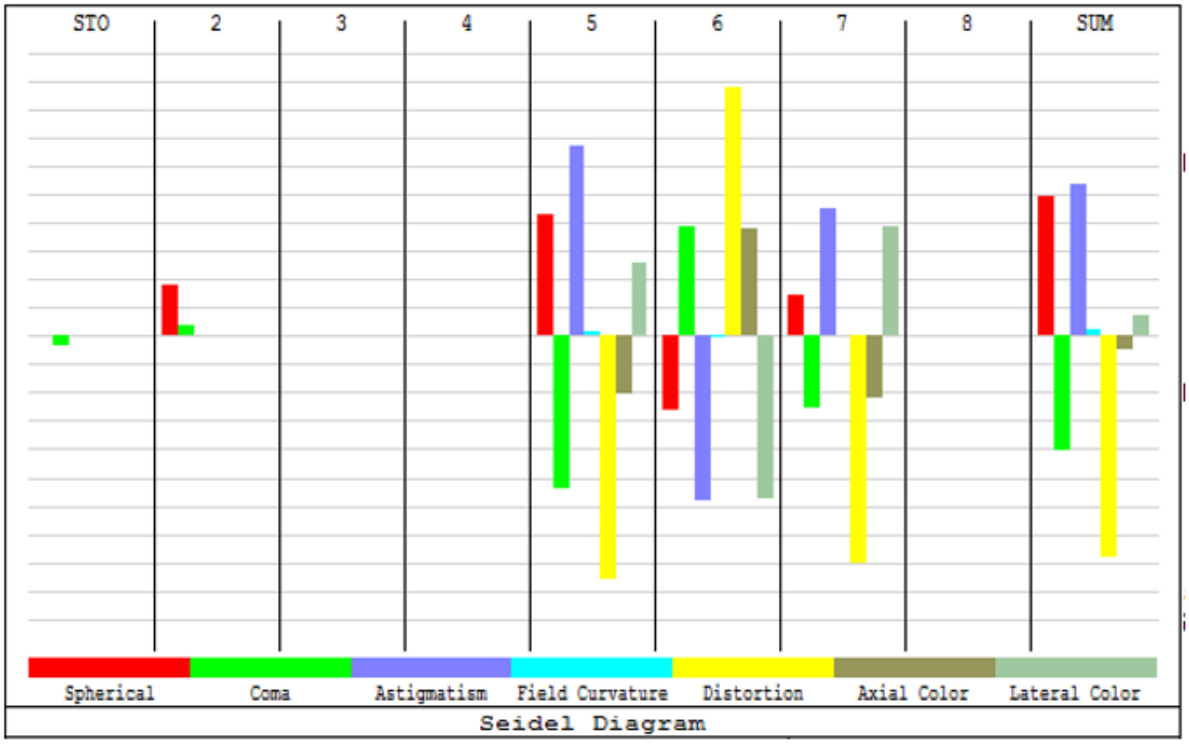

Figure 3.1. An example of Seidel diagram in ZEMAX. Each color block represents different type of third order (Seidel) aberration for each surface, which is shown independently in each column, in the system. The last column is the summation of the aberration of the system.

$$
\begin{aligned}
W(x_0,\rho,\theta) &= \sum_{j,m,n} x_0^k \rho l \cos^m\theta, \quad with\, k = 2j+m, l = 2n+m, \\
&= W_{200}x_0^2 + W_{111}x_0\rho\cos\theta + W_{020}\rho^2 \\
&+ W_{040}\rho^4 + W_{131}x_0\rho^3\cos\theta + W_{222}x_0^2\rho^2\cos^2\theta \\
&+ W_{220}x_0^2\rho^2 + W_{311}x_0^3\rho\cos\theta;
\end{aligned}
\tag{3.1}
$$

In terms of Seidel aberration coefficients S:

$$W(x_0,\rho,\theta) = \frac{1}{8}S_I\rho^4 + \frac{1}{2}S_{II}x_0\rho^3\cos\theta + \frac{1}{2}S_{III}x_0^2\rho^2\cos^2\theta + \frac{1}{4}(S_{III}+S_{IV})x_0^2\rho^2 + \frac{1}{2}S_V x_0^3\rho\cos\theta \tag{3.2}$$

where x_0 is image height. The relationship of the two aberration coefficients is shown in Table.3.1 (Shannon & Wyant, 1992).

Table 3.1. Relationship between wavefront aberration coefficients and seidel aberration coefficients.

Name	Wavefront Coefficient	Seidel Coefficient	Function
piston	W_{200}		x_0^2
tilt	W_{111}		$x_0\rho\cos\theta$
focus	W_{020}		ρ^2
spherical	W_{040}	$\frac{1}{8}S_I$	ρ^4
coma	W_{131}	$\frac{1}{2}S_{II}$	$x_0\rho^3\cos\theta$
astigmatism	W_{222}	$\frac{1}{2}S_{III}$	$x_0^2\rho^2\cos^2\theta$
field curvature	W_{220}	$\frac{1}{4}(S_{III}+S_{IV})$	$x_0^2\rho^2$
distortion	W_{311}	$\frac{1}{2}SV)$	$x_0^3\rho\cos\theta$

Monochromatic Aberration

Spherical Aberration (on-axis aberration): an optical defect that happens when the incoming light rays pass through a spherical surface, either mirror or lens. This is because the rays, striking the edge and center of the spherical surface, and reach a focus at different points along the optical axis. As a result, this causes blurry images.

Coma (off-axis aberration): Comatic aberration creates a comet-like blurry trail directed away from the optic axis. This is due to the different refraction when the rays pass through various zones of the optical surface. Coma is very similar to spherical aberration, but mainly encountered with off-axis light. It occurs often when the system is mis-aligned.

Astigmatism (off-axis aberration): this type of aberration has two focus points on each of the two perpendicular planes (tangential and sagittal). The image will appear elliptical in shape and off-axis. This is a monochromatic aberration (occurs even with a single wavelength).

Field Curvature (off-axis aberration): Petzval field curvature happens when image plane deviates from a flat surface or flat object, located normal to the optical axis, cannot bring the focus onto a flat image plane. Thus, the image is not uniformly sharp across the frame. The effect can be reduced by using a field stop, a limitation of which points on the object can produce an image, to remove the edge light ray.

Distortion (off-axis aberration): is a quadratic magnification error that alters the original shape on the image. The positive distortion, where the predicted distance of a pattern such as a dot target is more than an actual distance, is called Barrel distortion. This occurs when the image magnification decreases with the distance from the optical axis. The negative distortion from the increasing magnification is called Pincushion distortion. The mixture of both types is Moustache distortion.

Chromatic Aberration Chromatic aberration occurs when a lens is unable to bring all of the working wavelengths to the same focal plane. This can occur both in the longitudinal (axial) and lateral (transverse) direction. Chromatic aberration can be reduced by using an achromatic lens, which consists of materials with different refractive index, a dispersive property, to bring those wavelengths together.

3.1.2. Zernike polynomials

Zernike polynomials, named after Frits Zernike, are used to decompose complex wavefront into a polynomial functions in different modes. They are more common in vision science for describing wavefront aberrations. The Zernike aberration equations, apply to asymmetrical optical systems and have no field-dependent terms. The Zernike aberrations are calculated at a specific angle of view, while many Seidel aberration equations include a term that varies

with the angle of view. Zernike is preferred for the higher order aberration calculation. Some examples of the surface aberrations calculated[2] using zernike polynomials for the first, second and third orders are shown in Fig.3.2.

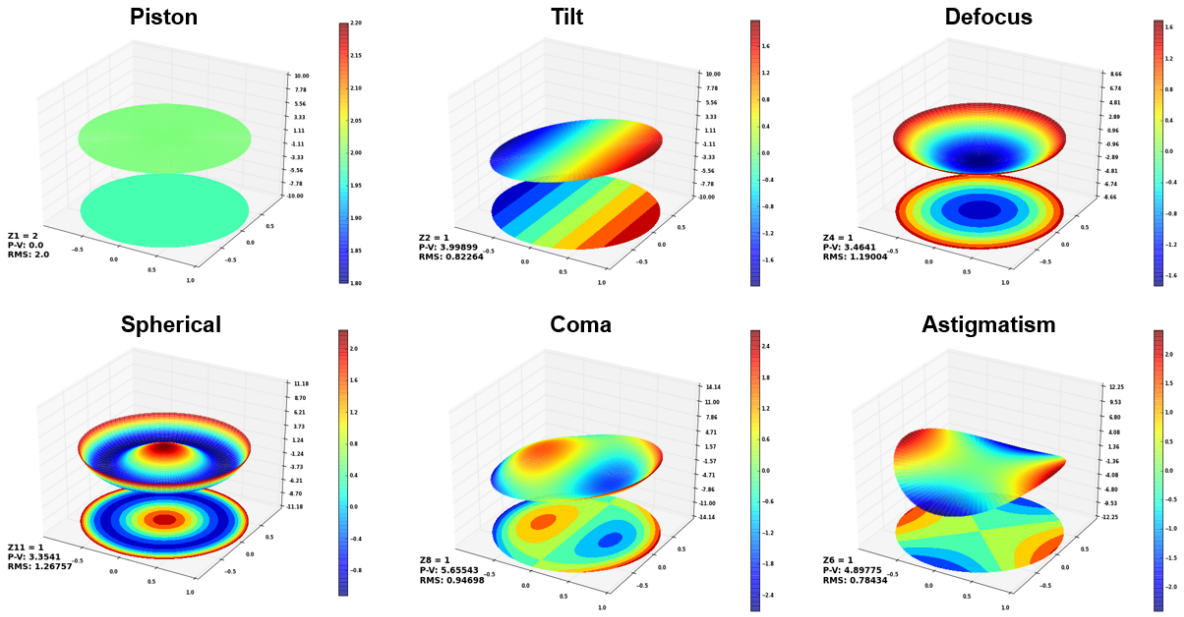

Figure 3.2. Zernike surfaces of the first, second and third order. From left to right, *top row*: piston, tilt, defocus, *bottom row* spherical, coma, astigmatism.

For the optical design, I use ZEMAX as a simulation tool. ZEMAX is ray tracing program, which models the propagation of rays through an optical system. It can model the effect of optical elements including the aberration from their properties such as gradient index lenses, mirrors, and diffractive optical elements. I can retrieve standard analysis diagrams such as layout, spot diagrams, and point spread function (PSF). ZEMAX can also model the effect of optical coatings on the surfaces of components. It includes a library of an up-to-date stock commercial lenses and also allows users to model their own glass catalog.

[2]http://sterncat.github.io

3.2. System Consideration

The science driver for this spectrograph is the search for planets around cool and low mass stars type M. Due to their large numbers, M dwarfs are interesting candidates for planets in their habitable zone, a distance from a star where water stays liquid (Tarter et al., 2007). Planet formation theories can be tested by M dwarf planet searches (Ida & Lin, 2004).

Infrared (IR) spectroscopy is highly efficient to observe M type stars, since the flux emitted by M5 dwarfs at 1 μm (Y-band) is a about 3.5 times higher than in the optical regime (0.6 μm). To achieve RV precision of 2.2 m/s in Y-band spectroscopy, assuming signal to noise (S/N) of 100 at 1 μm, requires spectral resolution R=60,000 for spectral-type M9 (Reiners et al., 2010).

The optical design considerations for the near infrared spectrograph are similar to the ones working in the visible wavelength range except for the optical material, cost and IR detector. High thermal backgrounds are major issue for designing near infrared spectrographs. As a result, these spectrographs are normally cooled in a cryogenic system.

The spectrograph is designed according to the science requirements and budget constraint of not having an IR detector array larger than 1,024 x 1,024 pixels size. We plan to employ a 1k infrared detector. Applying minimum spectral sampling of 2 pixels, the spectral resolution element is given by:

$$\Delta\lambda = \frac{FSR}{\frac{numberofpixels}{2}}, \tag{3.3}$$

With the free spectral range (FSR),

$$FSR = \frac{\lambda}{m}, \tag{3.4}$$

And the spectral resolution,

$$R = \frac{\lambda}{\Delta\lambda} = \frac{m * numberofpixels}{2}. \tag{3.5}$$

And grating equation in Littrow configuration,

$$m\lambda = 2d \sin \theta_B. \tag{3.6}$$

where m is the spectral order, d is spacing between grooves, θ_B is grating blazed angle. The working wavelength (λ) is set to 1 μm. To reach R $\geq$ 50,000 with a 1k detector, working at order m $>$ 100 is necessary. This leads to the main disperser choice of a commercially available echelle R6 grating with 13.33 grooves/mm giving θ_B = 80.6 $^\circ$, which disperses all the Y-band within the detector limited space. The choice of the H1RG detector and R6 grating set the effective focal length (EFL) of the objective to 200 mm and give Nyquist sampling of 2 pixels.

3.3. Optical Design Comparison

In recent years, a number of exoplanet instruments(Pepe, Ehrenreich, & Meyer, 2014) started operation in the near infrared region, such as GIANO (Oliva et al., 2006); they report many interesting science results including Chemical abundances of Phosphorus, Sulfur and Strontium essential for galaxy evolution study (Caffau et al., 2016), High precision near infrared radial velocity information (Bean et al., 2010) and Detection of Neptune sized planet around M4.5 dwarf (Mann et al., 2016). Further large coming up instruments are HPF (Mahadevan et al., 2014), IRD (Tamura et al., 2012), CARMENES (Quirrenbach et al., 2014), and SPIRou (Artigau et al., 2014), all optimized for an RV measurements. In the table 3.2, I compare some important design parameter for these recent spectrographs.

To compare with existing infrared spectrographs, TARdYS is a unique project to test a number of not completely common solutions such as a use of the R6 grating, the image slicer in the near infrared region, only a semi-cryogenics setup, and working at a very high altitude (5,640 m) environment at Tokyo Atacama Observatory (TAO), the highest observatory site in the world.(Yoshii et al., 2010).

Table 3.2. Design comparison of existing near infrared spectrographs

Instrument	λ [μm]	R	Telescope	Beam size	Input	Main Disperser
GIANO	0.90-2.50	46,000	TNG 3.5m	100mm	Fiber	Echelle R2
CARMENES	0.90-1.75	80,000	Calar Alto 3.5m	153.3mm	Fiber-IS*	Echelle R4
IRD	0.97-1.75	70,000	Subaru 8m	n/a	Fiber	Echelle R6
HPF	0.85-1.70	60,000	HET 10m	150mm	Fiber-IS	Echelle R4
SPIRou	0.90-2.40	85,000	CFHT 3.6m	150mm	Fiber	Echelle R4
TARdYS	**0.84-1.12**	**66,000**	**TAO 6.5m**	**3**0mm	**Fiber-IS**	**Echelle R6**

All spectrograph are using White Pupil Configuration
*Fiber-IS = Fiber and image-slicer

3.3.1. Slit vs Fiber

From the science case of detecting M dwarfs, one needs a spectral resolution of R$\approx$ 60,000. We need to consider resolution and pixel sampling. According to equation 3, if we need the resolution $R = 60,000$ then the wavelength resolution is $\Delta\lambda = 1\mu m/60,000 = 1.6x10^{-5}\mu m$ per 2 pixels; i.e. $8.3x10^{-6}\mu m/pixel$. If we consider the precision of 5 m/s case, we have $R^{-1} = \Delta\lambda/\lambda = \Delta v/c$. Assumed that the spectral shift $\Delta\lambda = (5m/s)/(3x10^{8}m/s)x1\mu$m $\approx 1.6x10^{-8}\mu m$. As a result, within one pixel $\Delta pix \equiv (1.6x10^{-8})/(8.3x10^{-6}) \approx 1/500$. In the end, the spectrograph has to resolve $18\mu m/500 = 36nm$. Thus, the fiber is used at the spectrograph entrance pupil.

The spectrograph entrance pupil concept is adopted from the FIbre Dual Echelle Optical Spectrograph (FIDEOS) at AIUC (Tala et al., 2014). The light from dual fibers (50 μm diameter, f/4), which correspond to 0.4 arc second diameter on the sky, are fed through a simplified version of the Bowen-Walraven image slicer. Given a suitable distance and angle of its two mirrors, the image slicer creates a two-slice image of a circular fiber containing an astronomical object image. The image slicer (Tala et al., 2017) works to increase the resolution of the spectrograph. The two mirror configuration of image slicer also yields the high efficiency of more than 90 $\%$ throughput (Gerardo Avila, 2012).

3.3.2. Collimator

A reflective parabolic surface collimates the beam from slit onto the dispersive element. After the image slicer, I assign the entrance pupil diameter in ZEMAX to be 28 mm. The light goes directly to the 156 mm diameter sized parabolic collimator with focal length 550 mm. I use an off axis angle of 3.8 degrees to use a subaperture of the main mirror as off-axis ZERODUR parabola with gold coating to achieve the highest reflection efficiency within the spectrograph's working wavelength (0.843-1.117 μm).

If one examines the spectrograph in Littrow configuration using a slit limit, the spectral resolution of telescope and instrument configuration can be specified in the term of Resolving Power (R), which is defined as:

$$R = \frac{2f_{col}\tan\theta}{\delta f} \tag{3.7}$$

where f_{col} is the focal length of collimator, δf is the slit size. In case of using an image slicer to slice a fiber of the size 50 μm, this eventually forms a pseudo slit at the spectrograph entrance pupil. I apply f_{col} = 550 mm. The $\tan\theta$ is 6. Thus the spectrograph will have R= 66,000.

3.3.2.1. Conic Constant

The shape of the mirror is usually described using conic constant. It explains a conic section (κ) where $\kappa = -e^2$ while e represents the eccentricity of the conic section. A conic section with apex at the origin and tangent to the y axis can be expressed as

$$y^2 - 2Rx + (\kappa + 1)x^2 = 0 \tag{3.8}$$

where κ is the conic constant and R is the radius of curvature at x = 0. In terms of the spectrograph design, conic constant of the collimating mirror plays a significant role in the image quality. Here I provide examples of using collimator with different conic constants in a spectrograph design that yields different image quality. The system has the same collimator focal length of 550 mm and I define a camera focal length of 200 mm using a paraxial surface.

The following illustrations show the Huygens Point Spread Function (PSF) on left hand side and the spot matrix at the central wavelength of the working wavelength range on the right hand side.

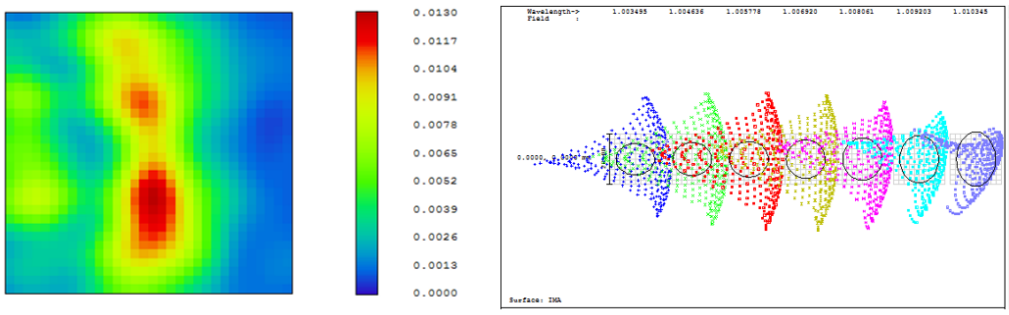

Figure 3.3. κ = 1. (Left) the Huygen PSF yields Strehl ratio of maximum 0.013 in the red region. (Right) spot metrix of wavelength 1.00-1.01 μm.

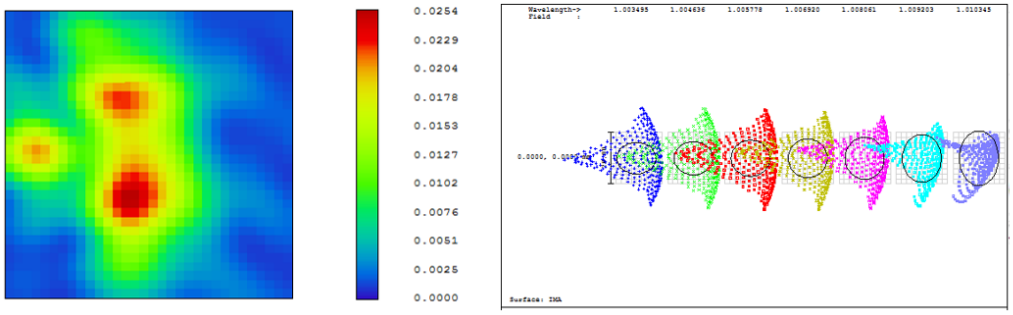

Figure 3.4. κ = 0.5 representing an elliptical shape mirror. (Left) the Huygen PSF yields Strehl ratio of maximum 0.028 in the red region. (Right) spot metrix of wavelength 1.00-1.01 μm.

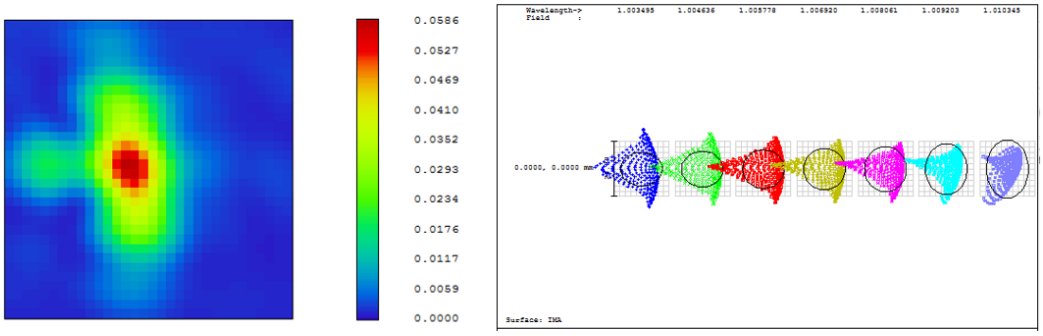

Figure 3.5. $\kappa = 0$ representing a spherical shape mirror. (Left) the Huygen PSF yields Strehl ratio of maximum 0.0586 in the red region. (Right) spot metrix of wavelength 1.00-1.01 μm.

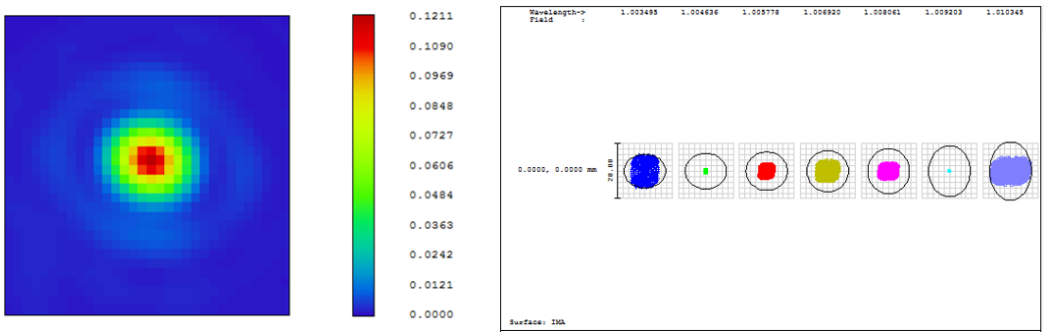

Figure 3.6. κ = -1 representing a parabolic shape mirror. (Left) the Huygen PSF yields Strehl ratio of maximum 0.1211 in the red region. (Right) spot metrix of wavelength 1.00-1.01 μm, diffraction limited.

3.3.3. Coating

Optical coating is a thin layer of material deposited on the optical components to enhance transmission or reflection. A spectrograph consists of many surfaces in the system. We apply both anti-reflection (AR) coating and metal coating on the collimating mirror since we want to collect as many photons as possible. Different types of coating yield different reflectivity at different wavelength as shown in Fig.1.6 (Weber, 2002).

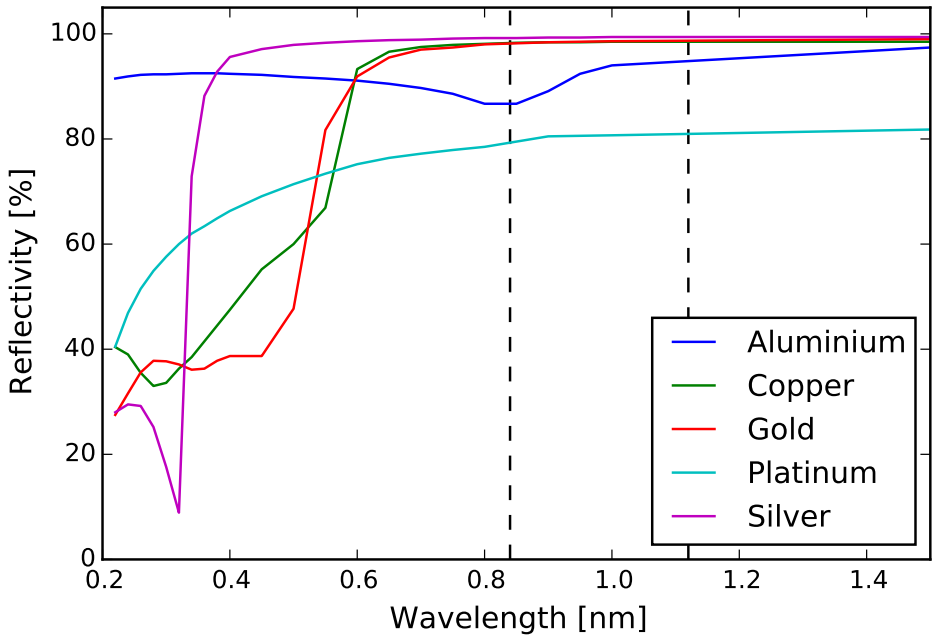

Figure 3.7. Reflectivity of different coating materials at different wavelength. TARdYS working wavelength is between the two dash line. The gold coating (red) is applied for the main collimating mirror. (data from Handbook of Optical Materials (Weber, 2002))

3.3.4. Setup Configuration

The design study considers two different configurations: quasi-Littrow and White Pupil.

3.3.4.1. Quasi-Littrow Configuration

In the concept design of TARdYS, I started with a quasi-Littrow (QL) spectrograph design (Berdja, Vanzi, Jordán, & Koshida, 2012). As shown in Fig. 3.8, the light beam reflects on a collimating mirror, an Echelle grating, a VPH grating and finally the camera optics respectively. With this configuration, I found that the predicted performance of the spectrograph from ray-tracing suffers from anamorphism. The focal plane image is always tilted due to the setup of the spectrograph as shown in Fig. 3.8 due to an angle γ (Schroeder, 1967) at the Echelle grating mount to direct the dispersed light towards the cross disperser.

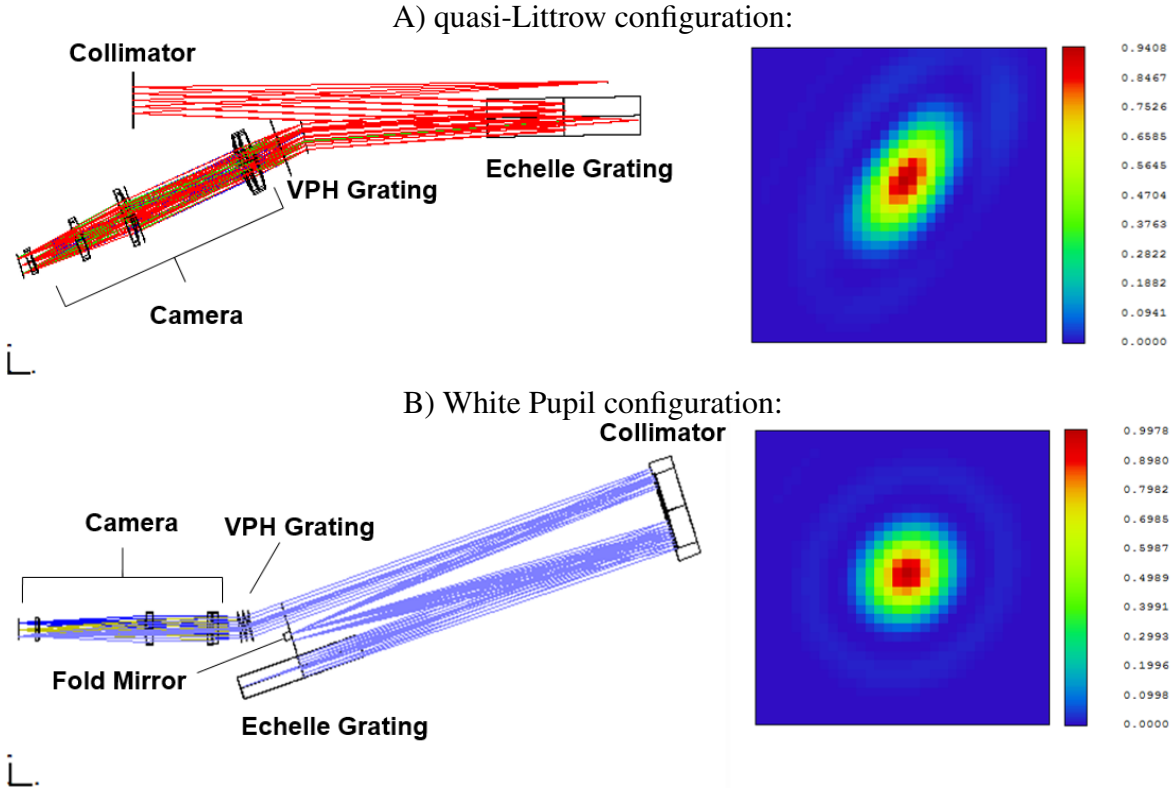

Figure 3.8. Optical layout of quasi-Littrow configuration (top left panel) and White Pupil configuration (bottom panel). The corresponding plots of the point spread function (PSF) on the right shows a symmetric behaviour, due to the White Pupil configuration, on the image plane. The Strehl ratio calculated at central wavelength or $\approx 1\mu$m of this configuration reach 0.99 in the red region.

3.3.4.2. White Pupil Configuration

I apply Baranne's classic White Pupil (WP) configuration (Baranne, 1972) and a parabolic mirror (conic constant K = -1) as a collimator in Fig. 3.8. Gratton's analytic calculations of Third-Order aberration (Gratton, Bhatia, & Cavazza, 2000) demonstrate that the WP configuration can cancel spherical aberration, coma, astigmatism, distortion and chromatic aberrations. The White Pupil configuration re-images a pupil placed on a grating into a secondary pupil where a cross disperser or camera optics can be placed. It is called 'white' because the pupil image location is independent of wavelength even though the light is dispersed (Bershady, 2009). It minimizes the geometrical aberrations that occur in QL configurations. The design delivers better image quality than the QL design for the same resolution. In the

right panels of Fig. 3.8, I evaluate the point spread function (PSF) to compare the image quality of the different design options. Both yield a similar value of Strehl ratio in central field shown in red in Fig. 3.8 at approximately 1.0 μm. However, the QL configuration shows asymmetrical and tilted PSF behavior. In contrast, the WP PSF is circular.

3.3.5. Dispersers

The main dispersive element is a R6 Echelle grating. Echelle gratings are blazed to high angles to yield high orders but this causes order overlapping that must be separated by cross-dispersion. The R values correspond to the tangent of a grating's blazed angle. The difference of these angles also has an effect on the size and volume of the spectrograph; smaller R value corresponds to larger spectrographs. In order to have a compact spectrograph, I choose a R6 Echelle grating, which gives the largest blazed angle of 80.5 degrees commercially available to date. It is the only fixed component in the design. The echellogram shown in Fig. 3.9 is calculated based on a diffraction equation from Schroeder (Schroeder, 1967). I apply f_{col} = 550 mm. Ultimately, the spectrograph targets R $\approx$ 66,000.

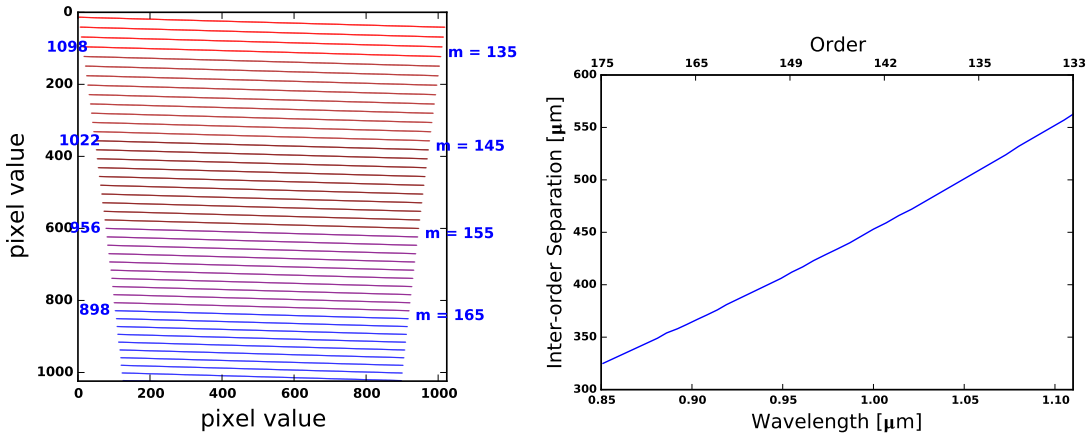

Figure 3.9. The echellogram in the left panel shows the free spectral range of 42 orders on the detector of 1,024x1,024 pixels. The right panel shows inter-order separation using VPH grating with 333 lines/mm as cross-disperser.

I choose a Volume Phase Holographic (VPH) Transmission Grating from Kaiser Optical System, Inc. as a cross disperser to obtain high efficiency. To optimize the inter-order separation, I modelled the dispersion in ZEMAX and tested various options of VPH line spacing. The separation increases with wavelength to the redder region. This is shown in the right panel of Fig. 3.9. I decided to use a VPH grating with 333 lines/mm at a 9.3° incidence angle, which is ideal because the two gratings will disperse the incoming light over a 0.843-1.117 μm wavelength range with a total of 42 orders (133 to 175) on a 1k detector. I simulate the detector plan according to the parameters mentioned above. The echellogram on the detector is shown in the top left panel of Fig.3.9.

3.3.6. Camera

The goal for optimizing the camera is to have the least number of surfaces in order to minimize losses. I design the camera of TARdYS for room-temperature assembly to minimize costs. Nevertheless, to achieve low noise, the detector and the last lens are placed in a cryogenic Dewar cooled to 80K (at the time of writing the thesis). The purpose of having this semi-cryogenic setup is to study the temperature effect of a Y band spectrograph later.

A doublet lens is chosen at the beginning of the camera to correct for chromatic aberration. The design of the camera started with 5 lenses: a doublet and 3 singlets. The choice of doublet is a simple combination of N-BAK4 and N-SF10. The singlets are BK7 glass, which has a relatively low cost. I show the camera lenses in the top panel of Fig. 3.10. I optimized the camera to obtain small spot sizes within the diffraction limit. The bottom panel in Fig. 3.10 shows the spot matrix for the lowest, middle and highest orders. Generally, the spot sizes increase from left to right, where it exceeds the diffraction limit of the airy disk (black circle). In addition, the spot sizes shown in Fig. 3.10 increases rapidly at one side of the detector and appear to be defocused at the upper right corner.

The camera design is evolved from this point by first changing the doublet combination. A crown glass and a flint glass were selected by the hammer optimization tool in ZEMAX considering the transmission wavelength and relative cost. Then the number of singlets is

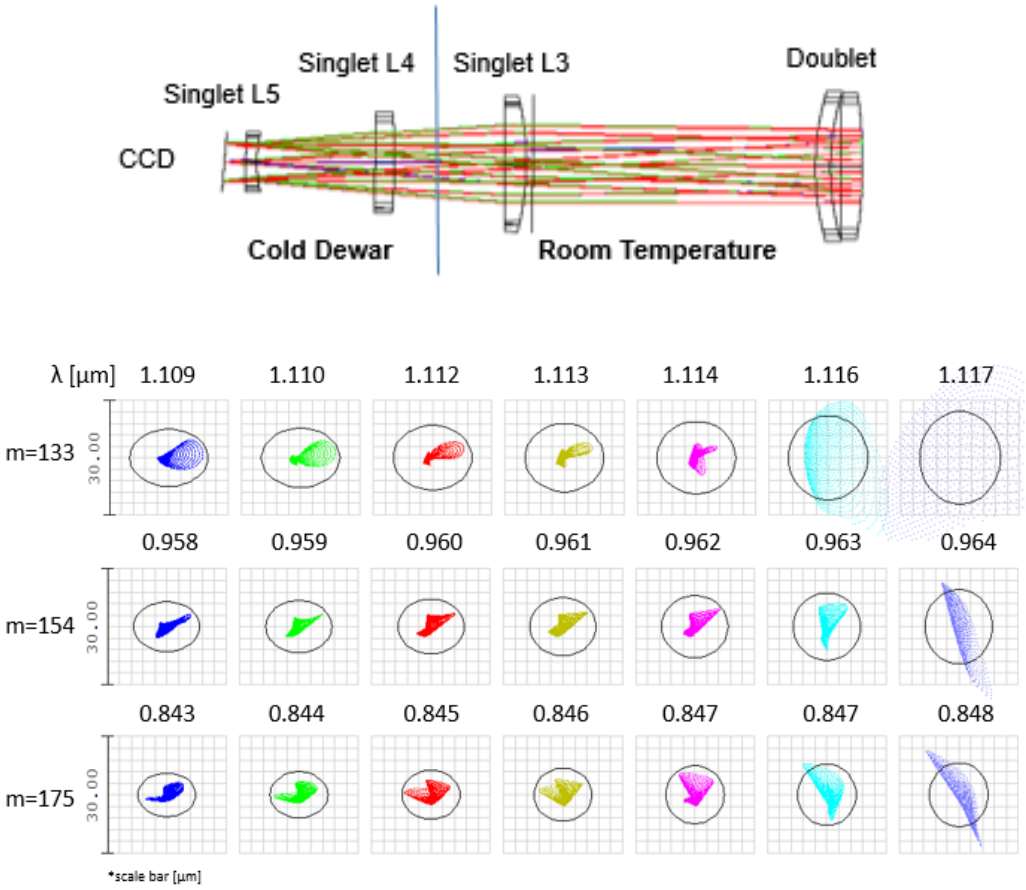

Figure 3.10. Top panel: the camera design with 5 lenses. The spot diagrams in the lower panel show the rays traced across the focal plane on the image surface from the 5 lenses camera. The three rows present the reddest, central and bluest orders. Columns present increasing wavelength within each order (m).

decreased by carefully optimizing the ZEMAX merit function and flattening one middle lens until it could be removed.

The final design is depicted in Fig. 3.11. I select one doublet of N-SK2 and N-SF6. The two singlets (L3 and L4) are fused-silica lenses. These are less affected by thermal expansion because we plan to cool this part of the camera. In the end, the camera has a focal length of 200 mm and consists of four 50 mm diameter lenses. At the time of writing the thesis, only the last lens will be in the cryogenic Dewar. Spot diagrams of rays traced across the

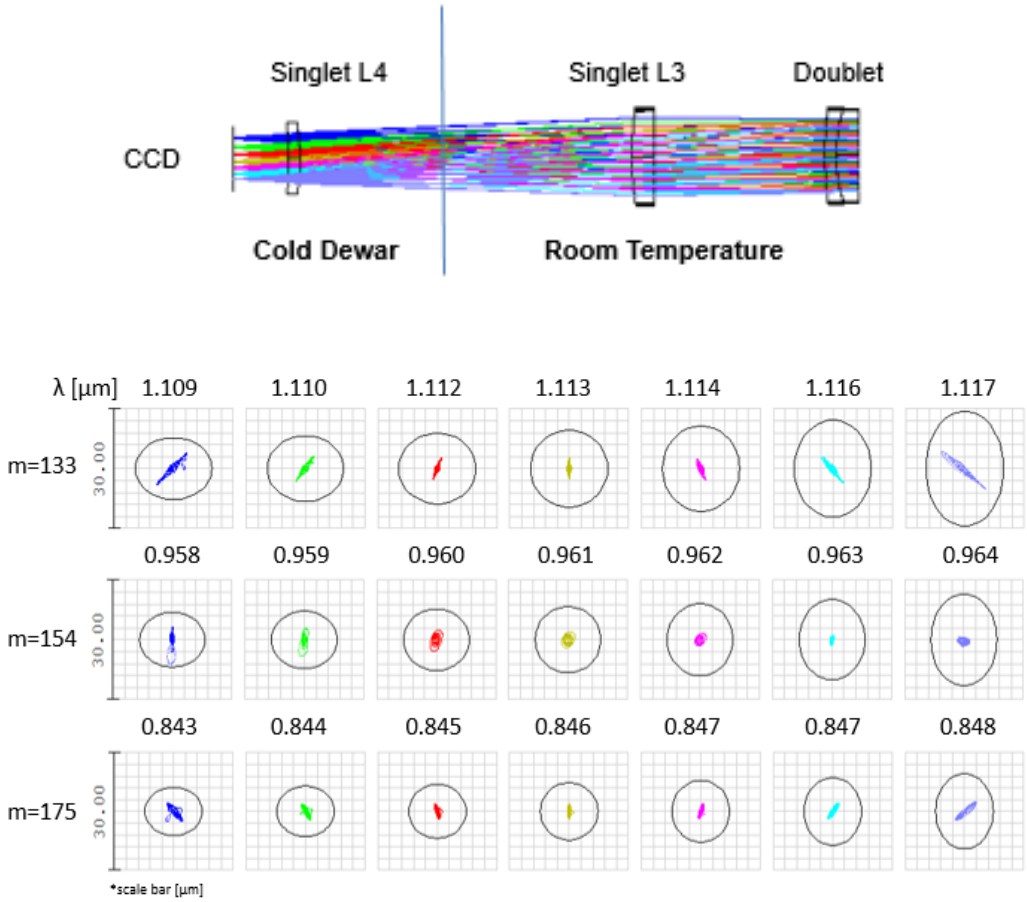

Figure 3.11. Final camera design with 4 lenses. The last (left) part of this camera, the detector and the last singlet L4, will be cooled in cryogenic Dewar. Spot diagrams below show the rays traced across the focal plane on the image surface, as in Fig.3.10. In all cases, the spots are smaller than the diffraction limit (black circles). The three rows present the reddest, central and bluest orders. Columns present increasing wavelength within each order.

focal plane on the image surface. In Fig. 3.11, the RMS spot size is clearly smaller than the 5 lenses configuration in Fig. 3.10. It is also diffraction limited everywhere in the ambient environment.

3.3.7. Comparison

The performances are compared for all four combinations: the two spectrograph configurations, quasi-Littrow (QL) and White Pupil (WP), with the two camera configurations, four lenses and five lenses. The Strehl ratio is demonstrated in Fig. 3.12. This is a comparison of the combinations through the entire Y-band working wavelength. The quasi-Littrow configuration exceeds $> 80\%$ with either camera. However, it performs better with the 5 lenses combination. The White Pupil design shows a more symmetrical behaviour throughout the working wavelength range. It yields $> 90\%$ with both camera designs, with the 4-lens camera performing best. Thus, I choose the White Pupil configuration with the 4-lens camera as the final design.

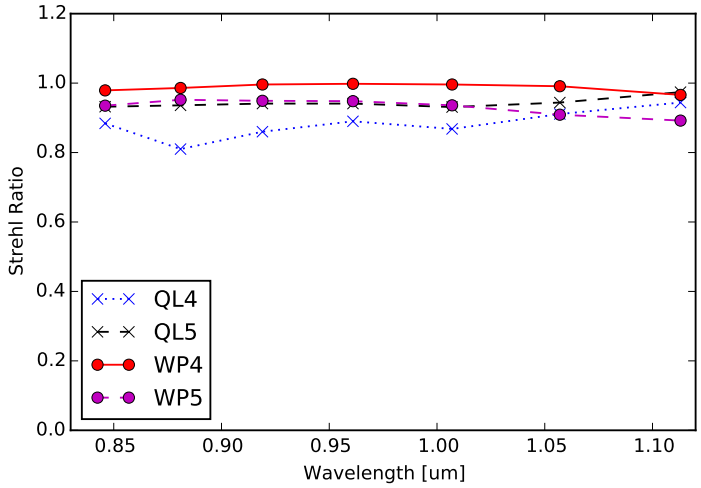

Figure 3.12. Strehl ratio of four configurations: quasi-Littrow (QL) or White-pupil (WP) with 4 or 5-lens cameras. The White-pupil configuration with 4-lens camera (red line) yields the highest ratio throughout the working wavelength range.

3.4. Analysis

This section aims to analyse the robustness of the design to manufacturing and alignment defects (§3.1), thermal changes (§3.2).

3.4.1. Tolerance Analysis

The tolerance analysis focuses on the camera part of the spectrometer. This is a critical part of the system because the camera must be cooled down to 80K in a cryogenic Dewar. One can reduce fabrication cost and delivery time by performing a testplate fit to all of the lenses. The testplate fit did not change the optical performance significantly, which is also presented in the previous section.

In the tolerance analysis, I forced ray aiming in ZEMAX for reliable results. For the alignment tolerances, the doublet was treated as a group. Additionally, I allowed the lenses to pivot about the center of curvature of the mating surface, to account for tolerances during cementing. The summary of the general tolerance variation is shown in Table 3.3.

The test wavelength of the analysis is at 1 μm. I use detector tilt and focus as compensators, and optimize the design using Damped Least Squares. In a Monte Carlo procedure, ZEMAX generates lens tolerances randomly from within the assigned range which is listed in Table. 3.3. The merit function (MF) measures the agreement between data and the fitting model for a particular choice of the parameters. By convention, the merit function is small when the agreement is good. However the output number of MF in the result mostly depend on the initial parameters boundary. The distribution of merit function values for 200 trials is shown in Fig 3.13. As an example for a typical as-built system, I choose the design that lies at the mean of this distribution.

Table 3.3. Camera Tolerance Criteria: parameters ranges to Monte Carlo generate 200 different designs. The central wavelength is set at 1 μm.

Surface	Property	Value
Doublet	Surface radius	1 fringe
	Center thickness	$\pm$0.05 mm
	Wedge	$\pm$0.01 mm
	Irregularity	λ/8 mm
	Tilt	$\pm$0.2 mm
	Decenter	$\pm$0.2 mm
Group Spacing	Center thickness	$\pm$0.05 mm
Doublet	Surface radius	1 fringe
	Center thickness	$\pm$0.05 mm
	Wedge	$\pm$0.01 mm
	Irregularity	λ/8 mm
	Surface Tilt	$\pm$0.2 mm
	Surface Decenter	$\pm$0.05 mm
	Element Tilt	$\pm$0.2 mm
	Element Decenter	$\pm$0.2 mm

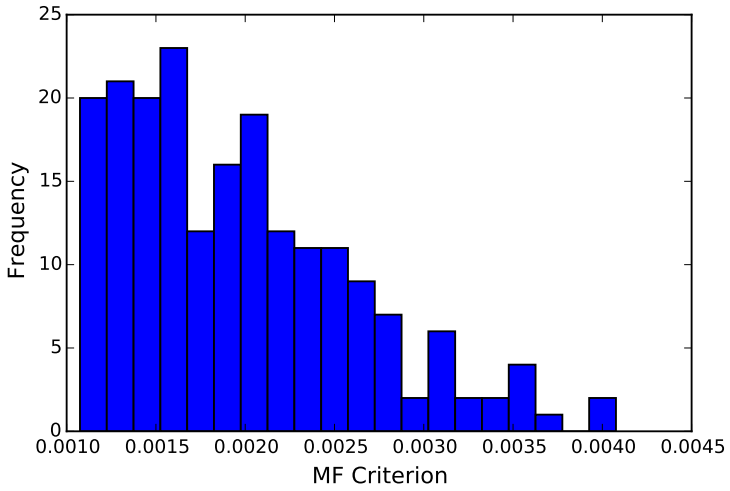

Figure 3.13. Histogram of the merit value of 200 Monte Carlo draws of design within the tolerance criteria from Table. 3.3.

3.4.2. Thermal Analysis

The system environment of TARdYS' original design was set at a temperature of 20°C and pressure 1 atm. As the last lens is cooled to cryogenic temperatures, I analyzed the optical performance for the singlet L4 at 73K (-200 °C). To obtain a reliable refractive index at cryogenic temperatures, I used the measurements of the Cryogenic, High-Accuracy Refraction Measuring System (CHARMS) (Leviton & Frey, 2008). They measured the absolute refractive index of fused silica from temperature ranging from 30 to 310 K at wavelength 0.4 to 2.6 μm with an absolute uncertainty of $\pm 1 \times 10^{-5}$. I construct a new glass catalog with the Sellmeier 1 formula via the ZEMAX glass fitting tool.

From the glass fitting, I retrieve the new glass properties of Fused Silica and assign it for thermal analysis at -200 °C. Initially the spot diagram had an airy disk size of 8.5 μm. The original setup shows a defocused spot diagram in the cold environment. The focusing problem can be solved by increasing the distance between the last Fused Silica lens and the detector mechanically. I optimized the thickness of the surface by using a merit function that considers all orders. The required detector tilt is 0.26 ° in the cross dispersion direction. For an optimally focused setup, the optics are diffraction limited over the whole field using spot rms criteria.

4. OPTOMECHANICAL DESIGN

Optomechanical mounts are crucial parts to hold optical components in place. The optical performance of a lens or a mirror can be significantly degraded by an inappropriate mounting configuration. A simple alignment can be perform by means of successful mounting components. TARdYS spectrograph has a very compact design comparing with other existing spectrographs. Although I have heritage design from the previous visible spectrograph built in AIUC, the space constraints of TARdYS introduce some difficulties to optomechanical mounts of this spectrograph.

To design any optomechanical mounts, I have to check the clear aperture or footprint of every single surface from the optical design. Then I determine the available space left for the mount. A general rule applied to these mount via six points kinematic scheme.

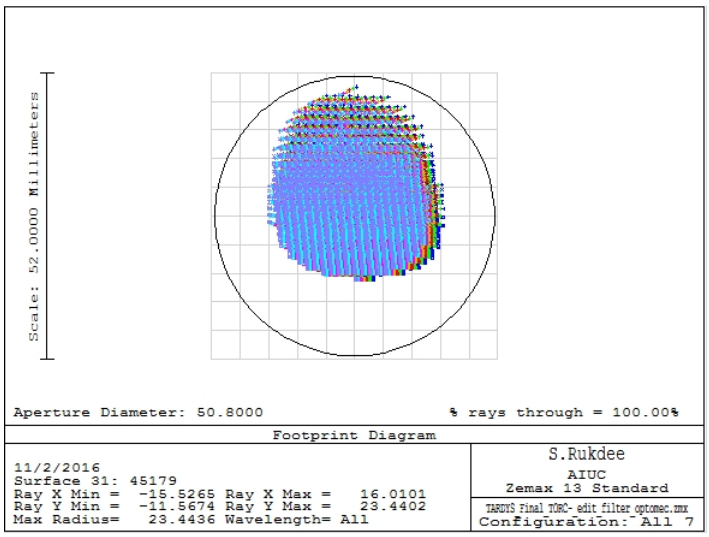

Figure 4.1. An example of a footprint diagram of Camera lens L1 retrieved from TARdYS optical design. The colored area is where the optical path is going through and the mount must not obstruct it.

4.1. Collimator Mount

The collimator mount housing structure is adjusted from (Tala et al., 2014). From Fig. 4.2 The mirror's outer ring is adapted from the circular fold mirror mount of (Rukdee et al., 2012). The back part contain three micrometric screws to allow tip-tilt adjustment. The mirror is made of Zerodur applying gold coating.

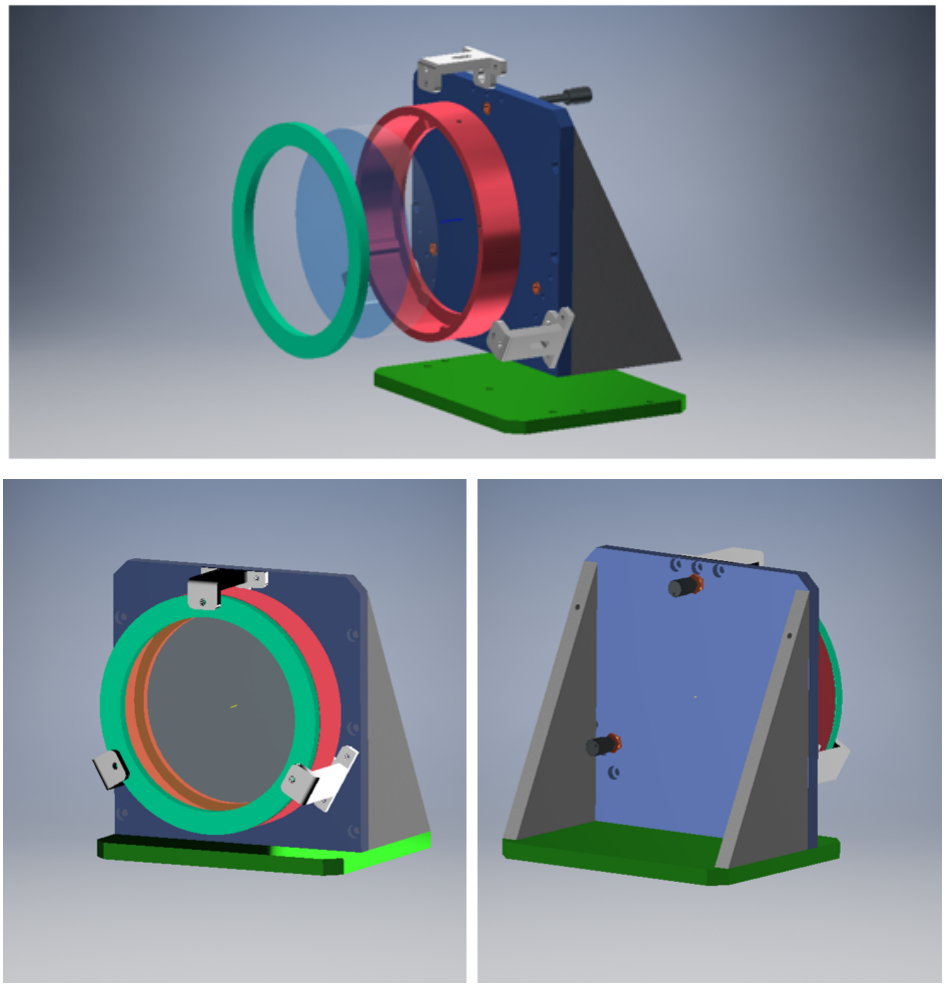

Figure 4.2. Top: The exploded view of the collimator mount showing all parts in the assembly. Lower Left: The front side of the collimator mount showing the ring structure (red) and cover (green) are being held with three clamps. Lower Right: The back side of the collimator housing structure showing micrometric screws (black screws) to be used for tip-tilt adjustment.

4.2. Echelle Grating

The Echelle grating is one of the most sensitive part of the system. The grating itself is faced down toward the optical table. The mount needs to allow enough degrees of freedom for alignment purpose. I apply a 'box' structure to hold the grating. This box also include the six points kinematic by introducing some hard points inside the box using end-hemisphere or small metal balls. This similar scheme is also applied in (Schwab et al., 2016) Part of FEM analysis of the echelle material is also presented in the same paper. In the design, I cut down part of the wall to avoid the collision with the input optics. The housing structure allows a few degrees tip-tilt to the grating box. The end hemisphere is used with the based plate (grey plate) to alignment as shown in Fig. 4.3.

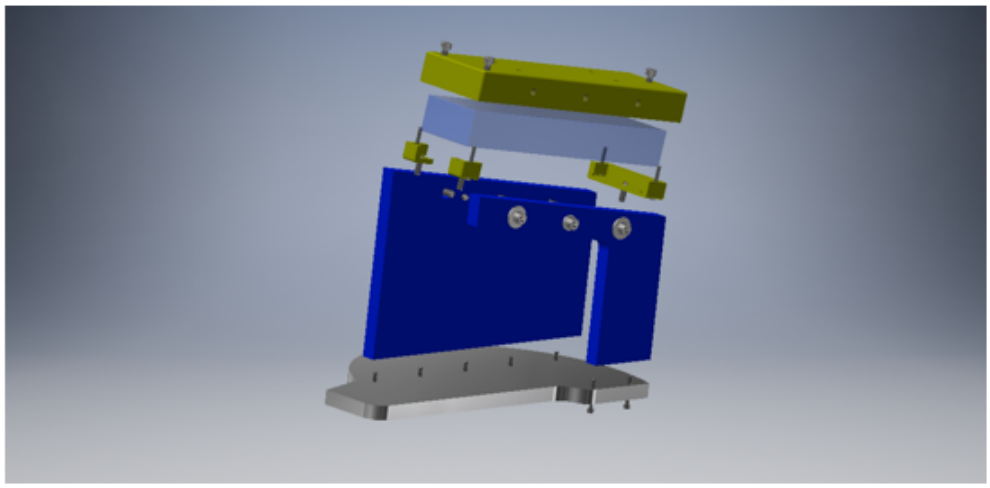

Figure 4.3. The Echelle box (yellow) is mounted with the housing structure (blue), which allowed the tip-tilt adjustment of the box. The grey based-plate allows the radial movement of the mount.

4.3. VPH Grating Mount

The VPH grating has a transmission property, thus the mount must not block the light going through this grating. The mount consists of 4 parts in Fig. 4.4: mount frame (red), spring frame(blue), mount holder, based plate. I design a squared mount frame of same size with the grating with three radial hard points using spring plunger and three axial hard points on inside the mount frame combine with some spring force pushing against the mount frame. The mount holder is designed so that the VPH grating has the same height as the optical path. The based plate is a circular shape plate that allow the rotation about the optical axis.

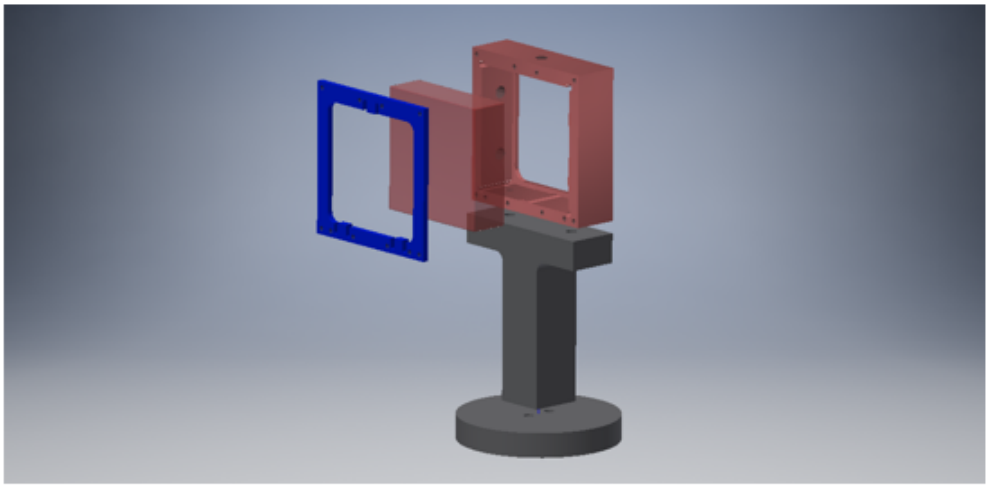

Figure 4.4. The VPH mount has 4 parts: squared mount frame (red), spring frame (blue), mount holder and based plate.

4.4. Lens Cells Mount

The lens mount is designed using the same scheme of VPH mount but in circular shape shown in Fig.4.5. The lens cell design are adjusted its thickness according to thickness of each lens. It is attached to the mount frame (blue) which can separate into two parts: frame and base. The spring frame (black) is used for retaining the lens inside the cell and give small spring force against the cell. All three lenses of the camera part of the spectrograph have the same mount frame and spring frame.

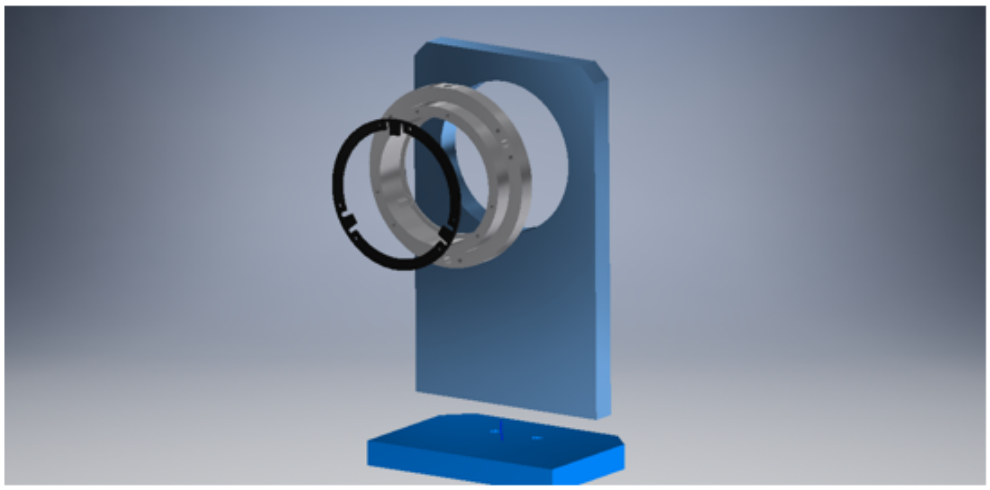

Figure 4.5. The design of Lens mount consists of lens cell (silver), spring frame (black), mount frame and base (blue)

4.5. Fold Mirror Mount

The fold mirror mount is shown in Fig.4.6. The mirror itself is a thin rectangular shape Zerodur with gold coating. The design is expected to be fairly thin since it will be placed in a very crowded area in between the fiber injection unit and the echelle grating mount. The mount frame is kinematics with three hard points. There are two small black spring used to cover the front part of the mirror at the top and bottom tip. The mount frame is mounted to the stand, which can help adjusting small angle between the mirror surface and the light beam by moving a screw in and out at the top of the mount frame. The stand is attached to the base for the propose of height adjustment. It can also be adjusted slightly for the translation direction.

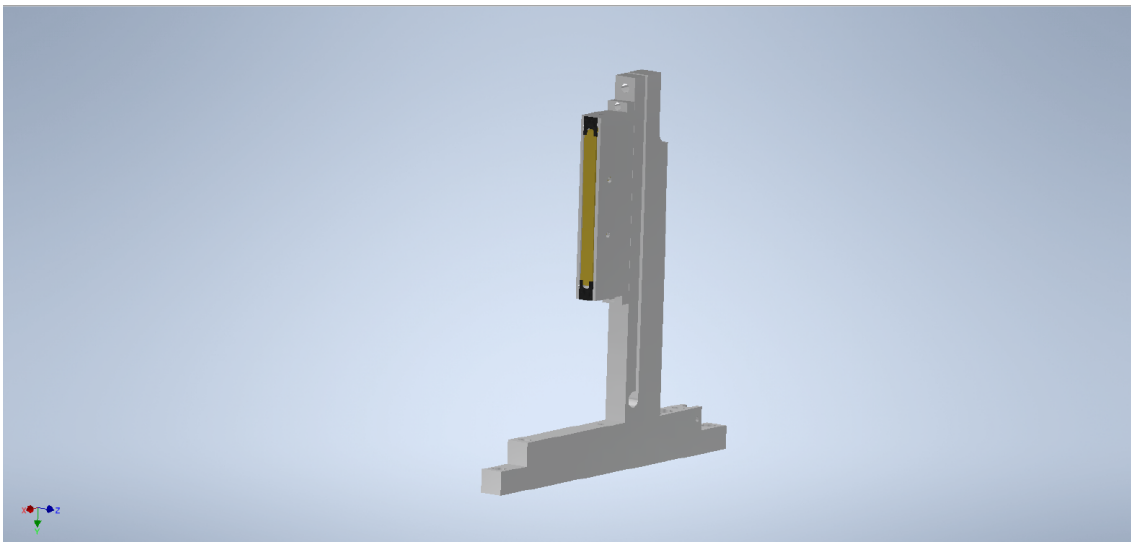

Figure 4.6. The design of the fold mirror mount consists of mirror frame (silver), spring frame (black), mount frame stand and base (silver).

4.6. Assembly

The optomechanical kinetic mounts of all optical components are put together in an assembly along the optical path shown in yellow color in Fig. 4.7. In the real assembly (after this prototype), I plan to cool down the last lens inside a Dewar with an infrared detector so that I can operate the detector at 80 K and decrease the effect of the thermal background.

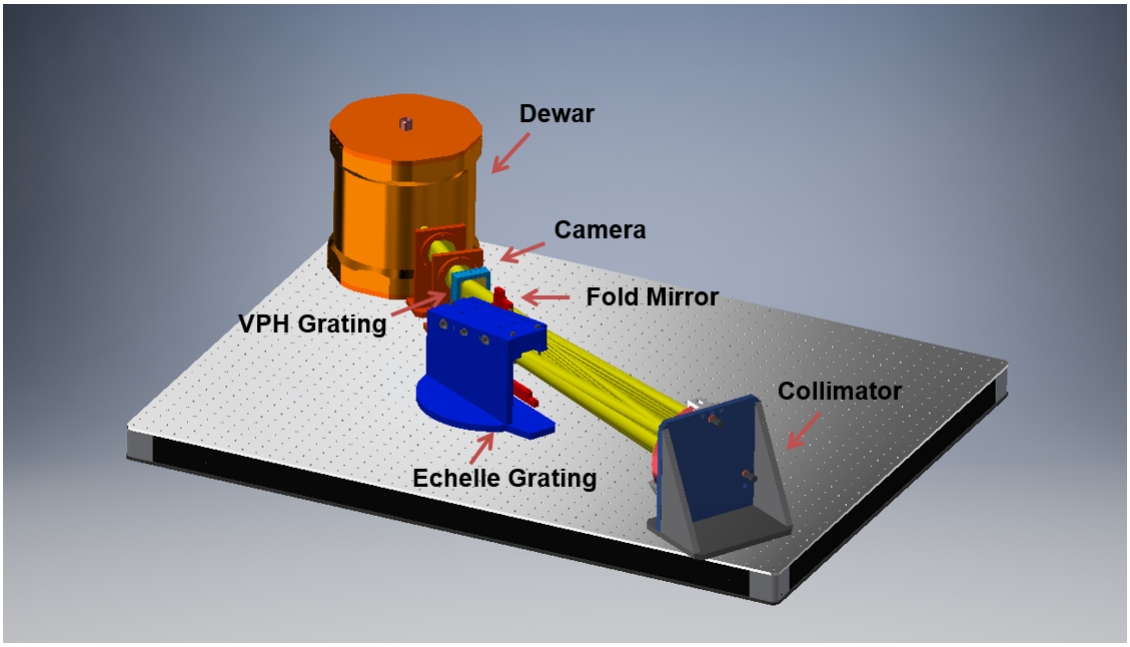

Figure 4.7. TARdYS assembly of the optomechanical mounts along the optical path (yellow) in white pupil configuration.

4.7. Analysis

Most of the optomechanical design for the prototype are designed to allow proper stiffness in the system so that I have almost no change to the optical path. I require the displacement change at the optical component to be less than 2 μm scale on the optical component.

A typical stress analysis workflow is done in Inventor. First I assign the materials to the 3D models. In the 3D model, I only include the major parts in the assembly. Some small structure such as screws are excluded from the simulation. Then I add constraints which specify the fixed position of the mounts. In this case all the mounts are basically attached to the optical table surface. For the mesh I simply assign average mesh size of 0.1 mm since the parts are regular size. The smaller the mesh size, the more computational cost is required. Next I assign the gravity as my load. The assigned gravity load and direction is shown in yellow arrow in Fig.4.8, 4.9, 4.10, 4.11 and 4.12. After running the simulation, the program provides sets of analysis results such as stress, displacement and safety factor.

In the case of collimator in Fig.4.8, the analysis result of the displacement is minimal since the kinematic mount (the ring structure) is placed on a kinematic housing structure. This gives maximum stiffness to collimator mount.

The echelle mount in Fig.4.9 is the tricky part because the echelle grating is facing down. The mount is designed to not let the grating fall down. When I assigned 1G force pulling downward, the maximum displacement in general is $2e-4$ mm showing at the top left corner of the mount because at this side of the mount, I cut down part of the wall to avoid vignetting. At the grating surface, the displacement is not critical, the maximum amount yields $1.2e-4$ mm showing at the corner of the echelle grating.

The small fold mirror mount is a special case. The design is made to allow the tip-tilt adjustment from the top of the mirror using a screw. The maximum displacement of the mirror mount appears to be 0.004 mm at that position. On the mirror surface, the maximum displacement reached 0.0025 mm.

In terms of VPH mount and the camera mount, the displacement due to gravity on the optical surface is not critical. It has average value of $6e-6$ mm on the VPH surface. The camera lens yields $3e-5$ mm in average.

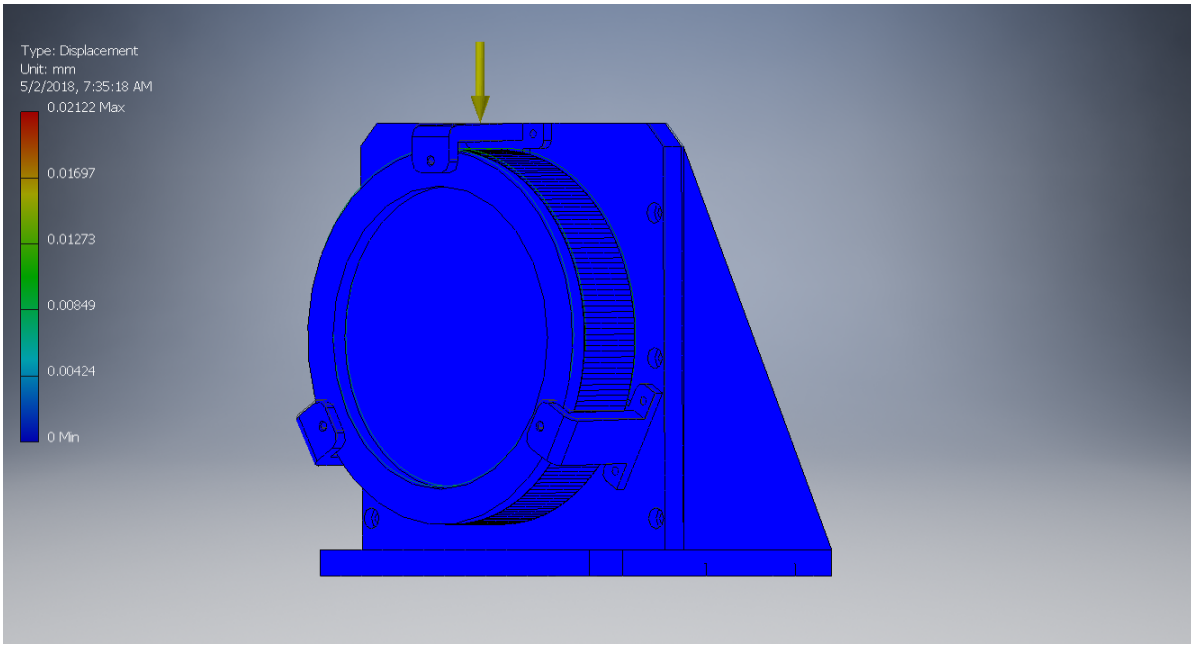

Figure 4.8. The displacement analysis of the collimator mount and housing structure.

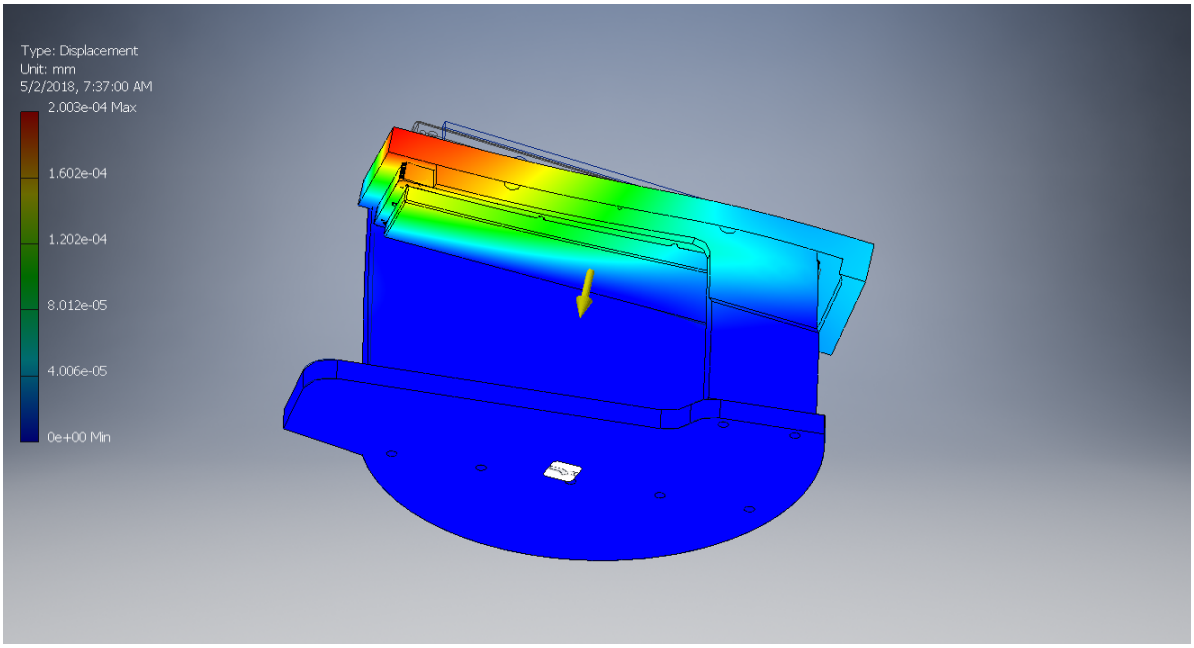

Figure 4.9. The displacement analysis of the echelle mount showing the maximum displacement of $1.2e-4$ mm on one corner of the echelle surface.

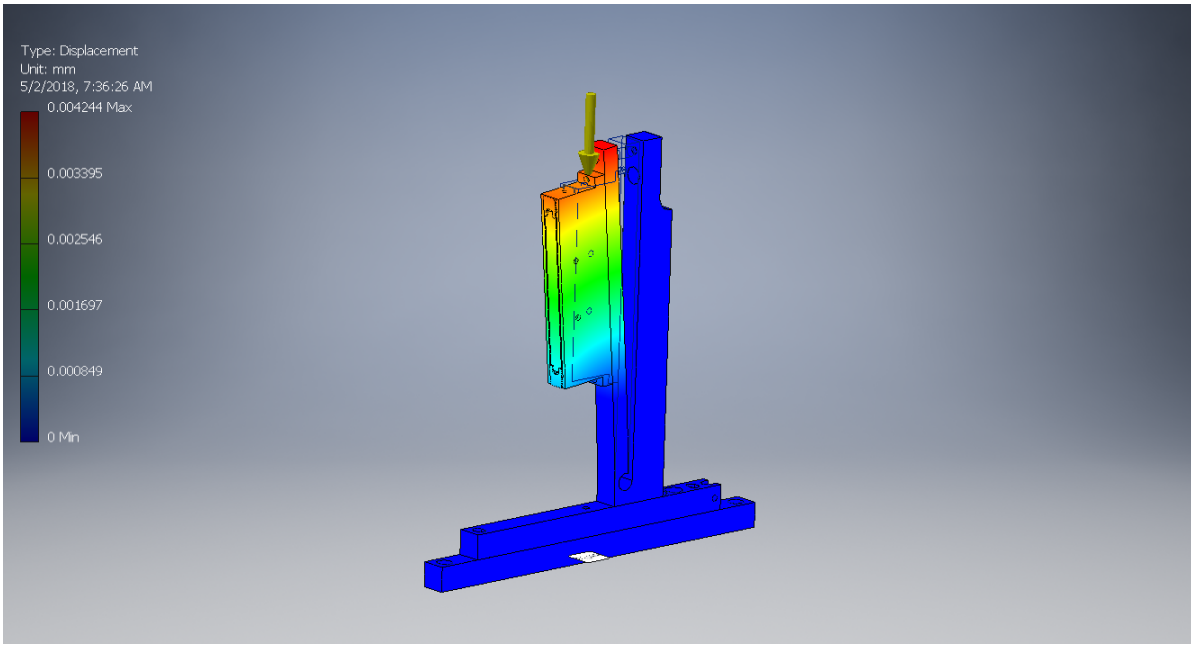

Figure 4.10. The displacement analysis of the fold mirror mount having maximum displacement of 0.004 mm at the top of the mount and 0.002 mm maximum on the mirror surface.

4.7.1. Choice of Breadboard

Optical breadboard is a solution for portable platform to build an optical setup. Nowadays there are various options for commercially available breadboard. The current technology allows better properties of breadboard in terms of damping and stiffness. Damping is the ability to dissipate energy from an induced vibration on the breadboard's surface. Stiffness is the capability to resist the bending to an applied force or load[3] . Thorlabs' recently introduce NEXUS breadboard which yield maximum of both damping and stiffness. However, the breadboard features all-steel construction while the optical mounts are fabricated using Aluminium (Al-6061). Thus a comparison study is done using finite element analysis of the two materials: steel and aluminium as shown in Fig. 4.13 and Fig. 4.14

In the analysis, a collimator and its aluminium mount representing the optical mounts, also because it is the largest mount in the system. The mount is placed on the breadboard

[3]https://www.thorlabs.com/

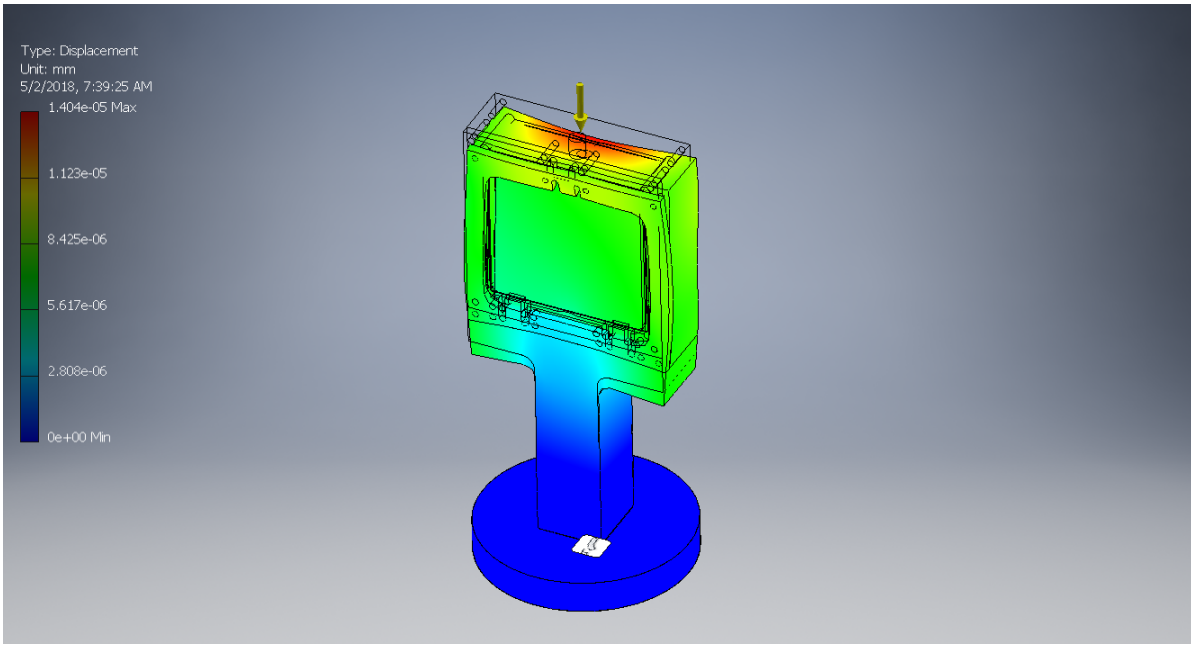

Figure 4.11. The displacement analysis of the VPH mount giving $6e-6$ mm in average on the VPH grating surface.

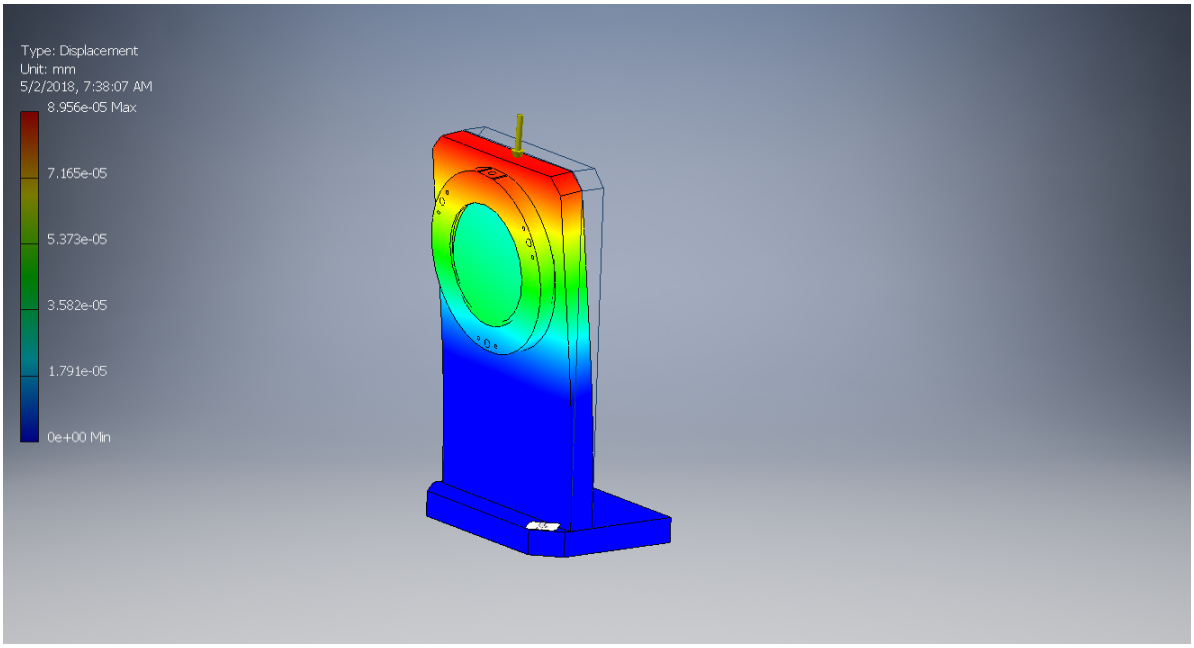

Figure 4.12. The displacement analysis of the camera mount yields about $2e-6$ mm on the lens surface.

made of aluminium (AL) and steel (SL). The system is triggered by pulling (assign a force) at one corner of the breadboard. The two material response differently. In terms of displacement (Fig.4.13), the maximum displacement of AL breadboard is 0.039 mm, peaks at the opposite corner to the assigned force. At the collimator, it yields about 0.015 mm. In case of SL breadboard, the maximum displacement is 0.025 mm, peaks at the optical components directly. This amount is sufficient to shift the optical path to one pixel of size 18 μm.

The stress analysis in Fig.4.14 shows that the AL mount on AL breadboard yields the stress of 0.0027 MPa when the force is applied at one corner of the breadboard. While the SL breadboard yields relatively higher stress of 0.95 MPa.

In the end, the Thorlabs Honey-comb Aluminium breadboard is chosen. One major reason is Thermal Expansion Coefficient since the material applied for the mounts in the system is Aluminium. TARdYS will employ a cooled DEWAR for the objective and detector. This DEWAR will be placed also on the same breadboard for the stability purpose. The temperature of the DEWAR will most likely trigger the temperature stability of the breadboard and that could also affect the optical mount and optical path.

4.7.2. Anodizing

Anodizing is an electrochemical process that converts the metal surface into a decorative, and corrosion-resistant finish. In this case, it adds interference effects to reflected light. Here is an experiment on the option of anodized and non-anodized parts with a simple study by obtaining images using XEVA infrared camera. There are two setups for this experiment exposing with two different light sources: 1) normal room light (Fig.4.15), and 2) flash light reflection (Fig.4.17). The analysis from the normal room light setup shows slight different (approximately 1000 counts) between two different region of anodized and non-anodized shown in Fig.4.16. In the second case of the flash light setup, which has more intensity shows larger different and non-uniform behaviour on the non-anodized piece in Fig.4.18. The additional

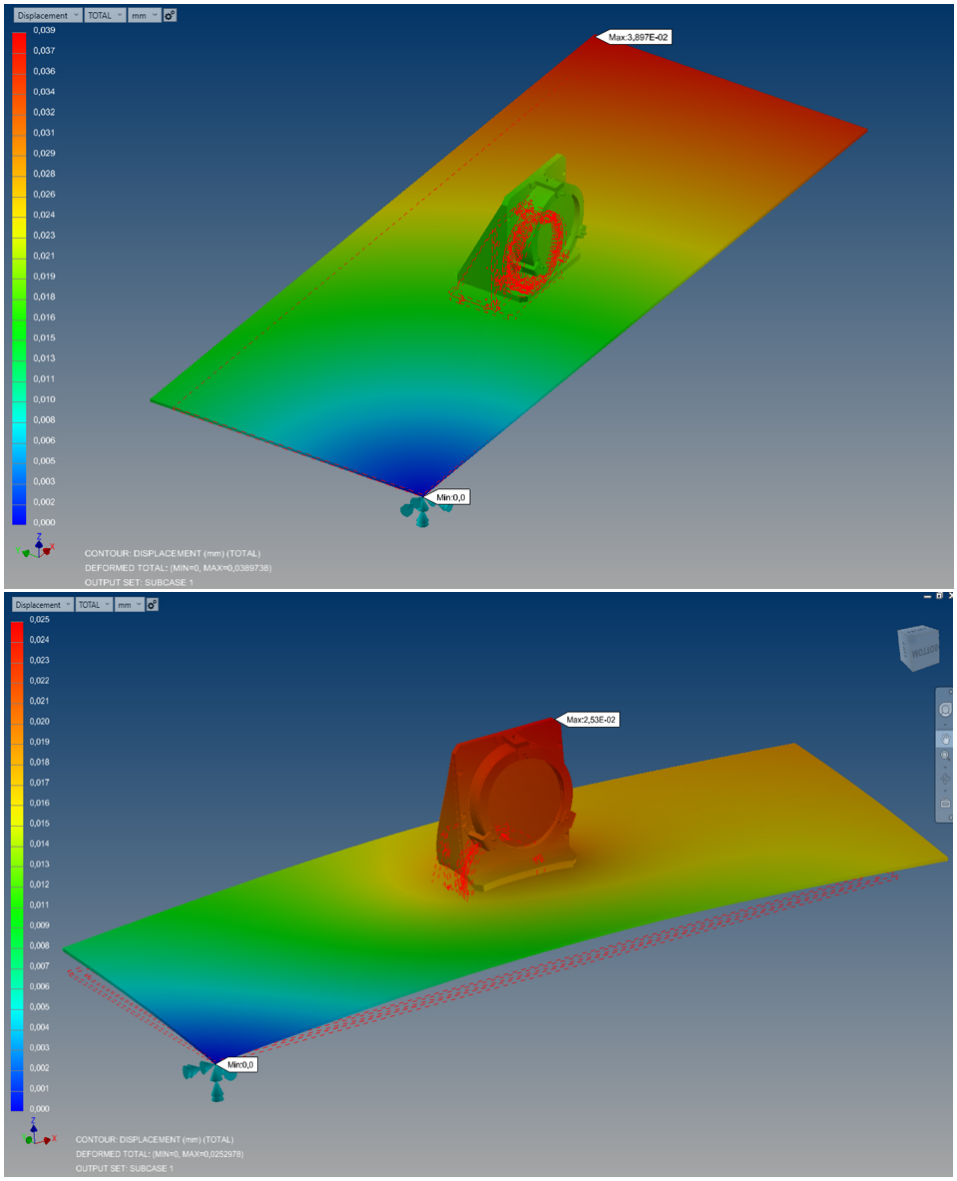

Figure 4.13. The displacement comparison between the aluminium breadboard (top) and steel breadboard (bottom) showing displacement at the optical component on AL breadboard is 0.015 mm and SL breadboard is 0.025 mm.

light is flashed onto the parts. It is clearly shown that once there is additional light flash directly to the parts, the non-anodized part reflects much more than normal condition. Thus, the anodizing is needed for all the aluminium mounts.

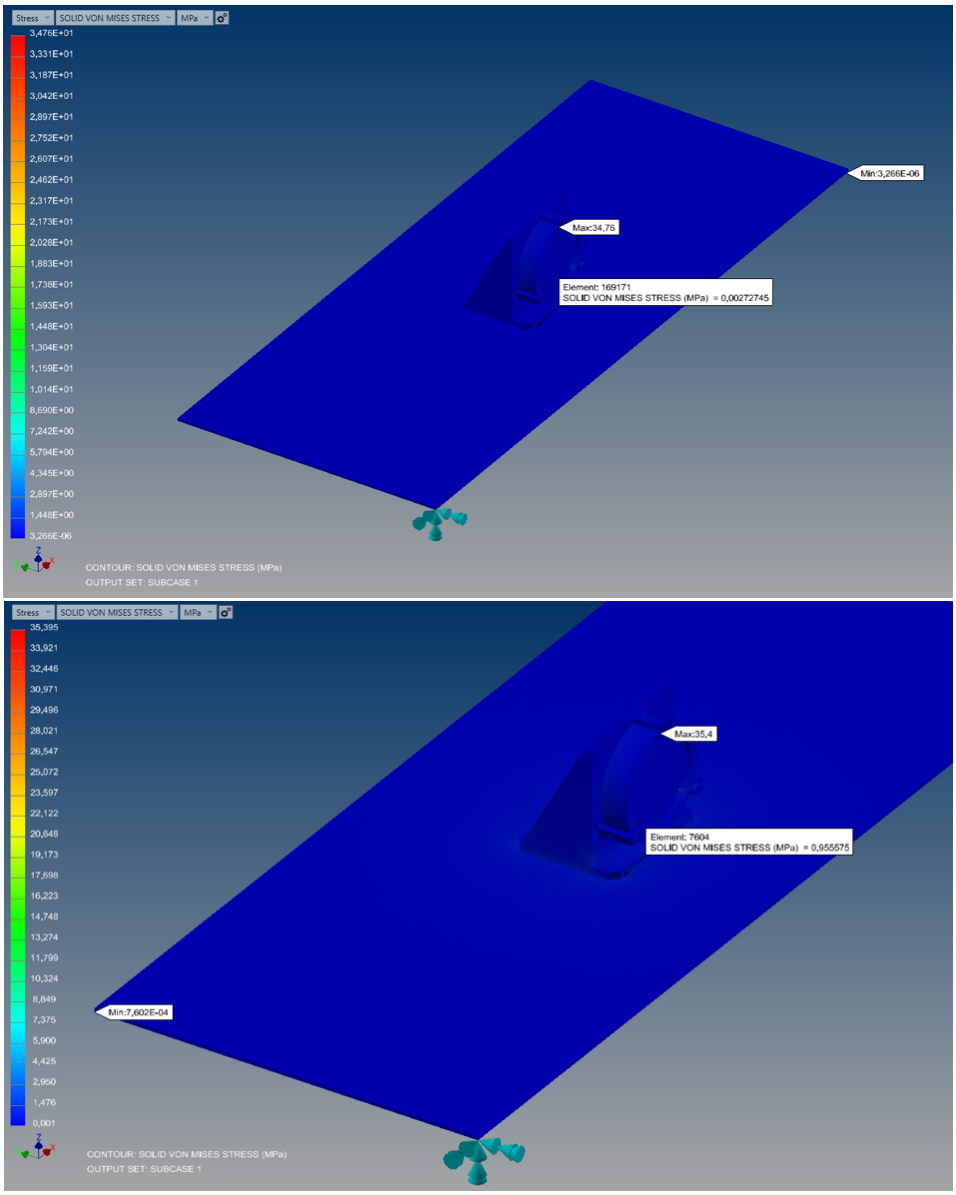

Figure 4.14. The stress comparison between the aluminium breadboard (top) and steel breadboard (bottom) showing the maximum stress of AL breadboard is 0.0027 MPa and SL breadboard is 0.95 MPa.

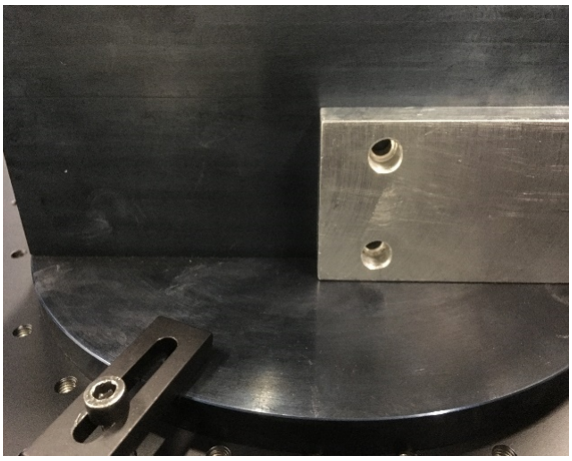

Figure 4.15. Setup of anodized and non-anodized part expose with room light.

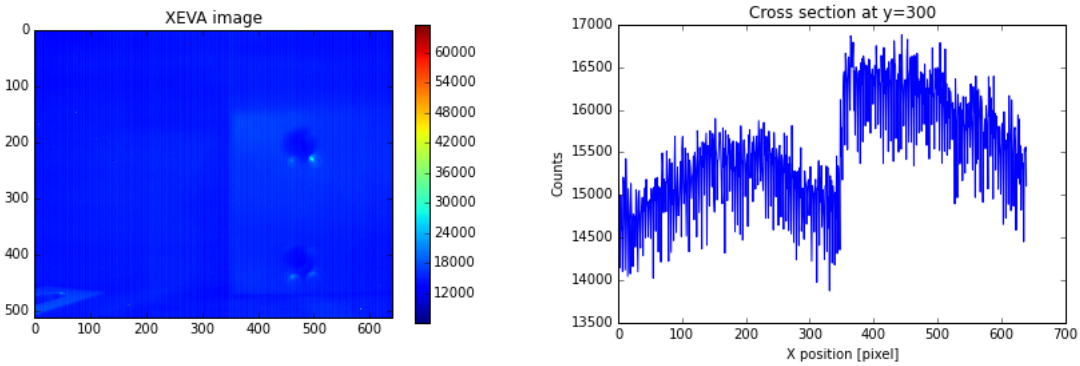

Figure 4.16. (Left) The image of anodized and non-anodized part, exposing to the room light, obtained by XEVA detector. (Right) The cross-section at position y = 300.

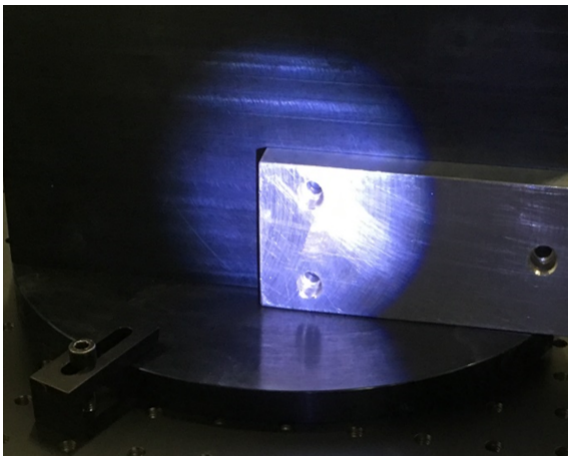

Figure 4.17. Setup of anodized and non-anodized part expose with room light and flashlight. The bright circle in the middle is from the flashlight

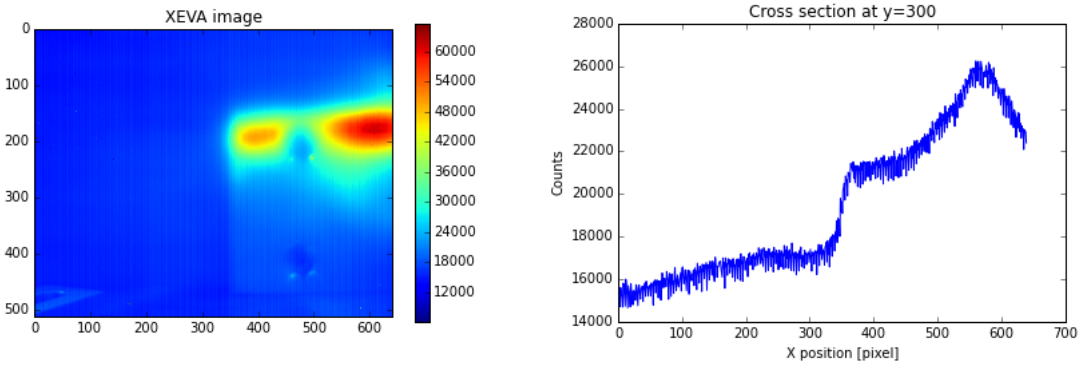

Figure 4.18. (Left) The image of anodized and non-anodized part, exposing to the room light and flashlight, obtained by XEVA detector. (Right) The cross-section at position y = 300.

5. PROTOTYPE AND PERFORMANCE

5.1. Prototype

In this early phase of the project, I construct prototypes of the two different configurations according to this optical design. The main goal of these prototypes is to test the optical components in ambient temperature. I decided to use the optical components optimized for WP configuration. However, I keen to know the behaviour of these components in the QL configuration. Thus I use the same optics set and also align in the QL configuration since it is also less complicated than the WP configuration. I exclude the image slicer in this experiment since its purpose is to boost up the spectral resolution of the spectrograph and the result has already been shown in our previous study such as (Tala et al., 2017), (Vanzi et al., 2018).

5.1.1. Alignment and construction

I assemble the optical components with the mounts. Then an alignment procedure is done using both single mode and multi-mode fiber. First, I find the center of the collimating mirror by placing a beam splitter in front of the mirror as shown in Fig.5.1. I create an image of the fiber to be projected at 550 mm, the focal length distance, from the mirror with a 30 mm achromatic doublet. I employ a single mode fiber, which has a smaller fiber core size than the multi-mode fiber, to collimate the beam and reduce aberration in the system. The image of the single mode fiber is detected using an imaging source camera which has smaller pixel size than the infrared detector. This way the aberration can be observed better. A real-time algorithm is implemented to measure the full width half maximum of the image.

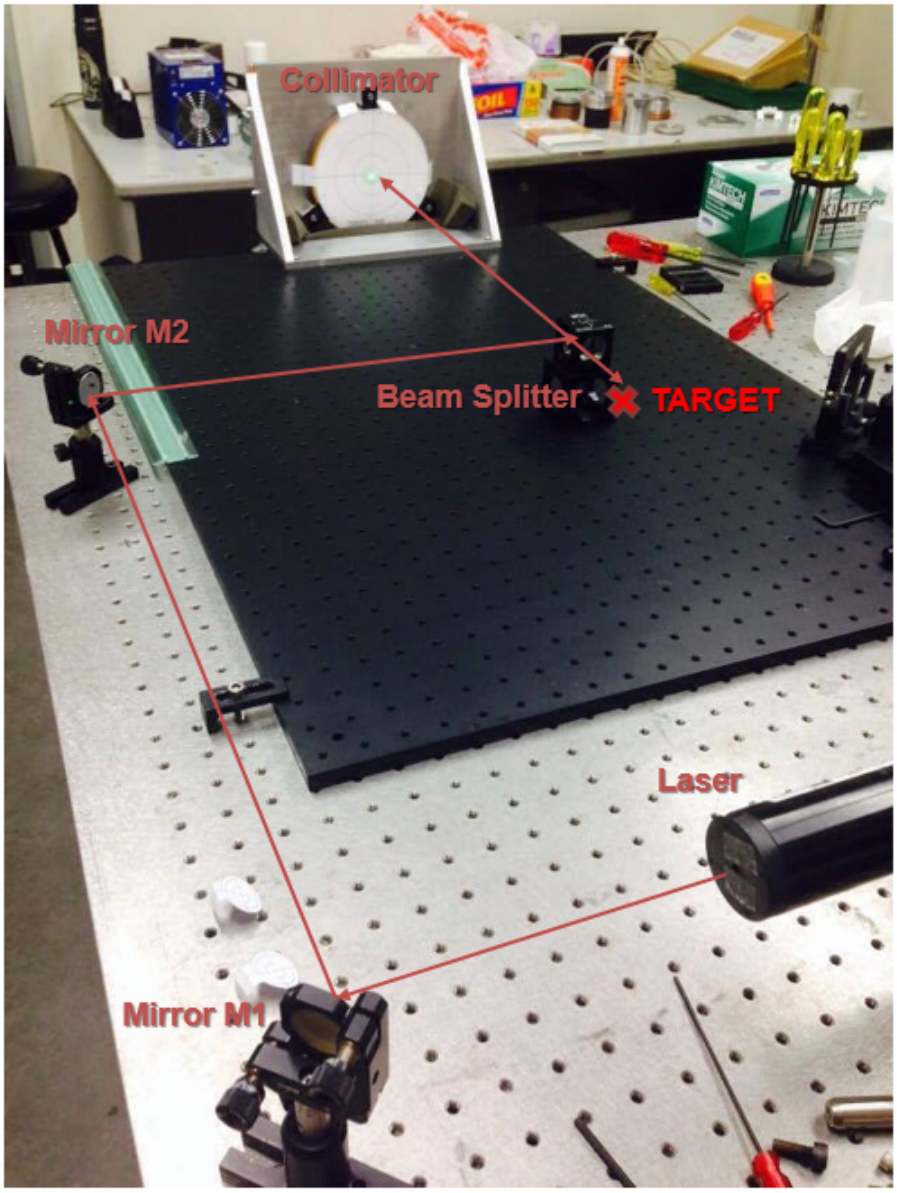

Figure 5.1. The setup to find center of the collimating mirror. There are two fold mirrors and a beam splitter. The red arrows represent light path from the laser source. The target is an aligned position at 550 mm in front of the mirror.

In the quasi-Littrow configuration, before the spectrograph, I have a feeding system (input fiber part) where I use a 30 mm achromatic doublet to create an image of the fiber at 550 mm distance in front of the collimating mirror. This gives the incoming beam of F/19.6. Then the light goes to the collimator, Echelle grating, VPH grating and camera lenses, according to the

optical design as shown in Fig. 5.2. In order to eliminate aberrations, I first use single mode fiber for the input and detect the images using detector with smaller pixel size such as SBIG detector. Later, the multi-mode fiber is used to obtain spectral images. I also fabricate simple spacers for spacing between the camera lenses.

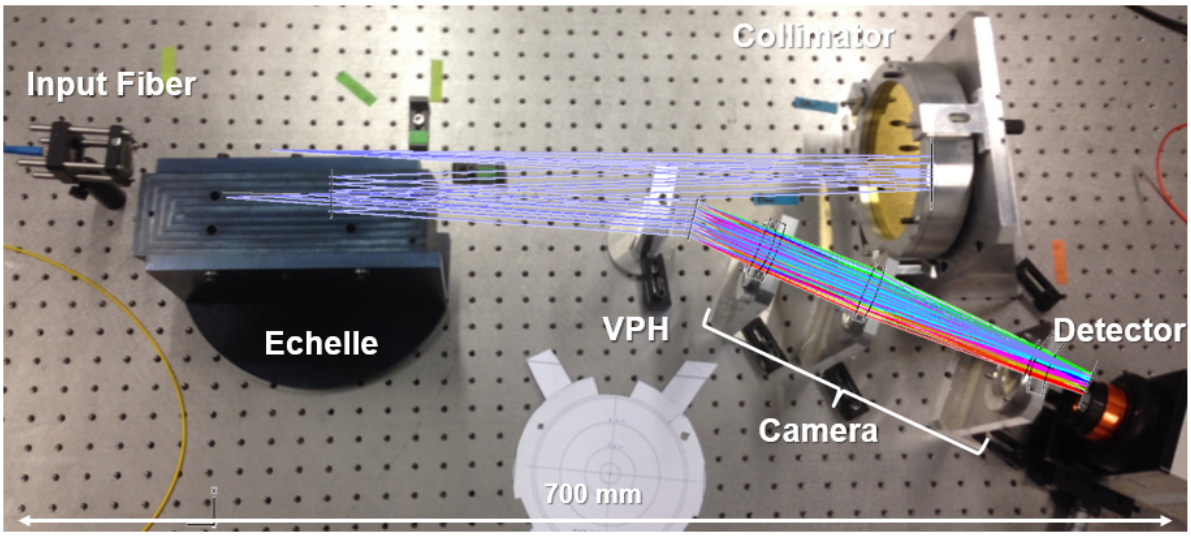

Figure 5.2. The spectrograph prototype of the Littrow configuration overlayed with the ray tracing image, yielding the length of approximately 700 mm.

In the White Pupil Configuration, due to the limited space where Echelle, fold mirror, input optics and VPH grating are located, I adjust the optical design to have a slightly larger angle of the beam reflected on the collimating mirror. In Fig.5.3, I move the Echelle grating closer to the collimator and shift the VPH grating about 30 mm to the back. This results the decreasing of the Strehl ratio (Fig.3.8 bottom part) of about 3-5 $\%$. In the alignment procedure, I apply and repeat the same alignment method as the quasi-littrow configuration. The light path goes to the collimator, Echelle, double pass on the collimator, to fold mirror and again onto the same collimator before going to VPH cross disperser. Then the dispersed light goes through the camera lenses and detector. I overlay the ray tracing on the image of the real setup in Fig.5.3.

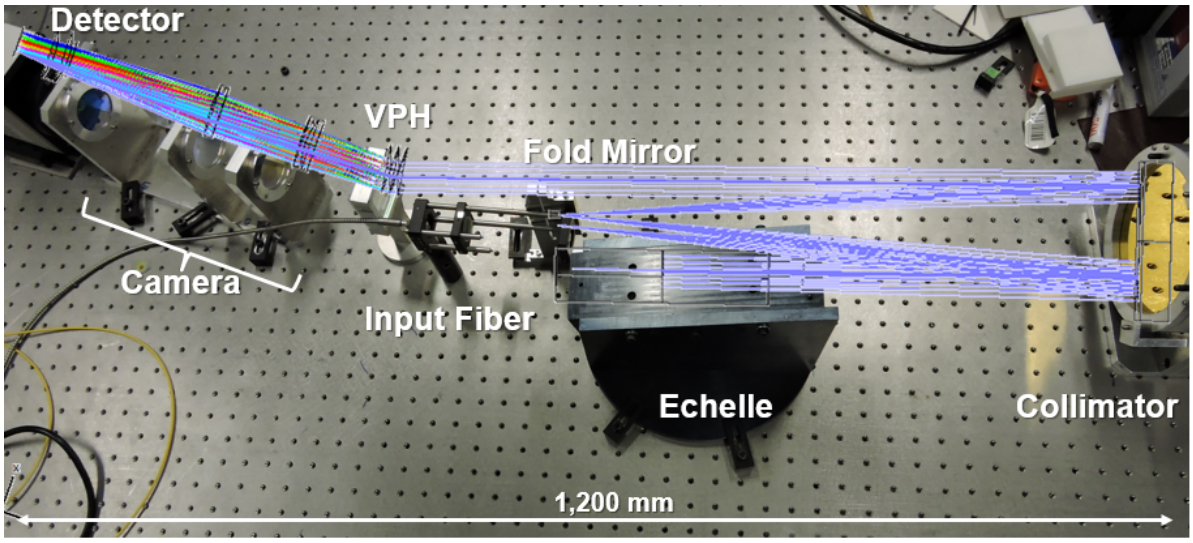

Figure 5.3. The spectrograph prototype of the White Pupil configuration overlayed with the ray tracing image showing double pass on the same collimating mirror. The length of the this configuration reaches approximately 1,200 mm after adjusting the optical design.

5.2. Image Quality

In the preliminary experiment, I want to test the image quality of the system. I use three different detectors to obtain images at different stages. Table 5.1 shows the specification of these detectors:

(i) **Imaging source camera** is a small detector used to obtain all fiber images at different places in the system. It is small enough to move around. I have implemented a small python program to read and analyse FWHM of the image of a single point source real time while using this camera.

(ii) **SBIG** camera has a larger dimension than the imaging source. It is used to take images after the setup is ready in order to have a full field of view of the disperse spectra although the SBIG dimension is much larger than what the system needs. Also it allows user to take FITS images which contain more information than the *.JPG files.

(iii) **XEVA** is an InGaAs infrared detector. It can be mounted with a lens to take infrared images. XEVA comes with its own software from Xeneth working in Windows. At AIUC, in collaboration with the XEVA company, I implemented a XEVA python based interface for reading and writing FITS files in Linux.

Detector	**Dimension**[pixels]	**Pixel pitch** [μm]	**Response**
Imaging Source	640x480	5.6	visible
SBIG	3352x2532	5.4	visible
XEVA	640x512	20.0	infrared

Table 5.1. Specification of different detectors used in the experiment

Spectra: SBIG

Fig.5.4 shows part of spectral images obtain from the SBIG detector using LED and ThAr source respectively. Here I apply a 'FWHM analyser' algorithm to the obtained the FWHM of each spot on the image. In the plot on the right, the FWHM accumulated in range 6-8 pixels corresponding to $\approx 40\mu$m as each pixel of SBIG has 5.4 μm size.

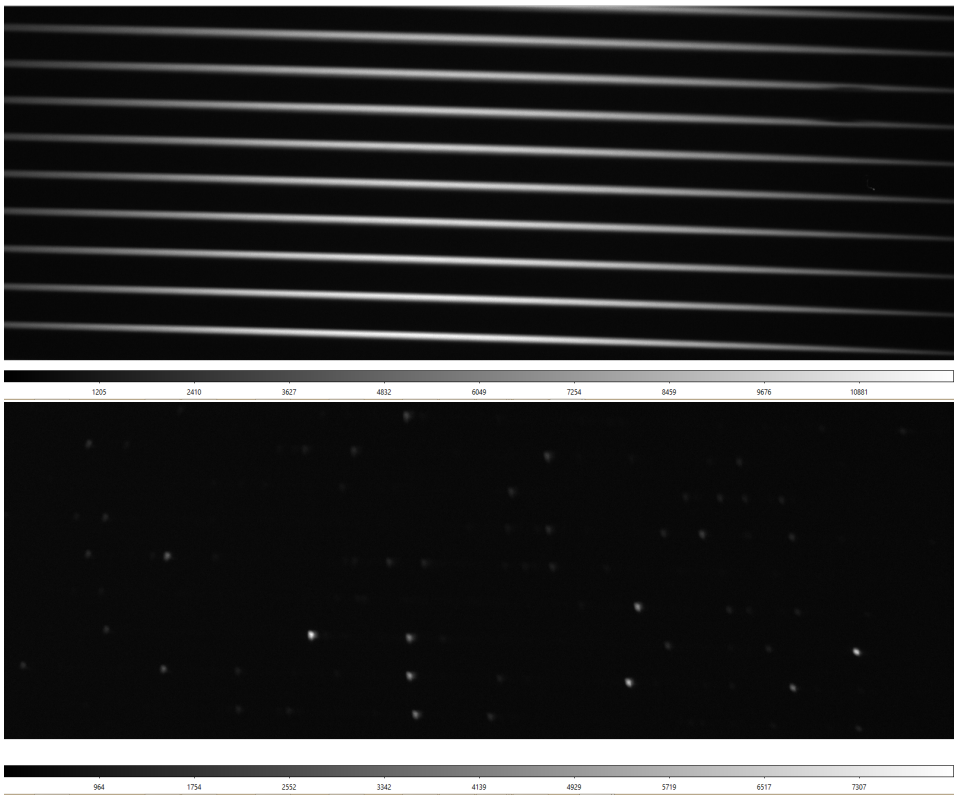

Figure 5.4. Spectal raw images of LED and ThAr obtained with the three lenses spectrograph camera and SBIG detector.

Spectra: XEVA

The same procedure is repeated with XEVA detector in Windows partition and obtain a *.PNG high-resolution files. In this case, the LED light source cannot be detected with XEVA due to the response of the detector. The integration time is set to 0.1 s (highest value allowed by the interface) and cooling to about -150 C. Fig.5.5 shows examples of reduced images obtained from XEVA.

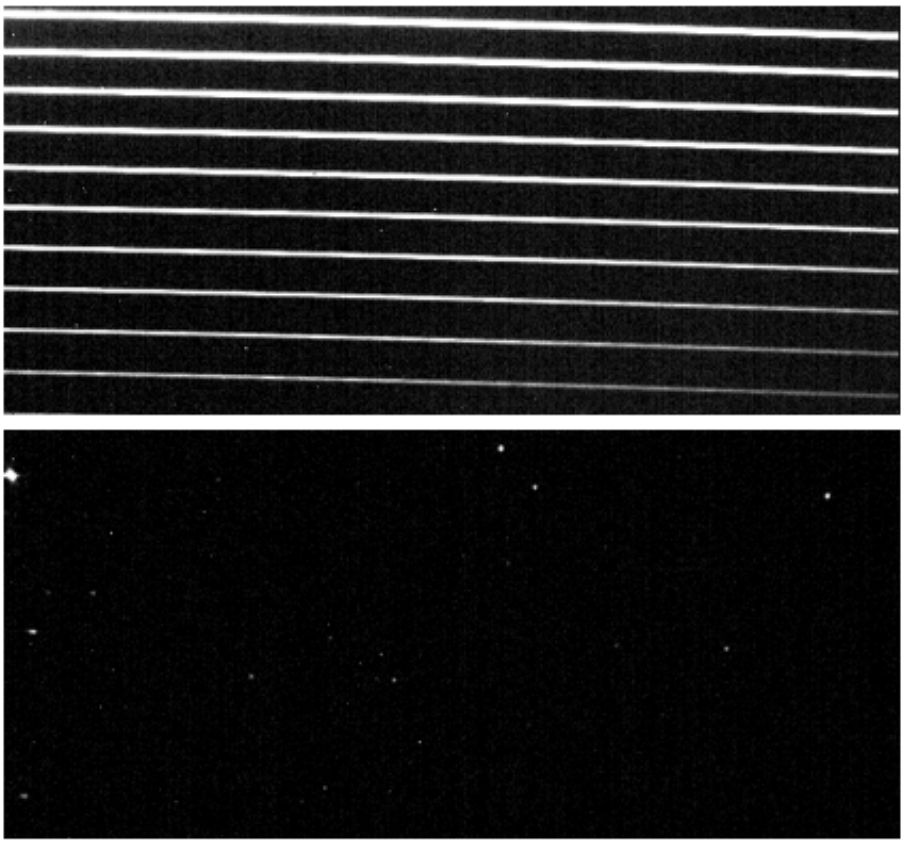

Figure 5.5. Reduced images from XEVA detector showing Continuum IR LED spectrum (top) and ThAr spectrum (bottom) from the same field.

5.2.1. Data acquisition and reduction

In the two prototype setups, I use a commercial InGaAs infrared detector XEVA-1.7-640 which has the dimension of 512x640 pixel of 20 μm size for each pixel. Here I introduce a data reduction and image processing routine to be used particular for this prototype dataset obtained from XEVA detector.

The full field image is a mosaic of the four corners with a relatively large overlapping area. Then I apply a pattern recognition technique to the images in order to merge them together. Each corner consist of a stack of 30 images for a master image. The light image is subtracted

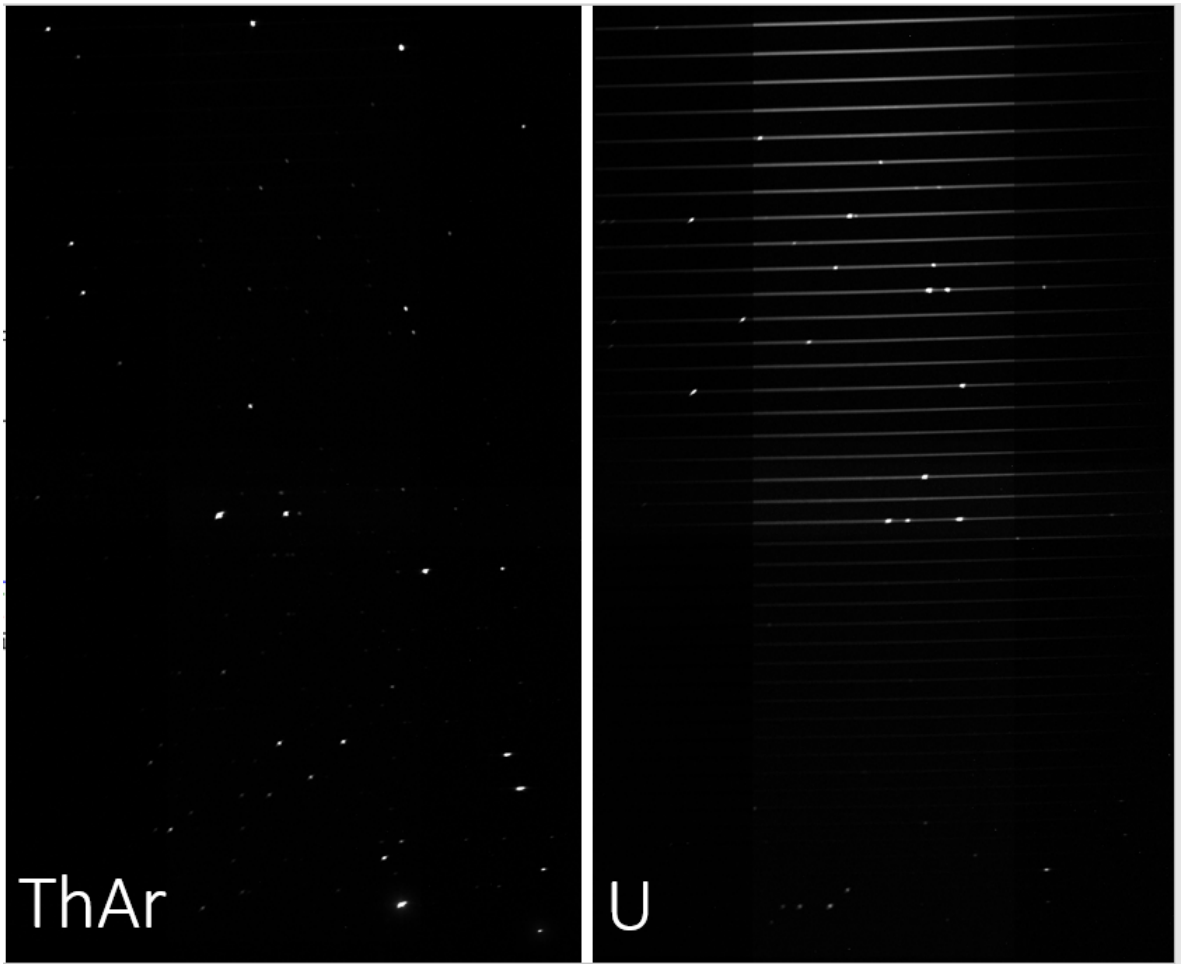

Figure 5.6. The full field merged spectral image obtained from 4 corner positions. The bright region in Uranium (U) spectra is the overlap region. The continuum in the orders is likely from the lamp background in U lamp case.

by a masterdark image. Since the background level of the XEVA detector is relatively high. To normalize the signal levels, I divide by the background level, obtained from the lowest pixel value.

Using a multimode-fiber of 50 μm core diameter size to bring the light into the spectrograph, I made an image of the fiber using one lens of focal length 30 mm coupled with (visible) LED source. The measured size of this slit for a collimated beam is 117 μm as shown in Fig.5.7

The relationship between the image at the entrance and magnification of the spectrograph can be derived as follow: the image at the entrance is 117 μm with the magnification of the system 1/2.75 (550/200 mm) I should get image of spot which has the Full Width Half Maximum (FWHM) of about 43 μm.

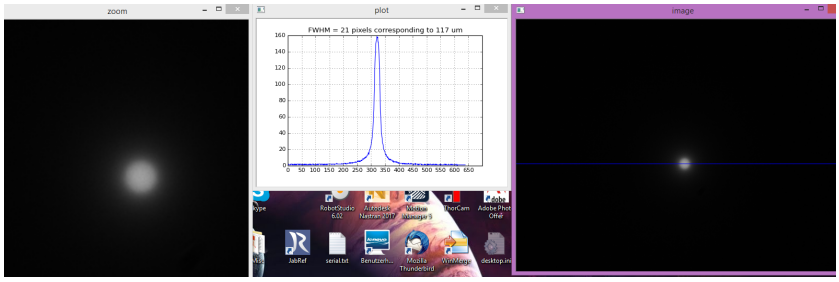

Figure 5.7. The image size of the pseudo-object(slit) from multimode fiber after a 30 mm lens. The FWHM of this image yields 117 μm.

The image quality is analyzed from both prototypes by taking spectral images with a ThAr calibration lamp and the XEVA detector, which has a size of 512x640 pixels, and thus covers only a corner of the full IR detector field. Fig. 5.8 shows FWHM of each spot in one such field. Across all spots, the median FWHM is 2.4 pixels which corresponds to 48 μm. This can be translated to the spectral resolution R = 35,617 at, for example, the 160th order. In the WP configuration, the median FWHM yields 2.15 pixels, corresponding to 43 μm. This improves the image quality by approximately 10%. Note that the image quality comparison is done in the realistic setup i.e. using the image of a mulimode fiber at the input by feeding through input optics. This could cause magnified spots on the image plane unlike the simulation where the input was setup to be a very small point source.

In order to get the full field image from four mosaic patches, first two upper halves are merged together and then merge again the upper halves and lower halves together. In the images obtained from the calibration lamps basically only have spots. I implemented an algorithm to detect all spots of the two frames that I want to merge and overlap the two images. The spots detection is very similar to the one from FWHM analyser. The algorithm is

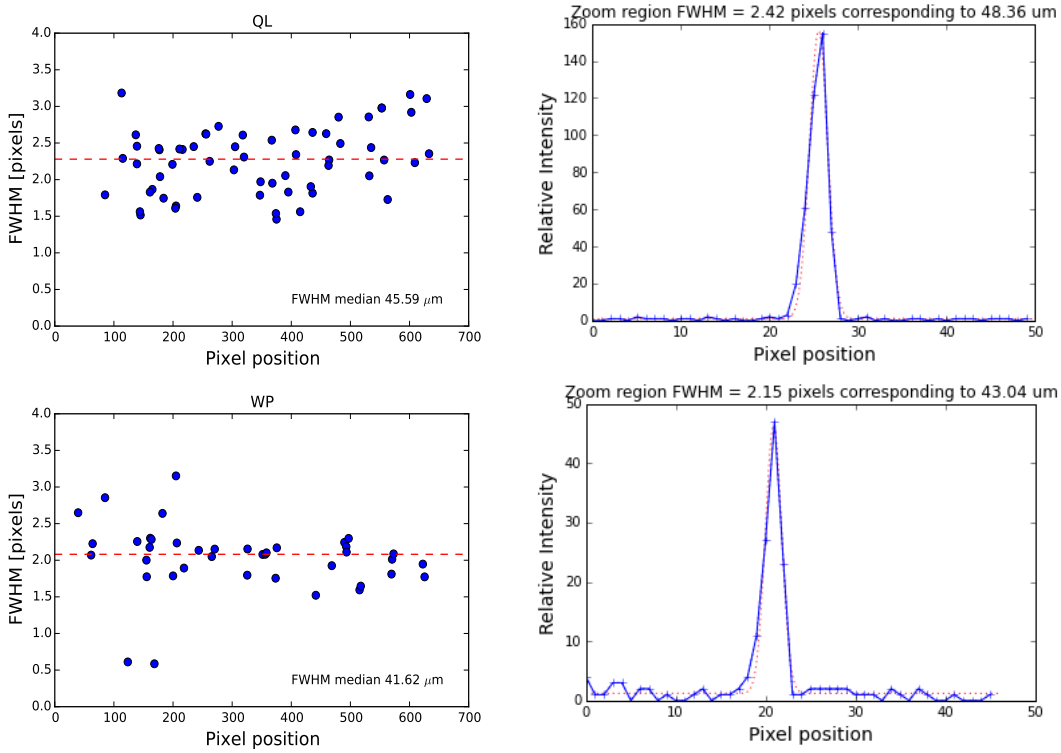

Figure 5.8. Left: The FWHM analysis of one corner of the mosaic patch. This analysis yields median FWHM of 2.4 pixels corresponding to approximately 48 μm from the QL configuration (top) and 2.15 pixels corresponding to 43 μm from WP configuration (bottom). Right: Typical PSF of calibration spot of the field showing the Gaussian fit (red dotted line) of the PSF which also fits the background level simultaneously.

also robust enough to allow the background adjustment so I make sure that the spots use in the stitch program are from the light source not the detector noise. I check the size (FWHM) and intensity of all detected spots, find how good is the matching spots and find the closes distance of the spots. Then I merge the two images at a time according to matching information. In the end, I obtain a merged image of full field spectra as shown in Fig.5.6

5.2.2. Extraction of Spectra

To find the spectral orders, I employ a low cost IR LED of approximate wavelength range 0.86-0.98 μm as my reference because it gives a strong signal that can be observed with

any detector used in this experiment. This range covers about two thirds of the spectral range. Fig.5.9 shows the comparison between the simulated data before. In my simulation, the smallest order separation is 325 μm, which corresponds to about 16 pixels (of 20 μm size per each pixel) of XEVA detector. Each order is extracted using the central wavelength reference together with echellogram calculation (Fig.3.9). To extract more information, I extract with a 3 pixels wide band from every order (limited to the IR continuum reference) and calibrate it with IRAF spectral atlas (Palmer & Engleman, 1983) as shown in Fig.5.10.

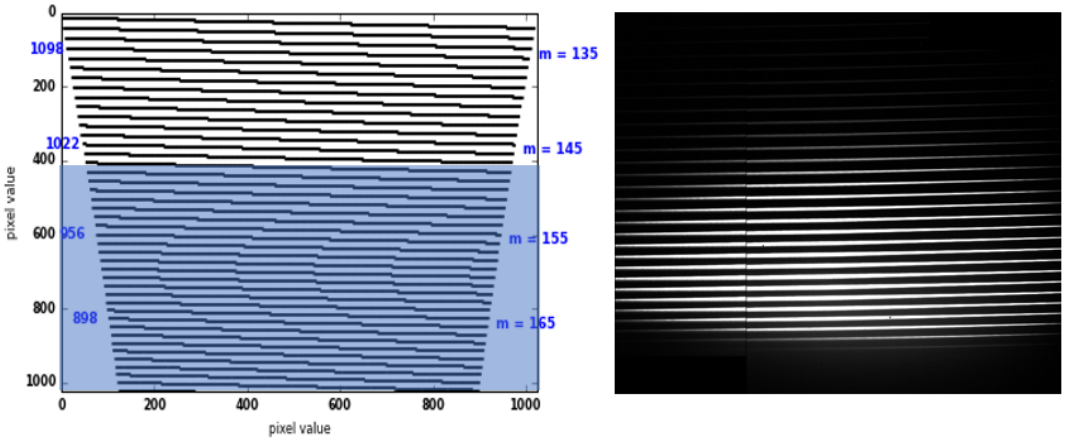

Figure 5.9. Comparison of the simulation (left) and observed continuum spectra (right) obtain from an infrared LED, which has a working wavelength from 0.86-0.98 μm. The obtained spectra (right) corresponds to the 147th-175th order. as shaded in simulation image in blue(left).

5.3. Stability

5.3.1. Wavelength Calibration Source

Wavelength calibration source is worth mentioning here since it plays an important role to achieve RV precision. In optical astronomy, thorium-argon lamps are widely used as a calibration source. However, uranium lamps exhibit more lines in Y-band in the infrared (λ = 0.9-1.1 μm) as shown in Fig. 5.11. The first generation calibration unit is based on FIDEOS

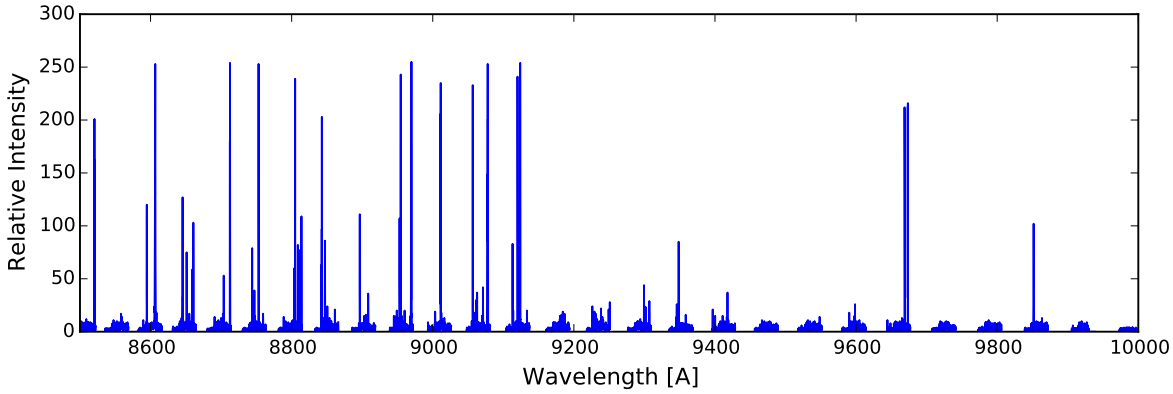

Figure 5.10. Merged spectrum using the IR LED continuum reference on the ThAr calibration image (lower half of Fig.5.6)

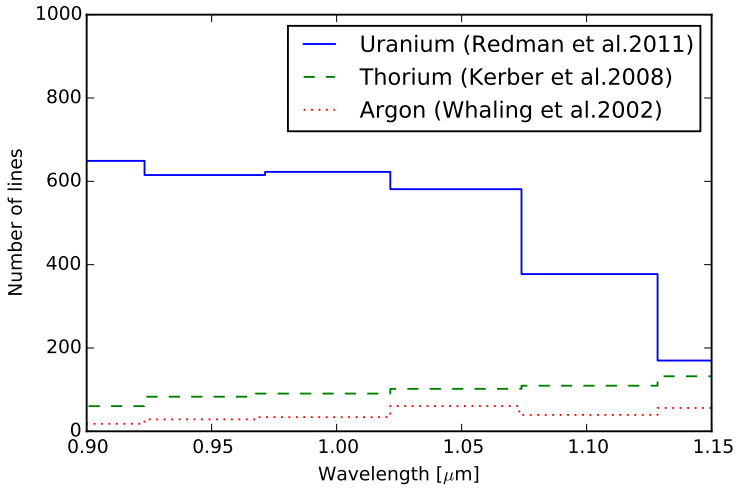

Figure 5.11. Histograms of the number of lines of standard uranium compared with thorium and argon. Note that the distributions are collected from various sources; they are not necessarily proportional to the intrinsic distribution density.

fiber link scheme (Tala et al., 2014). Because of this, I plan to use an uranium lamp instead of the thorium-argon lamp. The multimode fiber receives the image of the calibration source formed by an achromatic doublet lens (f = 30 mm) and feeds the calibration spectrum to the spectrograph fiber link.

5.3.2. Temperature Management

For this prototype experiment, I control the temperature with a very simple and low cost method. The goal is to keep the room, detector and optical bench temperature stable. I control the room temperature with an air-conditioner (AC) set to 22 °C. Without any enclosure, all the spectrograph parts are exposed to the room temperature. One problem of controlling with an AC is that there is fluctuation due to its cycle, in this case ± 1°C approximately every 20 minutes. This fluctuation has a direct effect on the XEVA infrared detector, which I use for this prototype, because XEVA applies electronic cooling (TE3) to cool down using an offset temperature from the ambient environment. Another problem of using this detector is the heat generated from the detector, as it heats up the optical bench through time. I set up different conditions as follows:

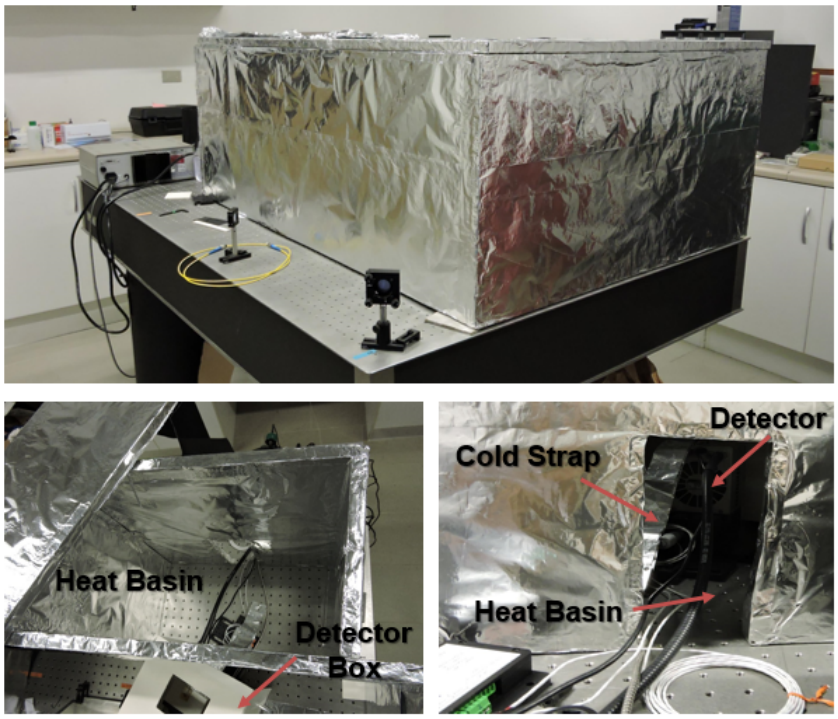

Figure 5.12. The simple implemented enclosure using foam board wrapped with a single layer aluminium foil (top panel). At the back of this enclosure (bottom panel) I attach a heat basin for Experiment 3 which acts as a heat filter between inside and outside of the enclosure through a small opening.

5.3.2.1. Experiment 1: Without enclosure

In the temperature experiments, I place three sensors from Omega Engineering, which comes with the real time reader. The sensors are placed on the top of detector box, optical bench, and on a separate table for the room temperature. This is a controlled experiment. I let all components expose to the air in the room, which is already controlled using an AC set to 22 °C. Note that the AC has particular cycle every 20-30 min if the temperature is set to be 22 °C.

5.3.2.2. Experiment 2: Closed system enclosure

In this experiment, I make an enclosure from foam board wrap with aluminum foil as shown in Fig.5.12 top panel. I close all entrances to the spectrograph system and have the detector inside.

The results of the two experiments are shown in Fig. 5.13 first and second panel. In the experiment 1, I observed strong fluctuations due to the AC cycle observed by all sensors. Therefore I need temperature isolation as exhibited in experiment 2. However, the closed system results an overheating within the system. I then explored various ways for a simple heat release method and finally found a solution as shown in experiment 3.

5.3.2.3. Experiment 3: Semi-opened system enclosure

In this experiment, I extend the enclosure with a heat basin and a thermal-strap on the detector. The main idea of the temperature stability control is not directly expose temperature sensor to the air in the room, which is controlled using AC. Instead, I let the air circulate in the system, balancing stability and room temperature fluctuations. This enclosure in Fig.5.12 consists of three different parts: 1. the main enclosure, 2. the heat basin at the back of the detector and 3. the detector enclosure. The main enclosure covers the main spectrograph optics. The basin area basically acts as air buffer. The XEVA detector that is used for the prototype, generally releases hot air from the back of the detector and cooled air at the side. If

there is no control applied, the air from the detector will disturb the bench temperature sensor. Thus, I also put a small box to cover the detector and the last lens together. The material of this box consists of a very thin layer of foam for the purpose of insulation (Fig.5.12 bottom left). This small box has an opening to the heat basin at the back of the detector. It encloses the side of the detector with another small opening at the top. From some additional experiments, I found that whenever there is closed enclosure over the sensor on the detector at one point the enclosure will be full of hot air and heat up the bench and the detector. I therefore release that hot air to the top so that it does not disturb the temperature stability of the optical bench. The opening at the back of the enclosure let the cool air inside from the bottom to circulate the heat in the system. Additionally, I implement a simple cold strap from 100 aluminum foil sheets (Fig.5.12 bottom right) and connect to the detector box on one end and release the heat to the basin on the other end.

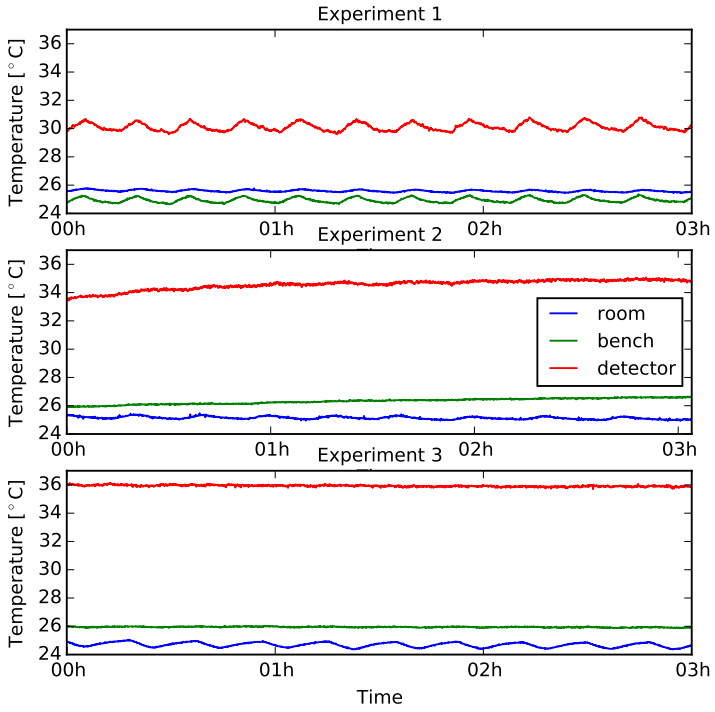

Figure 5.13. Temperature monitoring of the three experiments after the detector reaches a stable temperature.

I compare the three different experiments in Fig. 5.13. I put three sensors on (1) a table in the room (blue line), (2) optical bench (green line), and (3) detector box (red line). The top panel shows the temperature monitoring from experiment 1, without the enclosure. All sensors are triggered according to the air-conditioner (AC) cycle every approximately 20 minutes. The detector sensor heats up the most, following by room and bench. The result from the 'closed environment' experiment 2 is showing in the middle panel. The temperature sensor on the optical bench and detector is not triggered by the room AC cycle anymore. However, both heat up with the increasing temperature of the operating detector. Over the three hours, the bench temperature rose by 0.5 °C, and the detector increased 1.0 °C, continuously. No stable stage is seen in either. Lastly, in the semi-opened system solution (experiment 3), I can control the temperature of the bench and detector stable at the $\pm$ 0.1 °C level and achieve a temperature stable system.

5.3.3. Drift

Together with the temperature control experiment, I also took data from one corner of the full field in order to measure the wavelength stability. This is important because this instrument will measure Doppler line shift over time, tracing the radial velocity of a star as it is orbited by e.g., a planet. The radial velocity drift can be obtained from:

$$v = \frac{\lambda - \lambda_0}{\lambda_0 c} \tag{5.1}$$

where v is radial velocity or the shift measured in km/s, λ is shifted wavelength, λ_0 is the nominal wavelength and c is the speed of light 3×10^{-5} km/s. This measurement is usually performed using a spectrograph with a dispersing element to produce images as a function of wavelength. During the night of an observation run, the falling temperature can minimally change the geometry of the spectrograph, leading to the drifts of the light path. The shift/drift according to the increasing temperature was demonstrated in the study of PUCHEROS spectrograph (Vanzi et al., 2012).

For this prototype experiment, I control the temperature with a very simple method. The goal is to keep the room, detector and optical bench stable within 1 degree. I control the room temperature with an air-conditioner (AC) set to 22 °C in cold mode during the summer and heat mode during the winter. Without any enclosure, all the spectrograph parts are exposed to the room temperature. One problem of controlling with an AC is the fluctuation due to its cycle, in this case ± 1°C approximately every 20 minutes. This fluctuation has a direct effect on the XEVA infrared detector, which I use for this prototype, because XEVA applies electronic cooling (TE3) to cool down using an offset temperature from the ambient environment. Another problem of using this detector is the heat generated from the detector, as it heats up the optical bench over time.

Together with the temperature control experiment, I also took data from one corner of the full field in order to measure the wavelength stability. In this experiment the room temperature is controlled, while the pressure is not. I use a semi-open enclosure and monitor the wavelength shift over 4 hours. Data sets are obtained every 30 minutes.

I found that stabilizing temperature of the detector and the optical bench helps decrease the amplitude of the drift. At a ± 0.1°C control level, the drift varies the amplitude within 1 pixel of 20 μm corresponding to $\approx$ 2 km/s peak to peak in the top panel of Fig. 5.14. Within this range, one can observe that the drift is mostly affected by the environmental pressure (middle panel). This same effect was also observed in our previous study (Vanzi et al., 2018).

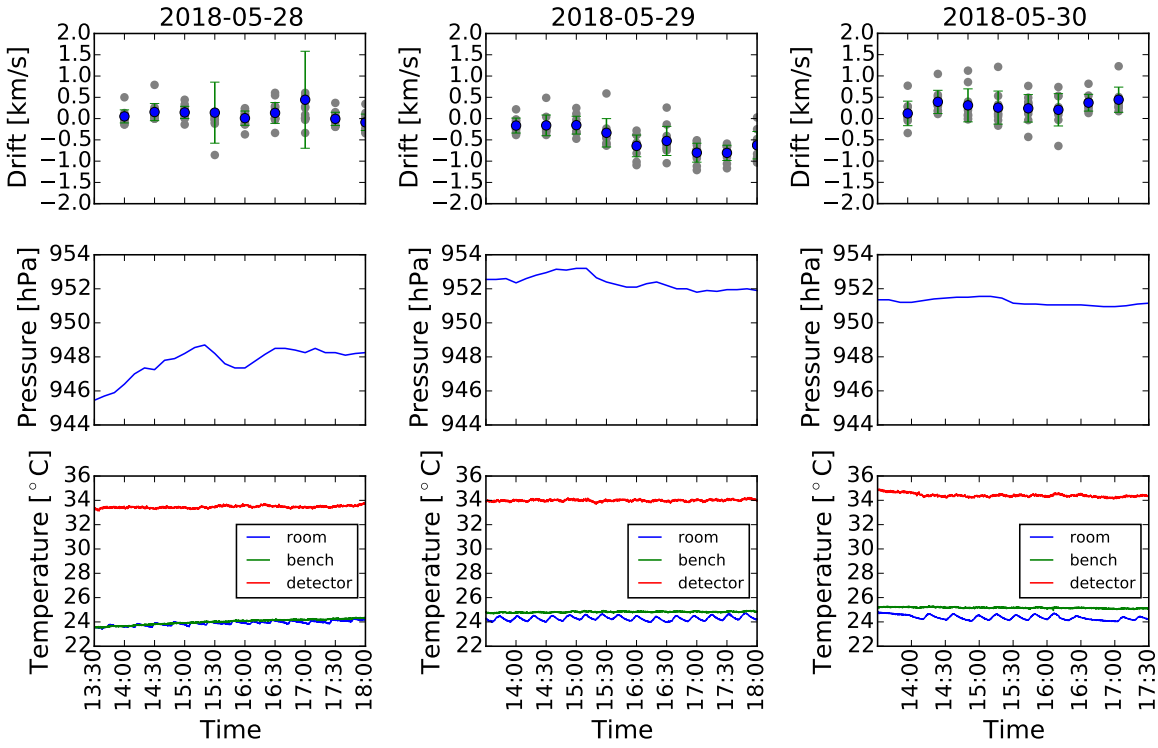

Figure 5.14. The Radial Velocity shift of the ThAr lamp in the AC control environment with enclosure. In the top panel, the gray dots represent sampled data points, and the blue dots represent average value representatives of each data set with green error bar. The middle panel is the measured pressure from the nearby pressure station. The bottom panel is temperature behaviour during the measurement.

5.4. Efficiency Measurement

The efficiency measurement of the VPH grating is done at a photonics laboratory at Macquire University, Sydney, Australia during my internship. The VPH is the cross−disperser in this spectrograph. I setup the experiment as shown in Fig.5.15. A pseudo object is created from the input optics, which consists of a fiber feeding the light, an iris and an achromatic doublet lens, at the distance 550 mm from the collimator. The light goes from the input optics to the collimator, through a beam splitter and to the VPH grating. Working in transmission, I retrieve the measurement at the back of the VPH using Photodiode power sensor 2 (IR). The dispersed orders of the VPH can be observed using a white paper background as shown

in Fig.5.15 in the zoom region on the top left corner. The other light path (P1 in Fig.5.15) from beam splitter goes to power sensor 1 that is used as reference. I use a multi-channel laser source as the input light into the experiment at $\lambda = 650$, 850 and 1300 nm respectively. The experiment was repeated twice and averaged. In Fig.5.16, the average data were fitted using quadratic polynomial fit. The maximum efficiency peaks at about 1000 nm which is the spectrograph central wavelength.

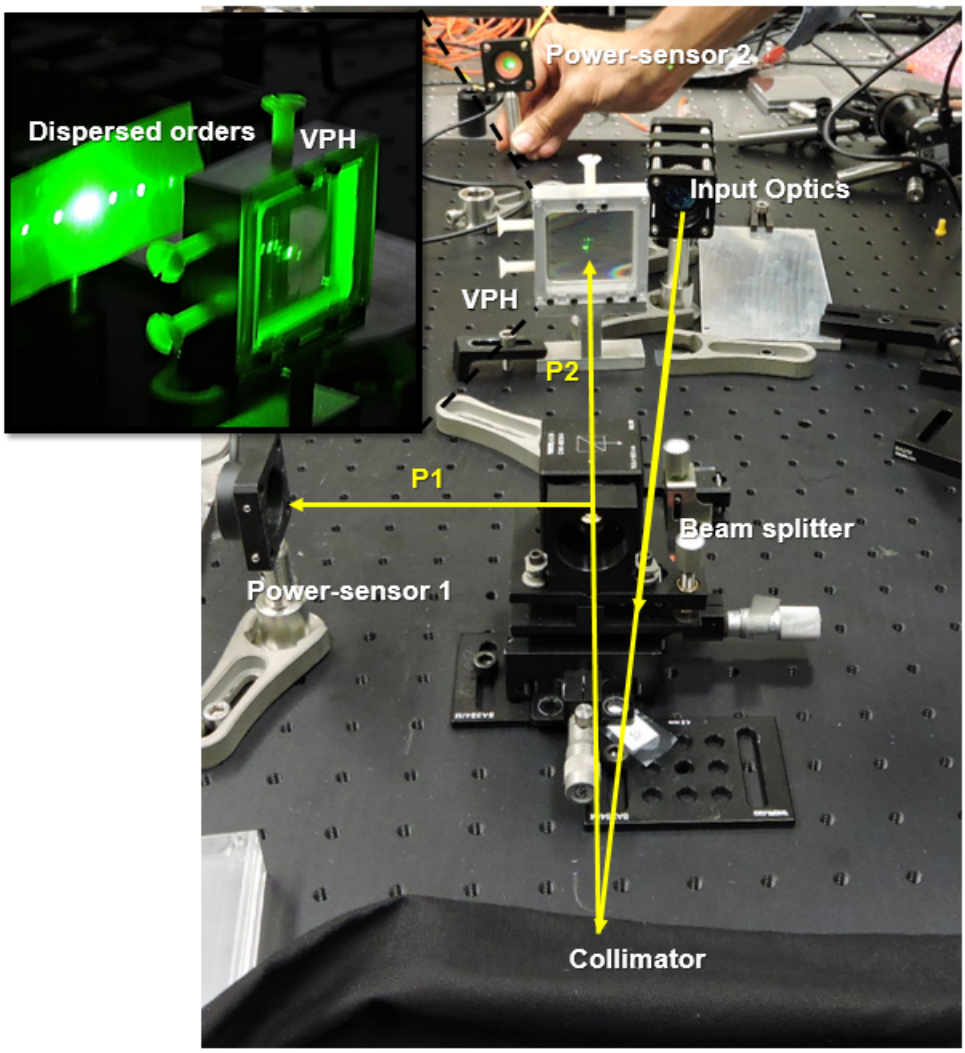

Figure 5.15. The setup for VPH efficiency measurement. The yellow arrows show the ligth path in the measurement setup. I use a beam splitter to split the light into 2 path: P1 and P2 for measurement and reference.

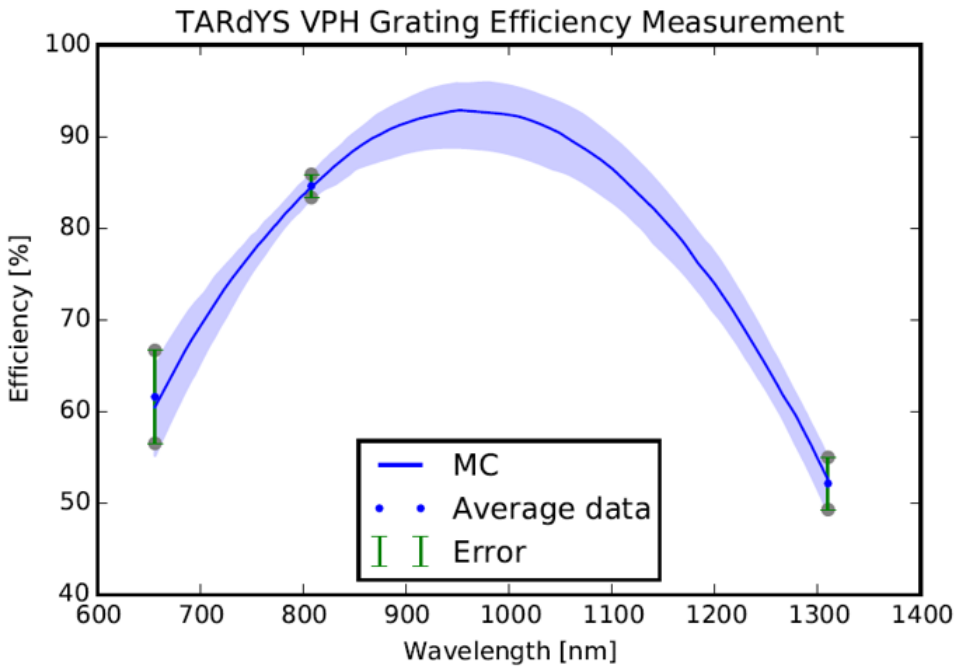

Figure 5.16. The VPH grating efficiency measurement at λ = 650, 850 and 1300 nm. The blue curve is a quadratic polynomial fit.

6. CONCLUSIONS

I present the optical design and prototype of TARdYS, a fiber-fed high resolution near-infrared spectrograph for RV exoplanet search. This novel design uses for the first time an Echelle R6 and an image-slicer optimized for the near-infrared regime.

I explore and compare the designs of two popular spectrograph setups: quasi-Littrow and White Pupil and two newly optimized cameras. The quasi-Littrow configuration shows that it can yield a relatively high strehl ratio with a proper camera design. The Huygen PSF analysis shows a slightly tilted image on the detector plane due to the setup. However, to detect very small shifts on spectral lines of exoplanets, it is required excellent image quality, which I can obtain from the White Pupil design with the same budget by double passing the light on the same collimating mirror and get rid of the anamorphic effect of the image. The Echelle R6, compared with other Echelle types, gives the smallest angle to the instrument by far. This allows us to shrink the volume of the optomechanical mounts and bench, resulting in a compact design. The design packs 42 spectral orders covering Y band (0.843-1.117 μm) onto a 1024x1024 pixels infrared detector, which is the most costly component of the instrument. With an image slicer, it potentially yields spectral resolution of R = 60,000.

The final design of TARdYS, based on the White Pupil configuration, was presented. The 4-lens design camera offers great image quality. The tolerance and thermal analysis of the spectrograph camera predicts diffraction limited performance assuming realistic manufacturing and alignment tolerances. The spectrograph prototype was built in the lab Center of Astro-Engineering UC-AIUC in Chile. I have retrieved preliminary results from the prototype setup using a commercially available infrared detector XEVA. I obtained mosaic a full field image of the Thorium-Argon spectra and IR continuum source using a pattern recognition technique. The result agrees well with the simulation, given the median image quality of 2.4 pixels FWHM corresponding to spectral resolution of approximately 35,000 without an image slicer. The image quality improve by 8-10% in the WP configuration. I also applied a simple temperature stability control to the prototype using an air conditioner and a semi-open

enclosure to circulate the heat within the system. This results in a change of $\pm$ 0.1 K over several hours. Stabilizing the temperature of the detector and optical bench temperature helps to decrease the amplitude of the velocity drift. Within the range of 2 km/s, the trend of the drift is mostly affected by the environmental pressure.

The next phase of the project will include the integration of the detector, Dewar and a better-structured stability control. I plan to use a Uranium lamp as a calibrator instead of Thorium-Argon combining with Fabry-Perot Etalon. TARdYS will open up opportunities for high-resolution Y-band infrared spectroscopy including studies of M-dwarfs and searches for the exoplanets.

REFERENCES

Angel, J. R. P., Adams, M. T., Boroson, T. A., & Moore, R. L. (1977, December). A very large optical telescope array linked with fused silica fibers. ApJ, *218*, 776-782. doi: 10.1086/155734

Anglada-Escudé, G., Amado, P. J., Barnes, J., Berdiñas, Z. M., Butler, R. P., Coleman, G. A. L., ... Zechmeister, M. (2016, August). A terrestrial planet candidate in a temperate orbit around Proxima Centauri. NATURE, *536*, 437-440. doi: 10.1038/nature19106

Anna Brucalassi, F. L. L. W. C. F. H. K. S. M. H. U. H. R. B., Frank Grupp. (2013). *Pressure and temperature stabilization of an existing Échelle spectrograph iv* (Vol. 8864). Retrieved from http://dx.doi.org/10.1117/12.2023274 doi: 10.1117/12.2023274

Artigau, É., Kouach, D., Donati, J.-F., Doyon, R., Delfosse, X., Baratchart, S., ... Figueira, P. (2014, July). SPIRou: the near-infrared spectropolarimeter/high-precision velocimeter for the Canada-France-Hawaii telescope. In *Ground-based and airborne instrumentation for astronomy v* (Vol. 9147, p. 914715). doi: 10.1117/12.2055663

Bailey, J., Simpson, A., & Crisp, D. (2007). Correcting infrared spectra for atmospheric transmission. *Publications of the Astronomical Society of the Pacific*, *119*(852), 228. Retrieved from http://stacks.iop.org/1538-3873/119/i=852/a=228

BaileyIII, J. I., White, R. J., Blake, C. H., Charbonneau, D., Barman, T. S., Tanner, A. M., & Torres, G. (2012). Precise infrared radial velocities from keck/nirspec and the search for young planets. *The Astrophysical Journal*, *749*(1), 16. Retrieved from http://stacks.iop.org/0004-637X/749/i=1/a=16

Balan, S. T., & Lahav, O. (2009, July). EXOFIT: Bayesian Estimation of Orbital Parameters of Extrasolar Planets. *ArXiv e-prints*.

Ballard, S. (2018, January). Predicted Number, Multiplicity, and Orbital Dynamics of TESS M Dwarf Exoplanets. *ArXiv e-prints*.

Baranne, A. (1972, June). Equipement spectrographique du foyer coudé du télescope de 3.60 mètres. Etude de faisabilité d'un spectrographe universel. In S. Laustsen & A. Reiz (Eds.), *Auxiliary instrumentation for large telescopes* (p. 227-239).

Barden, S., Arns, J., Colburn, W., & Williams, J. (2000). Volume-phase holographic gratings and the efficiency of three simple volume-phase holographic gratings. *Publications of the Astronomical Society of the Pacific*, *112*(772), 809–820. Retrieved from http://www.jstor.org/stable/10.1086/316576

Barnes, J. R., Jenkins, J. S., Jones, H. R. A., Jeffers, S. V., Rojo, P., Arriagada, P., ... Anglada-Escudé, G. (2014, April). Precision radial velocities of 15 M5-M9 dwarfs. MNRAS, *439*, 3094-3113. doi: 10.1093/mnras/stu172

Bean, J. L., Seifahrt, A., Hartman, H., Nilsson, H., Wiedemann, G., Reiners, A., ... Henry, T. J. (2010). The crires search for planets around the lowest-mass stars. i. high-precision near-infrared radial velocities with an ammonia gas cell. *The Astrophysical Journal*, *713*(1), 410. Retrieved from http://stacks.iop.org/0004-637X/713/i=1/a=410

Ben-Ami, S., López-Morales, M., Garcia-Mejia, J., Gonzalez Abad, G., & Szentgyorgyi, A. (2018, May). High Resolution Spectroscopy using Fabry Perot Intereferometer Arrays: An Application to Searches for O_2 in Exoplanetary Atmospheres. *ArXiv e-prints*.

Berdja, A., Vanzi, L., Jordán, A., & Koshida, S. (2012, September). An echelle

spectrograph for precise radial velocity measurements in the near IR. In *Ground-based and airborne instrumentation for astronomy iv* (Vol. 8446, p. 844681). doi: 10.1117/12.925572

Bershady, M. A. (2009, October). 3D Spectroscopic Instrumentation. *ArXiv e-prints*.

Bonfils, X., Delfosse, X., Udry, S., Forveille, T., Mayor, M., Perrier, C., ... Bertaux, J.-L. (2013, January). The HARPS search for southern extra-solar planets. XXXI. The M-dwarf sample. A&A, *549*, A109. doi: 10.1051/0004-6361/201014704

Caffau, E., Andrievsky, S., Korotin, S., Origlia, L., Oliva, E., Sanna, N., ... Bonifacio, P. (2016, January). GIANO Y-band spectroscopy of dwarf stars: Phosphorus, sulphur, and strontium abundances. A&A, *585*, A16. doi: 10.1051/0004-6361/201527272

Carleo, I., Sanna, N., Gratton, R., Benatti, S., Bonavita, M., Oliva, E., ... Sissa, E. (2016, June). High precision radial velocities with GIANO spectra. *Experimental Astronomy*, *41*, 351-376. doi: 10.1007/s10686-016-9492-3

Cersullo, F., Wildi, F., Chazelas, B., & Pepe, F. (2017, May). A new infrared Fabry-Pérot-based radial-velocity-reference module for the SPIRou radial-velocity spectrograph. A&A, *601*, A102. doi: 10.1051/0004-6361/201629972

Charbonneau, D., Berta, Z. K., Irwin, J., Burke, C. J., Nutzman, P., Buchhave, L. A., ... Forveille, T. (2009, December). A super-earth transiting a nearby low-mass star. *Nature*, *462*, 891. Retrieved from `http://dx.doi.org/10.1038/nature08679`

Claudi, R., Benatti, S., Carleo, I., Ghedina, A., Molinari, E., Oliva, E., ... Riverol, C. (2016, August). GIARPS: the unique VIS-NIR high precision radial velocity facility in this world. In *Ground-based and airborne instrumentation for astronomy vi* (Vol. 9908, p. 99081A). doi: 10.1117/12.2231845

Cotton, D. V., Bailey, J., & Kedziora-Chudczer, L. (2014, March). Atmospheric modelling for the removal of telluric features from infrared planetary spectra. MNRAS, *439*, 387-399. doi: 10.1093/mnras/stt2465

Crossfield, I. J. M., Ciardi, D. R., Petigura, E. A., Sinukoff, E., Schlieder, J. E., Howard, A. W., ... Defrere, D. (2016, September). 197 Candidates and 104 Validated Planets in K2's First Five Fields. ApJS, *226*, 7. doi: 10.3847/0067-0049/226/1/7

Dumusque, X., Borsa, F., Damasso, M., Díaz, R. F., Gregory, P. C., Hara, N. C., ... Udry, S. (2017, February). Radial-velocity fitting challenge. II. First results of the analysis of the data set. A&A, *598*, A133. doi: 10.1051/0004-6361/201628671

Dumusque, X., Udry, S., Lovis, C., Santos, N. C., & Monteiro, M. J. P. F. G. (2011, January). Planetary detection limits taking into account stellar noise. I. Observational strategies to reduce stellar oscillation and granulation effects. A&A, *525*, A140. doi: 10.1051/0004-6361/201014097

Feroz, F., Balan, S. T., & Hobson, M. P. (2011, September). Bayesian evidence for two companions orbiting HIP 5158. MNRAS, *416*, L104-L108. doi: 10.1111/j.1745-3933.2011.01109.x

Ford, E. B., & Gregory, P. C. (2007, November). Bayesian Model Selection and Extrasolar Planet Detection. In G. J. Babu & E. D. Feigelson (Eds.), *Statistical challenges in modern astronomy iv* (Vol. 371, p. 189).

Fraunhofer, J. (n.d.). Kurzer bericht von den resultaten neuerer versuche über die gesetze des lichtes, und die theorie derselben. *Annalen der Physik*, *74*(8), 337-378. Retrieved from `https://onlinelibrary.wiley.com/doi/abs/10.1002/andp.18230740802` doi: 10.1002/andp.18230740802

Gerardo Avila, T. B., Carlos Guirao. (2012). High efficiency inexpensive 2-slices image

slicers. In (Vol. 8446, p. 8446 - 8446 - 6). Retrieved from http://dx.doi.org/10.1117/12.927448 doi: 10.1117/12.927448

Giovanelli, R., Darling, J., Sarazin, M., Yu, J., Harvey, P., Henderson, C., ... Swain, M. (2001, July). The Optical/Infrared Astronomical Quality of High Atacama Sites. I. Preliminary Results of Optical Seeing. PASP, *113*, 789-802. doi: 10.1086/322135

Gratton, R. G., Bhatia, R., & Cavazza, A. (2000, June). Asymmetric White-Pupil Collimators for High-Resolution Spectrographs. Applied Optics, *39*, 2614-2619. doi: 10.1364/AO.39.002614

Grimm, S. L., Demory, B.-O., Gillon, M., Dorn, C., Agol, E., Burdanov, A., ... Queloz, D. (2018, June). The nature of the TRAPPIST-1 exoplanets. A&A, *613*, A68. doi: 10.1051/0004-6361/201732233

Harrison, G. R. (1949a, Jun). The production of diffraction gratingsi. development of the ruling art∗. *J. Opt. Soc. Am.*, *39*(6), 413–426. Retrieved from http://www.osapublishing.org/abstract.cfm?URI=josa-39-6-413 doi: 10.1364/JOSA.39.000413

Harrison, G. R. (1949b, Jul). The production of diffraction gratings: Ii. the design of echelle gratings and spectrographs1. *J. Opt. Soc. Am.*, *39*(7), 522–528. Retrieved from http://www.osapublishing.org/abstract.cfm?URI=josa-39-7-522 doi: 10.1364/JOSA.39.000522

Hearnshaw, J. (2009). *Astronomical spectrographs and their history*. Cambridge University Press. doi: 10.1017/CBO9780511735288

Herbst, T. M. (1994, December). Numerial evaluation of OH-suppression instruments. PASP, *106*, 1298-1309. doi: 10.1086/133507

Hill, G. J., MacQueen, P. J., Palunas, P., Shetrone, M. D., & Booth, J. A. (2006, June).

Present and future instrumentation for the Hobby-Eberly Telescope. In *Society of photo-optical instrumentation engineers (spie) conference series* (Vol. 6269, p. 626907). doi: 10.1117/12.672642

Hillenbrand, L. A., Foster, J. B., Persson, S. E., & Matthews, K. (2002). The y band at 1.035 microns: Photometric calibration and the dwarfstellar/substellar color sequence. *Publications of the Astronomical Society of the Pacific*, *114*(797), 708. Retrieved from http://stacks.iop.org/1538-3873/114/i=797/a=708

Ida, S., & Lin, D. N. C. (2004, March). Toward a Deterministic Model of Planetary Formation. I. A Desert in the Mass and Semimajor Axis Distributions of Extrasolar Planets. ApJ, *604*, 388-413. doi: 10.1086/381724

Jenkins, J. S., Ramsey, L. W., Jones, H. R. A., Pavlenko, Y., Gallardo, J., Barnes, J. R., & Pinfield, D. J. (2009, October). Rotational Velocities for M Dwarfs. ApJ, *704*, 975-988. doi: 10.1088/0004-637X/704/2/975

Jones, A., Noll, S., Kausch, W., & Kimeswenger, S. (2014, June). An Advanced Scattered Moonlight Model. In *American astronomical society meeting abstracts #224* (Vol. 224, p. 405.03).

Kamizuka, T., Miyata, T., Sako, S., Ohsawa, R., Okada, K., Uchiyama, M. S., ... Yoshii, Y. (2016). *Development status of the mid-infrared two-field camera and spectrograph mimizuku for the tao 6.5-m telescope* (Vol. 9908). Retrieved from https://doi.org/10.1117/12.2231565 doi: 10.1117/12.2231565

Lanza, A. F., Boisse, I., Bouchy, F., Bonomo, A. S., & Moutou, C. (2011, September). Deriving the radial-velocity variations induced by stellar activity from high-precision photometry. Test on HD 189733 with simultaneous MOST/SOPHIE data. A&A, *533*, A44. doi: 10.1051/0004-6361/201117270

Le, H. A. N., Pak, S., Jaffe, D. T., Kaplan, K., Lee, J.-J., Im, M., & Seifahrt, A. (2015). Exposure time calculator for immersion grating infrared spectrograph: {IGRINS}. *Advances in Space Research*, *55*(11), 2509 - 2518. Retrieved from http://www.sciencedirect.com/science/article/pii/S0273117715001908 doi: https://doi.org/10.1016/j.asr.2015.03.007

Leviton, D. B., & Frey, B. J. (2008, May). Temperature-dependent absolute refractive index measurements of synthetic fused silica. *ArXiv e-prints*.

Lord, S. D. (1992, December). *A new software tool for computing Earth's atmospheric transmission of near- and far-infrared radiation* (Tech. Rep.).

Lovis, C., & Fischer, D. (2010, December). Radial Velocity Techniques for Exoplanets. In S. Seager (Ed.), *Exoplanets* (p. 27-53).

Ma, B., & Ge, J. (2012, May). A New Multi-band Radial Velocity Technique for Detecting Exoplanets around Active Stars. ApJ, *750*, 172. doi: 10.1088/0004-637X/750/2/172

Mace, G., Jaffe, D., Park, C., & Lee, J.-J. (2016, June). Stellar Radial Velocities with IGRINS at McDonald Observatory. In *19th cambridge workshop on cool stars, stellar systems, and the sun (cs19)* (p. 55). doi: 10.5281/zenodo.56434

Mackenzie, F. (2003). *Our changing planet: An introduction to earth system science and global environmental change*. Prentice Hall. Retrieved from https://books.google.cl/books?id=M_1EAQAAIAAJ

Mahadevan, S., Ramsey, L. W., Terrien, R., Halverson, S., Roy, A., Hearty, F., ... Nelson, M. (2014, July). The Habitable-zone Planet Finder: A status update on the development of a stabilized fiber-fed near-infrared spectrograph for the for the Hobby-Eberly telescope. In *Ground-based and airborne instrumentation for astronomy v* (Vol.

9147, p. 91471G). doi: 10.1117/12.2056417

Maihara, T., Iwamuro, F., Yamashita, T., Hall, D. N. B., Cowie, L. L., Tokunaga, A. T., & Pickles, A. (1993, September). Observations of the OH airglow emission. PASP, *105*, 940-944. doi: 10.1086/133259

Mann, A. W., Gaidos, E., Mace, G. N., Johnson, M. C., Bowler, B. P., LaCourse, D., ... Jaffe, D. T. (2016, February). Zodiacal Exoplanets in Time (ZEIT). I. A Neptune-sized Planet Orbiting an M4.5 Dwarf in the Hyades Star Cluster. ApJ, *818*, 46. doi: 10.3847/0004-637X/818/1/46

Martin, E. C., Fitzgerald, M. P., McLean, I. S., Adkins, S. M., Aliado, T., Brims, G., ... Weiss, J. (2014). *Performance modeling of an upgraded nirspec on keck* (Vol. 9147). Retrieved from `https://doi.org/10.1117/12.2056896` doi: 10.1117/12.2056896

Mayor, M., & Queloz, D. (1995, November). A Jupiter-mass companion to a solar-type star. NATURE, *378*, 355-359. doi: 10.1038/378355a0

Meinel, I. A. B. (1950, May). OH Emission Bands in the Spectrum of the Night Sky. ApJ, *111*, 555. doi: 10.1086/145296

Moehler, S., Modigliani, A., Freudling, W., Giammichele, N., Gianninas, A., Gonneau, A., ... Vinther, J. (2014, August). Flux calibration of medium-resolution spectra from 300 nm to 2500 nm: Model reference spectra and telluric correction. A&A, *568*, A9. doi: 10.1051/0004-6361/201423790

Motohara, K. M. T. H. K. N. M. K. Y. K. Y. T. Y. O. H. A. T. D. M. K. T. K. K. M. T. M. T. M.-T. M. K. O. K. S. S. S. T. T. Y. T. T. T. M. T. K. U. M. S. K. S. A. K. T. K. U. M. T. S., K., & Yoshii, Y. (2016). *Nir camera and spectrograph swims for tao 6.5m telescope: overview and development status* (Vol. 9908). Retrieved from

https://doi.org/10.1117/12.2231386 doi: 10.1117/12.2231386

Murray, C. D., & Dermott, S. F. (2000). *Solar System Dynamics*.

Nelson, B. E., Ford, E. B., Buchner, J., Cloutier, R., Díaz, R. F., Faria, J. P., ... Rukdee, S. (2018, June). Quantifying the Evidence for a Planet in Radial Velocity Data. *ArXiv e-prints*.

Noll, S., Kausch, W., Kimeswenger, S., Barden, M., Jones, A. M., Modigliani, A., ... Taylor, J. (2014, July). Skycorr: A general tool for spectroscopic sky subtraction. A&A, *567*, A25. doi: 10.1051/0004-6361/201423908

Nutzman, P., & Charbonneau, D. (2008, March). Design Considerations for a Ground-Based Transit Search for Habitable Planets Orbiting M Dwarfs. PASP, *120*, 317. doi: 10.1086/533420

Oliva, E., & Origlia, L. (1992, February). The OH Airglow Spectrum - a Calibration Source for Infrared Spectrometers. A&A, *254*, 466.

Oliva, E., Origlia, L., Baffa, C., Biliotti, C., Bruno, P., D'Amato, F., ... Sozzi, M. (2006, June). The GIANO-TNG spectrometer. In *Society of photo-optical instrumentation engineers (spie) conference series* (Vol. 6269, p. 626919). doi: 10.1117/12.670006

Osterbrock, D. E., Fulbright, J. P., & Bida, T. A. (1997). Night-sky high-resolution spectral atlas of oh emission lines for echelle spectrograph wavelength calibration. ii. *Publications of the Astronomical Society of the Pacific*, *109*(735), 614-627. Retrieved from http://www.jstor.org/stable/40680935

Pak, S., Jaffe, D. T., Stacey, G. J., Bradford, C. M., Klumpe, E. W., & Keller, L. D. (2004, July). Near-Infrared Molecular Hydrogen Emission from the Central Regions of Galaxies: Regulated Physical Conditions in the Interstellar Medium. ApJ, *609*, 692-709. doi: 10.1086/421233

Palmer, B. A., & Engleman, R. (1983). *Atlas of the Thorium spectrum*.

Palmer, C. (2014). *Diffraction grating handbook (7th edition)*.

Paul Martini, D. L. D. (2000). *Optimal resolutions for ir spectroscopy through the oh airglow* (Vol. 4008). Retrieved from http://dx.doi.org/10.1117/12.395526 doi: 10.1117/12.395526

Pepe, F., Ehrenreich, D., & Meyer, M. R. (2014, September). Instrumentation for the detection and characterization of exoplanets. NATURE, *513*, 358-366. doi: 10.1038/nature13784

Perryman, M. (2011). *The Exoplanet Handbook*.

Peter P. Plavchan, P. G. J. K. W. B. M. D. C. S. C. S. L. C. B. C. B. J. J. C. D. R. W. G. A.-E. K. v. B. G. V. L. P. S. K. A. T. B. W. S. M., M. Bottom. (2013). *Precision near-infrared radial velocity instrumentation ii: noncircular core fiber scrambler* (Vol. 8864). Retrieved from http://dx.doi.org/10.1117/12.2023696 doi: 10.1117/12.2023696

Quirrenbach, A., Amado, P. J., Caballero, J. A., Mundt, R., Reiners, A., Ribas, I., ... Xu, W. (2014, July). CARMENES instrument overview. In *Ground-based and airborne instrumentation for astronomy v* (Vol. 9147, p. 91471F). doi: 10.1117/12.2056453

Ramsey, L. W. (1988). Focal ratio degradation in optical fibers of astronomical interest. In S. C. Barden (Ed.), *Fiber optics in astronomy* (Vol. 3, p. 26-39).

Reiners, A., Bean, J. L., Huber, K. F., Dreizler, S., Seifahrt, A., & Czesla, S. (2010, February). Detecting Planets Around Very Low Mass Stars with the Radial Velocity Method. ApJ, *710*, 432-443. doi: 10.1088/0004-637X/710/1/432

Reiners, A., Zechmeister, M., Caballero, J. A., Ribas, I., Morales, J. C., Jeffers, S. V.,

... Zapatero Osorio, M. R. (2017, November). The CARMENES search for exoplanets around M dwarfs: High-resolution optical and near-infrared spectroscopy of 324 survey stars. *ArXiv e-prints*.

Ricker, G. R., Winn, J. N., Vanderspek, R., Latham, D. W., Bakos, G. Á., Bean, J. L., ... Villasenor, J. (2015, January). Transiting Exoplanet Survey Satellite (TESS). *Journal of Astronomical Telescopes, Instruments, and Systems*, *1*(1), 014003. doi: 10.1117/1.JATIS.1.1.014003

Rittenhouse, D. (1786). Explanation of an optical deception. *Transactions of the American Philosophical Society*, *2*, 37–42. Retrieved from `http://www.jstor.org/stable/1005164`

Rousselot, P., Lidman, C., Cuby, J.-G., Moreels, G., & Monnet, G. (2000, February). Night-sky spectral atlas of OH emission lines in the near-infrared. A&A, *354*, 1134-1150.

Rowland, H. A. (1882, August). Preliminary notice of the results accomplished in the manufacture and theory of gratings for optical purposes. *The Observatory*, *5*, 224-228.

Rukdee, S., Park, C., Kim, K.-M., Lee, S.-H., Chun, M.-Y., Yuk, I.-S., ... T. Jaffe, D. (2012, 06). Igrins mirror mount design for three off-axis collimators and one slit-viewer fold mirror. , *29*, 233-244.

Rybicki, G. B., & Lightman, A. P. (1979). *Radiative processes in astrophysics*.

Saunders, R. W. (1996, July). Satellite meteorology - An introduction. By S.Q. Kidder and T. H. von der Haar. Academic Press. 1995. Pp 466. ISBN 012 406430 2. *Quarterly Journal of the Royal Meteorological Society*, *122*, 1227-1228. doi: 10.1002/qj.49712253312

Schroeder, D. J. (1967, November). An echelle spectrometer-spectrograph for astronomical use. Applied Optics, *6*, 1976. doi: 10.1364/AO.6.001976

Schwab, C., Jovanovic, N., Feger, T., Bakovic, M., V. Gurevich, Y., Stürmer, J., ... Guyon, O. (2016, 07). *Adaptive optics fed single-mode spectrograph for high-precision doppler measurements in the near-infrared.*

Schwab, C., Stürmer, J., Gurevich, Y. V., Führer, T., Lamoreaux, S. K., Walther, T., & Quirrenbach, A. (2015, September). Stabilizing a Fabry-Perot Etalon Peak to 3 cm s^{-1} for Spectrograph Calibration. PASP, *127*, 880. doi: 10.1086/682879

Schweizer, F. (1979, February). Anamorphic Magnification of Grating Spectrographs - A Reminder. PASP, *91*, 149. doi: 10.1086/130458

Seifahrt, A., Käufl, H. U., Zängl, G., Bean, J. L., Richter, M. J., & Siebenmorgen, R. (2010, December). Synthesising, using, and correcting for telluric features in high-resolution astronomical spectra . A near-infrared case study using CRIRES. A&A, *524*, A11. doi: 10.1051/0004-6361/200913782

Shannon, R. R., & Wyant, J. C. (Eds.). (1992). *Applied Optics and Optical Engineering, Volume XI* (Vol. 11).

Simons, D. A., & Tokunaga, A. (2002). The mauna kea observatories near-infrared filter set. i. defining optimal 1–5 micron bandpasses. *Publications of the Astronomical Society of the Pacific*, *114*(792), 169. Retrieved from `http://stacks.iop.org/1538-3873/114/i=792/a=169`

Stefansson, G., Hearty, F., Robertson, P., Mahadevan, S., Anderson, T., Levi, E., ... Terrien, R. (2016, December). A Versatile Technique to Enable Sub-milli-Kelvin Instrument Stability for Precise Radial Velocity Measurements: Tests with the Habitable-zone Planet Finder. ApJ, *833*, 175. doi: 10.3847/1538-4357/833/2/175

Tala, M., Berdja, A., Jones, M., Vanzi, L., Ropert, S., Flores, M., & Viscasillas, C. (2014, July). FIDEOS: a high resolution echelle spectrograph for the ESO 1m telescope at La Silla. In *Ground-based and airborne instrumentation for astronomy v* (Vol. 9147, p. 914789). doi: 10.1117/12.2056551

Tala, M., Vanzi, L., Avila, G., Guirao, C., Pecchioli, E., Zapata, A., & Pieralli, F. (2017, April). Two simple image slicers for high resolution spectroscopy. *Experimental Astronomy*, *43*, 167-176. doi: 10.1007/s10686-017-9526-5

Tamura, M., Suto, H., Nishikawa, J., Kotani, T., Sato, B., Aoki, W., ... Terada, H. (2012, September). Infrared Doppler instrument for the Subaru Telescope (IRD). In *Ground-based and airborne instrumentation for astronomy iv* (Vol. 8446, p. 84461T). doi: 10.1117/12.925885

Tamura, M., & team, I. (2015). Extra-solar planets exploration using frequency comb: Infrared doppler instrument for the subaru telescope (ird). In *Optical fiber communication conference* (p. Tu2C.3). Optical Society of America. Retrieved from `http://www.osapublishing.org/abstract.cfm?URI=OFC-2015-Tu2C.3` doi: 10.1364/OFC.2015.Tu2C.3

Tarter, J. C., Backus, P. R., Mancinelli, R. L., Aurnou, J. M., Backman, D. E., Basri, G. S., ... Young, R. E. (2007, March). A Reappraisal of The Habitability of Planets around M Dwarf Stars. *Astrobiology*, *7*, 30-65. doi: 10.1089/ast.2006.0124

Vanderburg, A., Latham, D. W., Buchhave, L. A., Bieryla, A., Berlind, P., Calkins, M. L., ... Johnson, J. A. (2016, January). Planetary Candidates from the First Year of the K2 Mission. ApJS, *222*, 14. doi: 10.3847/0067-0049/222/1/14

Vanzi, L., Chacon, J., Helminiak, K. G., Baffico, M., Rivinius, T., Štefl, S., ... Guirao, C. (2012). Pucheros: a cost-effective solution for high-resolution spectroscopy with

small telescopes. *Monthly Notices of the Royal Astronomical Society*, *424*(4), 2770–2777. Retrieved from http://dx.doi.org/10.1111/j.1365-2966.2012.21382.x doi: 10.1111/j.1365-2966.2012.21382.x

Vanzi, L., Zapata, A., Flores, M., Brahm, R., Tala Pinto, M., Rukdee, S., ... Espinoza, N. (2018, July). Precision stellar radial velocity measurements with FIDEOS at the ESO 1-m telescope of La Silla. MNRAS, *477*, 5041-5051. doi: 10.1093/mnras/sty936

Wandel, A. (2018). On the biohabitability of m-dwarf planets. *The Astrophysical Journal*, *856*(2), 165. Retrieved from http://stacks.iop.org/0004-637X/856/i=2/a=165

Weber, M. (2002). *Handbook of optical materials*. Taylor & Francis. Retrieved from https://books.google.cl/books?id=6VpQDoef05wC

Wyant, J. C., & Creath, K. (1992). Basic Wavefront Aberration Theory for Optical Metrology. In R. R. Shannon & J. C. Wyant (Eds.), *Applied optics and optical engineering, volume xi* (Vol. 11, p. 2).

Yoshii, Y., Aoki, T., Doi, M., Handa, T., Kawara, K., Kato, D., ... Hamuy, M. (2010, July). The University of Tokyo Atacama Observatory 6.5m telescope project. In *Ground-based and airborne telescopes iii* (Vol. 7733, p. 773308). doi: 10.1117/12.856680

Yoshii, Y., Doi, M., Kohno, K., Miyata, T., Motohara, K., Kawara, K., ... Garay, G. (2016). *The university of tokyo atacama observatory 6.5m telescope: project overview and current status* (Vol. 9906). Retrieved from http://dx.doi.org/10.1117/12.2231391 doi: 10.1117/12.2231391